

# **Compositional and Structural Characterisation of Polymer Photovoltaic Devices**

By

Ignacio Cobo Ocejó

A thesis submitted for the degree of

Master of Science

in the

University of Dublin

School of Physics

Trinity College Dublin

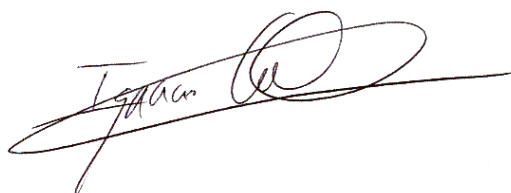
June 2008

# Declaration

I declare that the work in this thesis has not been previously submitted as an exercise for a degree to this or any other university.

The work described herein was carried out by me alone, excepted for the assistance mentioned in the acknowledgements.

I agree that Trinity College Library may lend or copy this thesis on request.

A handwritten signature in black ink, appearing to read 'Ignacio Cobo Ocejo', with a large, stylized flourish at the end.

---

Ignacio Cobo Ocejo

June 2008

# Acknowledgements

Firstly, I would like to thank my supervisor for the past two years, Professor Werner J. Blau, for his help, scientific, moral and financial support, over the course of this Masters. It has been a great experience for me to study, learn and work in his group.

I would like to express a special thank to Prof. John O'Connor and Dr. Paul Dastoor for giving me the opportunity to work at the Nanomaterials Newcastle Devices Group at the University of Newcastle, Australia, from February to May 2005, and Prof. Gordon Wallace and Dr. Andrew Minnet for welcoming me to the Intelligent Polymer Research Institute at the University of Wollongong, Australia, in June 2005.

A special thank you goes to Chris Harris for sharing his polymer solar cells skills collaborating on the polymer nanotube photovoltaic devices network. It was a great experience to be able to work together in the same project at the University of Newcastle, Australia.

From members of staff in the Department of Physics, I would like to acknowledge the valued help of Jeanette Cummins and John Kelly for administrative assistance.

To other people in the group, past and present, who I have interacted with during the last two years – to Dr. Patrick Fournet, who was the first person to introduce me in the field of photovoltaic devices, Dr. Jonathan Coleman, Dr. Colin Belton, Dr. Stephen Lipson, Dr. Margaret Brennan, Adam Strevens, Robert Murphy, David Blond, Martin Djiango, Valeria Nicolosi, Kevin Ryan, Grace Jordan, Denis McCarthy, Shane Bergin, Helen Cathcart, Fiona Blighe, Emer Lahiff, Rory Leahy, Cathal Frizell, Chris Kufazvinei, Dr. Silvia Giordani, Dr. Manuel Ruether, Dr. Rebekah D'Arcy, Dr. Gordon Armstrong, Keith Fortune, Trevor Woods, Dr. Shweta Nandu, Dr. Ramesh Babu, Dr. John Fields, James Doyle, Eimhin Ni Mhuirheartaigh, Eveann Nolan, Sharon King, Umar Khan, Yenny Hernandez, Alexander Fleming, Anna Drury, Ronan Hodson, Dr. Takeyuki Kobayashi, and David Rickard – , and everybody else I have ever met during these last two years.

Finally, I would like to thank my parents, Domingo and Isabel, and sisters, Noelia and Silvia, for their help and support.

# Abstract

Organic materials have enormous relevance in material science and have many advantages over materials such as metals, ceramics and glass due to their physical and mechanical properties. They offer a viable alternative to their inorganic counterparts due to their low manufacturing costs and their mechanical and electrical properties.

Polymer / fullerene composites are really interesting organic material candidates for photovoltaic devices as they are chemically very stable and have excellent electrical properties. In order to get a good balance between hole and electron conduction, polymers can assume the function of hole transport materials, and fullerenes can function as an optimal electron transport.

In this project, several electron donor semiconducting polymers, such as poly[2,5-dimethoxy-(2'-ethylhexyloxy)-1,4-phenylenevinylene] (MEH-PPV), poly(3-hexylthiophene-2,5-diyl), (P3HT), combined with fullerenes such as C<sub>60</sub> or the derivative [6,6]-phenyl-C<sub>61</sub> (PCBM), were selected for use in the manufacture organic solar cells. Charge transport of these blends was investigated. (Poly (3,4-ethylenedioxythiophene) (PEDOT:PSS) was used as a hole transport conducting polymer. Indium Tin Oxide (ITO) and Aluminium (Al) were used as electrodes.

Spectral response and current-voltage measurements using 80 mW/cm<sup>2</sup> white illumination, simulating solar energy illumination, were analysed in order to determine the photovoltaic behaviour of organic solar cells. Absorption spectroscopy was carried out to analyse the charge transfer within the composites and at the interface between the composites and the other polymer layers. Also, calorimetric studies helped us to characterise these polymer and fullerene composites. An optimum photovoltaic response and relative efficiency of 2.3 % was obtained for ITO / PEDOT:PSS / P3HT:PCBM / Al devices after annealing treatment.

The effect of incorporating single-walled and multi-walled carbon nanotubes (SWNT and MWNT) in to organic solar cells had been studied. Free-standing carbon nanotube / polymer composite films, using chemical vapour deposition (CVD) in order to grow nanotubes on substrates, were also investigated as candidates for organic solar cells.

The project aims to, together with understanding the underlying physics, determine which materials and device architectures are more appropriate to obtain better power conversion efficiencies.

# Table of Contents

<b>ABSTRACT</b> .....	<b>iv</b>
<b>LIST OF FIGURES AND TABLES</b> .....	<b>vii</b>
<b>CHAPTER 1 - MOTIVATION AND OUTLINE</b> .....	<b>1</b>
<b>1.1 Renewable energy</b> .....	<b>1</b>
<b>1.2 Plastic solar cells</b> .....	<b>2</b>
<b>1.3 Thesis outline</b> .....	<b>4</b>
<b>CHAPTER 2 - INTRODUCTION TO PHOTOVOLTAIC DEVICES</b> .....	<b>6</b>
<b>2.1 Introduction</b> .....	<b>6</b>
<b>2.2 Physical process of organic materials</b> .....	<b>6</b>
2.2.1 Charge generation in conjugated polymers .....	6
2.2.2 Single layer diodes .....	7
2.2.3 Heterojunction diodes .....	8
<b>2.3 Photovoltaic characterization of solar cells</b> .....	<b>11</b>
2.3.1 Equivalent circuit diagram .....	11
2.3.2 Important parameters in solar cells .....	12
<b>2.4 Annealing treatment</b> .....	<b>13</b>
2.4.1 Heat transfer .....	14
2.4.2 Annealing on a hot plate .....	15
<b>2.5 Conclusions</b> .....	<b>16</b>
<b>CHAPTER 3 - MATERIALS AND EXPERIMENTAL BACKGROUND</b> .....	<b>17</b>
<b>3.1 Introduction</b> .....	<b>17</b>
<b>3.2 Materials</b> .....	<b>17</b>
3.2.1 Indium-Tin-Oxide (ITO) coated glass .....	17
3.2.2 Electron donor MEH-PPV .....	18
3.2.3 Electron donor P3HT and P3OT.....	19
3.2.4 Hole transport PEDOT:PSS .....	19
3.2.5 Electron acceptor fullerenes C <sub>60</sub> and PCBM .....	20
3.2.6 Carbon nanotubes .....	21
<b>3.3 Polymer and carbon nanotube / fullerene composites</b> .....	<b>25</b>
3.3.1 Characterization of carbon nanotubes .....	25
3.3.2 Preparation of composites .....	25
<b>3.4 Experimental equipment</b> .....	<b>26</b>
3.4.1 Glove box, I-V and photocurrent spectroscopy .....	26
3.4.2 Profilometry .....	28
3.4.3 Absorption spectroscopy .....	29
3.4.4 Atomic Force Microscopy .....	29
3.4.5 Differential Scanning Calorimetry .....	30
3.4.6 Chemical Vapour Deposition .....	31
<b>3.5 Conclusions</b> .....	<b>32</b>
<b>CHAPTER 4 - SAMPLE PREPARATION AND CHARACTERIZATION PROCEDURES</b> .....	<b>33</b>
<b>4.1 Introduction</b> .....	<b>33</b>
<b>4.2 Preparations of sample films</b> .....	<b>33</b>
4.2.1 Substrate preparation .....	33
4.2.2 Solution preparation .....	34
4.2.3 Spin coating of polymer films .....	34
<b>4.3 Sample device design and construction</b> .....	<b>35</b>

4.3.1	General device structure .....	35
4.3.2	Device construction .....	35
4.3.3	Metal deposition .....	36
<b>4.4</b>	<b>Device characterisation .....</b>	<b>36</b>
4.4.1	Current-voltage measurements .....	36
4.4.2	Photocurrent spectroscopy - Spectral Response .....	37
4.4.3	Absorption analysis .....	37
4.4.4	Surface microscopy analysis.....	38
4.4.5	Calorimetry measurements .....	39
<b>4.5</b>	<b>Conclusions .....</b>	<b>39</b>
 <b>CHAPTER 5 - LOW EFFICIENCY MEH-PPV PHOTOVOLTAIC DEVICES ....</b>		<b>40</b>
<b>5.1</b>	<b>Introduction .....</b>	<b>40</b>
<b>5.2</b>	<b>Experimental .....</b>	<b>40</b>
<b>5.3</b>	<b>Results and discussion .....</b>	<b>41</b>
5.3.1	Single layer devices .....	41
5.3.2	Double layer devices .....	43
5.3.3	Filter effect .....	46
5.3.4	MEH-PPV and fullerene devices .....	47
<b>5.4</b>	<b>Conclusions .....</b>	<b>50</b>
 <b>CHAPTER 6 - HIGH EFFICIENCY P3HT:PCBM PHOTOVOLTAIC DEVICES</b>		<b>51</b>
<b>6.1</b>	<b>Introduction .....</b>	<b>51</b>
<b>6.2</b>	<b>Experimental .....</b>	<b>51</b>
<b>6.3</b>	<b>Results and discussion .....</b>	<b>52</b>
6.3.1	Inclusion of PEDOT:PSS.....	52
6.3.2	Annealing process .....	54
6.3.3	Variation of fullerene PCBM .....	56
6.3.4	Solvent comparison .....	60
6.3.5	Effects of postproduction treatment .....	62
6.3.6	Optical properties.....	64
6.3.7	Differential Scanning Calorimetry analysis.....	68
6.3.8	Morphology analysis.....	73
<b>6.4</b>	<b>Conclusions .....</b>	<b>76</b>
 <b>CHAPTER 7 - INFLUENCE OF CARBON NANOTUBES ON PHOTOVOLTAIC DEVICES .....</b>		<b>78</b>
<b>7.1</b>	<b>Introduction .....</b>	<b>78</b>
<b>7.2</b>	<b>Experimental .....</b>	<b>78</b>
<b>7.3</b>	<b>Results and discussion .....</b>	<b>79</b>
7.3.1	Single-walled carbon nanotubes .....	79
7.3.2	Multi-walled carbon nanotubes .....	80
7.3.3	Absorption spectroscopy of P3HT:MWNT composite films .....	85
7.3.4	Absorption spectroscopy of P3HT:PCBM:MWNT composite films .....	87
7.3.5	Chemical Vapour Deposition .....	88
<b>7.4</b>	<b>Conclusions .....</b>	<b>92</b>
 <b>CHAPTER 8 - CONCLUSIONS AND FUTURE WORK .....</b>		<b>94</b>
<b>8.1</b>	<b>Conclusions .....</b>	<b>94</b>
<b>8.2</b>	<b>Future work .....</b>	<b>95</b>
 <b>REFERENCES .....</b>		<b>97</b>

# LIST OF FIGURES

Figure 1.1: Different renewable sources worldwide .....	2
Figure 1.2: Global warming over the next 53 years .....	2
Figure 2.1: Basic structure of a SL polymer photovoltaic device.....	8
Figure 2.2: Schematic diagram of heterojunction photovoltaic device .....	9
Figure 2.3: Equivalent circuit diagram for a typical solar cell .....	11
Figure 2.4: Sample I-V curve of a polymer photovoltaic cell showing $V_{oc}$ , $I_{sc}$ and the maximum power rectangle $(I.V)_{MAX}$ .....	13
Figure 2.5: How the temperature drops if a glass slide is placed onto a hot plate .....	16
Figure 3.1: Atomic force microscopy image of the surface of the ITO glass slides .....	18
Figure 3.2: UV-Vis absorption spectrum of an ITO glass slide .....	18
Figure 3.3: Repeat unit of the polymer MEH-PPV .....	19
Figure 3.4: Repeat unit of the polymer P3HT and P3OT .....	19
Figure 3.5: Chemical structures of PEDOT and PSS .....	20
Figure 3.6: Chemical structures of $C_{60}$ (left) and PCBM (right) fullerenes .....	21
Figure 3.7: Schematic image of $C_{60}$ .....	21
Figure 3.8: Models of armchairs, zigzag, and chiral nanotubes .....	22
Figure 3.9: 2D graphene sheet showing chiral vector $C_h$ and chiral angle $\theta$ .....	22
Figure 3.10: Band structure for single walled carbon nanotubes .....	23
Figure 3.11: Characteristics of thin multi-walled carbon nanotubes .....	25
Figure 3.12: Samples of composites solutions .....	26
Figure 3.13: Glove box used for electrical measurements .....	27
Figure 3.14: Schematic of the experimental setup used for taking short-circuit photocurrent spectra .....	28
Figure 3.15: AFM design .....	29
Figure 3.16: Chemical vapour deposition (CVD) set-up for the generation of aligned carbon nanotubes by pyrolysis of FePc .....	31
Figure 4.1: Top view of device architecture of polymer solar cells .....	33
Figure 4.2: Polymer film thickness as a function of different spin casting speeds for four concentrations .....	34
Figure 4.3: General device structure for photovoltaic devices .....	35
Figure 4.4: Spectral profile of a Solux lamp compared to the AM 1.5 solar mass spectrum .....	37
Figure 5.1: I-V characteristics of a MEH-PPV single layer device .....	41
Figure 5.2: Spectral response of an ITO/MEH-PPV/Al device for three different polymer film thicknesses .....	42

Figure 5.3: Spectral response of a MEH-PPV single layer device .....	43
Figure 5.4: Device structure of double layer MEH-PPV device .....	43
Figure 5.5: I-V characteristics of a MEH-PPV double layer device .....	44
Figure 5.6: Spectral response of a MEH-PPV double layer device .....	45
Figure 5.7: Spectral response of a MEH-PPV single and double layer device .....	45
Figure 5.8: Schematic picture explaining the filter effect .....	47
Figure 5.9: Power efficiency of ITO / MEH-PPV /Al as a function of the MEH- PPV layer's thicknesses .....	47
Figure 5.10: Illustration of a polymer / fullerene network in a composite .....	48
Figure 5.11: I-V characteristics of ITO/MEH-PPV:PCBM(20%w.)(70nm)/Al .....	48
Figure 5.12: Spectral response of MEH-PPV and P3HT .....	49
Figure 6.1: Device structure and operation principle on ITO/PEDOT:PSS/P3HT:PCBM/Al .....	52
Figure 6.2: I-V characteristics of a P3HT:PCBM (70 nm) layer device with and without PEDOT:PSS (30nm) layer .....	53
Figure 6.3: Spectral response of a P3HT:PCBM layer device with and without PEDOT:PSS (30nm) layer .....	54
Figure 6.4: I-V characteristics of an ITO/PEDOT:PSS(30nm)/P3HT:PCBM (70 nm)/Al photovoltaic device before and after annealing treatment .....	55
Figure 6.5: Short circuit current, efficiency, open circuit voltage and fill factor for P3HT:PCBM (1:1 by weight) blend film devices as a function of annealing time .....	56
Figure 6.6: I-V of a ITO/PEDOT:PSS(30nm)/P3HT:PCBM(70nm)/Al photovoltaic device before and after annealing as a function of PCBM Weight Ratio .....	57
Figure 6.7: Short circuit current, efficiency, open circuit voltage and fill factor for PEDOT:PSS/P3HT:PCBM blend film devices as a function of PCBM Weight Ratio .....	58
Figure 6.8: Spectral response of PEDOT:PSS/P3HT:PCBM before and after annealing at 140°C for 4 minutes .....	60
Figure 6.9: I-V characteristics of a ITO/PEDOT:PSS(30nm)/P3HT:PCBM/Al photovoltaic device before and after annealing, as a function of solvents. ....	61
Figure 6.10: I-V curves of P3HT:PCBM (1:1 weight ratio) and postproduction treatment analysis .....	62
Figure 6.11: Current density decay after different treatment processes .....	63
Figure 6.12: Spectral response of PEDOT:PSS/P3HT:PCBM before and after annealing at 140°C for 4 minutes and after 24 hours .....	64
Figure 6.13: Absorption spectra of PEDOT:PSS/P3HT:PCBM composite film	



and P3HT films before and after thermal annealing at 140°C for 4 minutes .....	65
Figure 6.14: Absorption spectra of PEDOT:PSS/P3HT:PCBM composite film after successive thermal annealing steps .....	66
Figure 6.15: Absorption spectra of P3HT:PCBM composite films as a function of PCBM weight ratio before and after annealing at 140°C for 4 minutes .....	67
Figure 6.16: Absorption spectra after annealing and during evaporation of Al electrodes .....	68
Figure 6.17: DSC results obtained of P3HT .....	69
Figure 6.18: DSC results obtained of P3HT. $T_g$ , $T_m$ and $T_c$ .....	70
Figure 6.19: DSC results obtained of the P3HT:PCBM composite with $T_m$ and $T_c$ .....	71
Figure 6.20: DSC results obtained of fullerene PCBM .....	72
Figure 6.21: AFM images of P3HT:PCBM composite films .....	73
Figure 6.22: Height line scans across the P3HT:PCBM composite film .....	74
Figure 6.23: SEM images of P3HT:PCBM composite film .....	76
Figure 6.24: TEM images of P3HT:PCBM composite film .....	75
Figure 7.1: Chemical structures and device architecture of P3OT:SWNT device .....	79
Figure 7.2: Spectral response of polymer MWNT composites .....	81
Figure 7.3: Spectral response of polymer MWNT composites .....	82
Figure 7.4: I-V characteristics of P3HT and MWNT composite .....	83
Figure 7.5: I-V characteristics of P3HT:PCBM:MWNT composites .....	84
Figure 7.6: SEM images of P3HT:PCBM:MWNT annealed composite film .....	85
Figure 7.7: Absorption spectrum of P3HT:MWNT devices .....	86
Figure 7.8: Absorption spectrum of P3HT:PCBM:MWNT devices .....	87
Figure 7.9: Growth of carbon nanotube mechanism using CVD.....	88
Figure 7.10: SEM images of carbon nanotube growth on silicon substrates .....	89
Figure 7.11: SEM images of carbon nanotube growth on ITO and free-standing film ....	90
Figure 7.12: Picture of free standing composite containing carbon nanotubes .....	90
Figure 7.13: SEM images of different aligned carbon nanotubes composites .....	91
Figure 7.14: Picture of aligned carbon nanotube device. Top views .....	91

# LIST OF TABLES

Table 1: $J_{SC}$ , $V_{OC}$ , $(IV)_{MAX}$ , FF and $\eta_e$ of ITO / MEH-PPV / Al solar cells as a function of the thickness of the polymer MEH-PPV layer .....	44
Table 2: $J_{SC}$ , $V_{OC}$ , $(IV)_{MAX}$ , FF and $\eta_e$ of ITO / MEH-PPV / Al solar cells as a function of the thickness of the polymer MEH-PPV layer .....	46
Table 3: $J_{SC}$ , $V_{OC}$ , $(IV)_{MAX}$ , FF and $\eta_e$ of different polymer composites solar cells .....	49
Table 4: $J_{SC}$ , $V_{OC}$ , $(IV)_{MAX}$ , FF and $\eta_e$ of ITO/ P3HT:PCBM/Al and ITO/PEDOT:PSS/P3HT:PCBM/Al devices.....	53
Table 5: $J_{SC}$ , $V_{OC}$ , $(IV)_{MAX}$ , FF and $\eta_e$ of ITO/PEDOT:PSS/P3HT:PCBM/Al before and after annealing .....	55
Table 6: $J_{SC}$ , $V_{OC}$ , $(IV)_{MAX}$ , FF and $\eta_e$ of ITO/PEDOT:PSS/P3HT:PCBM/Al before and after annealing as a function of PCBM Weight Ratio .....	59
Table 7: $J_{SC}$ , $V_{OC}$ , $(IV)_{MAX}$ , FF and $\eta_e$ of ITO/PEDOT:PSS/P3HT:PCBM/Al before and after annealing as a function of solvent used .....	61
Table 8: $J_{SC}$ , $V_{OC}$ , $(IV)_{MAX}$ , FF and $\eta_e$ of ITO/P3OT/Al and ITO/P3OT:SWNT/Al .....	80
Table 9: $J_{SC}$ , $V_{OC}$ , $(IV)_{MAX}$ , FF and $\eta_e$ of polymer and MWNT composites .....	81

# CHAPTER 1 - MOTIVATION AND OUTLINE

## 1.1 Renewable energy

The worldwide demand for energy has grown dramatically over recent years with an increase in the industrialisation of the world. The need for energy is likely to grow even more in the 21<sup>st</sup> century with the improvements in living conditions across the world. This high demand for energy actually brings and will continue to bring into question the energy sources used and the depletion of natural resources.

Most of our energy comes from non-renewable sources, but due to the limited supply of our main energy sources, oil, coal and uranium, we will be forced to turn to renewable energy sources such as wind energy, hydroelectric power, biomass and solar energy (see Figure 1.1).

It has been predicted that within ten or fifteen years oil production will be unable to keep up with demand [1] an increase in oil prices worldwide will result, thus making renewable sources very necessary and much more favourable.

The combustion of fossil fuels is used to produce electric power and heat, but this generates by products such as carbon dioxide (CO<sub>2</sub>) and sulphur compounds (e.g. SO<sub>2</sub>). Plants are unable to absorb this amount of CO<sub>2</sub> leading to the green house effect and global warming (Figure 1.2). This will result in the melting of the polar ice caps causing a rise in sea levels and covering of coastal areas all over the world.

Renewable energy sources use natural resources without depleting them and have no harmful side effects for the environment. Examples include energy from water due to waves, power plants that use wind energy, energy from rivers using tidal motion or potential energy, and solar energy. The energy provided from the sun can be used in solar collector systems to heat water or by directly converting the solar energy into electrical energy using photovoltaic devices.

Current renewable energy systems cannot produce energy at the same low cost as conventional fossil fuel plants. For large-scale implementation of renewable energy plants, it is therefore necessary to develop systems that can compete on an economic level with fossil fuel facilities, either by decreasing cost, increasing efficiency or a combination of both.

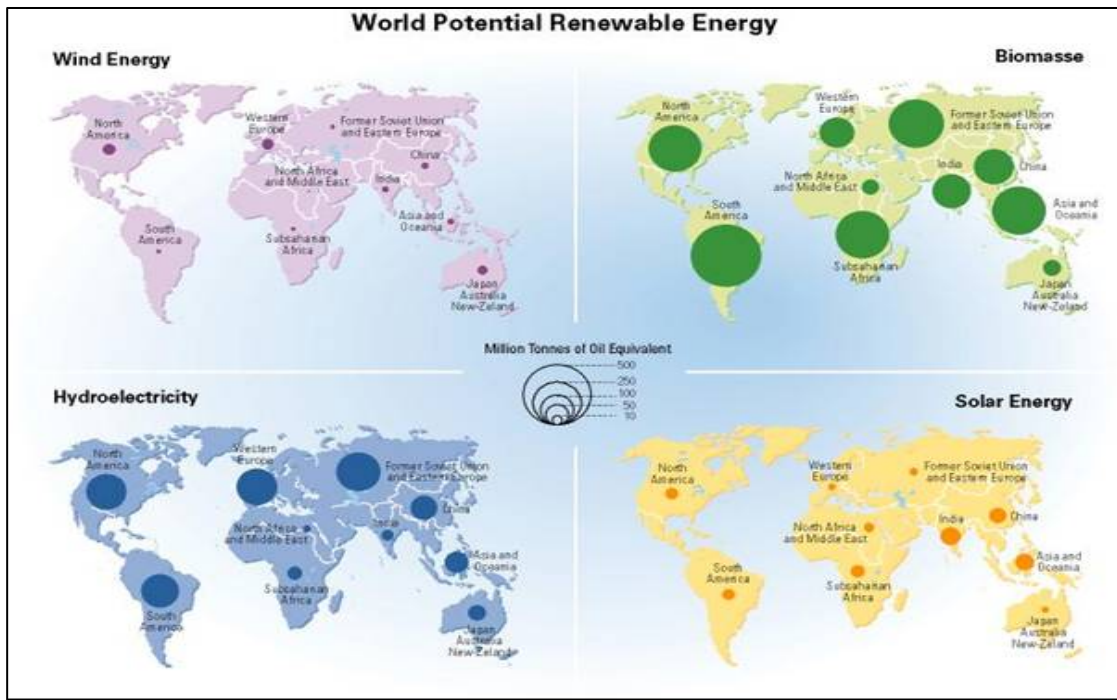


Figure 1.1. Different renewable sources worldwide (www.grida.no).

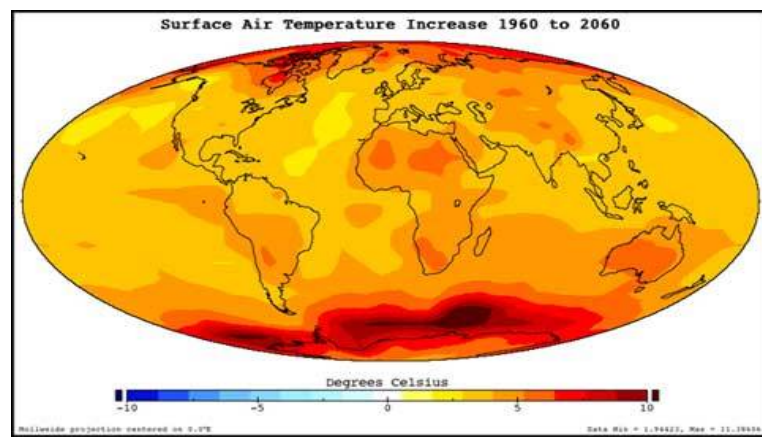


Figure 1.2. Global warming over the next 53 years (www.nasa.gov).

## 1.2 Plastic solar cells

Photovoltaic devices are renewable energy power resources. The optical energy supplied by the sun can be converted into electrical energy in a solar cell. Unfortunately at present one can only find high cost Si solar cells. So we need to make solar cells more competitive with fossil fuel power plants by reducing the price of manufacturing solar cells.

Fortunately the supply of energy from the sun to the earth is enormous:  $3 \times 10^{24}$  J per year, or about 10,000 times more than the global population currently consumes. In other words, covering 0.1 % of the earth's surface with solar cells with an efficiency of 10 % would satisfy our present needs.

The actual solar energy market is growing rapidly, crystalline silicon dominates the industry but the reduction of solar grade silicon and wafers due to high demand gives us the motivation to introduce new materials. Solar cells based on organic materials raise considerable interest because they offer the hope of large manufacturing at low temperatures and low costs. However, at present there are many obstacles to make organic solar cells a practical reality, for example improving the power conversion efficiency of these devices, which have barely reached 3% compared to over 30% for their inorganic cousins. So molecular electronics and nanotechnology now play an important role in photovoltaic industry. The introduction of polymers, fullerenes and carbon nanotubes will be the key to develop new devices. These materials are also interesting because of their potential for use in many applications such as photovoltaic devices.

Photovoltaic devices based on organic materials should cost less than traditional materials [2, 3, 4, 5, 6, and 7]. Si or GaAs can be replaced by semiconducting polymer materials in combination with fullerenes as the active layer. These materials are usually soluble in common organic solvents.

Over the last 30 years there has been increasing interest in exploiting the properties of these organic materials. In 1977, A. J. Heeger, A. G. McDiarmid and H. Shirakawa were awarded the Nobel Prize for Chemistry in 2000, for discovering unique properties of one class of organic materials, conjugated polymers. They discovered that the chemical doping of these materials resulted in an increase in electronic conductivity over several orders of magnitude [8]. Since then, electrically conducting materials have been applied in many diverse applications.

Thin films of these organic materials dissolved in organic solvents can be made by spin casting [9] and since the organic films are flexible, they can be applied to flexible plastic substrates ( Indium Tin Oxide (ITO)-coated PET substrate) making the whole device flexible [10].

Although organic cells are still considerably less efficient than inorganic solar cells, significant progress has been in improving organic cell efficiency during the last few years. In particular, solar cells based on polymer networks, polymer and fullerene blends, and solid-state dye-synthesised devices have shown high solar conversion efficiencies reaching values of 1.5-2% [47].

A review of organic photovoltaic solar cells appropriate to the time of this thesis is explained as follows. Early studies in 1994 showed the first polymer bulk heterojunction devices constructed based on blends of MEH-PPV (poly[2,5-dimethoxy-(2'-ethylhexyloxy)-1,4-phenylenevinylene) and fullerene C<sub>60</sub> spin coated.

These devices exhibited a photosensitivity an order of magnitude higher than MEH-PPV, but their efficiency was still very low. The next significant improvement in device efficiency came from the introduction of blends with the soluble fullerene C<sub>60</sub>-derivative PCBM (6,6)-phenyl-C<sub>61</sub>-butyric acid). Blends with (poly[2-methoxy-5-(3,7-dimethyloctyloxy)]-1,4-phenylenevinylene) MDMO-PPV and PCBM showed better photovoltaic responses. After this improvement, a further increase in efficiency was achieved by changing the polymer [41]. Polythiophene derivatives, such as P3HT (poly (3-hexylthiophene-2,5-diyl)) and P3OT (poly (3-octylthiophene-2,5-diyl)), have a slightly lower band gap than MDMO-PPV, giving them a broader spectral response and better photovoltaic efficiency. Devices based on blends of P3HT and PCBM were shown to give efficiencies of 1.5%. However this efficiency could only be brought about after the devices were given a postproduction annealing treatment of 140°C for 4 minutes. The improvement obtained from annealing was explained in terms of an increase in the hole mobility of the polymer resulting from enhanced crystallisation from heating above the glass transition temperature. The increase in photovoltaic response of P3HT:PCBM after annealing clearly represents an exciting development in the history of organics photovoltaic devices [49]. In this work these last P3HT:PCBM photovoltaic devices were selected for further investigations. A new approach of annealing treatment at higher temperatures will be shown to be a good method to get higher photovoltaic power conversion efficiencies. Devices with power conversion efficiencies of up to 2.2 % were fabricated.

To further enhance the efficiency of the devices, a slightly more complicated structure based on a polymer carbon nanotube photovoltaic device [11] using Chemical Vapour Deposition (CVD) grown carbon nanotubes is suggested. This leads to new structures where the interface between the electron donors and acceptors is diffuse, but only the donor material has contact to the anode (ITO) and only the acceptor material has contact to the cathode (Aluminium). These structures should enhance the transport of electrons and holes through the acceptor and donor material respectively. In this work CVD technique was considered to increase the effectiveness of carbon nanotubes in polymer devices improving carbon nanotube manipulation and morphology.

### **1.3 Thesis outline**

Chapter 2 gives an introduction to the physical processes in photovoltaic devices based on organic materials. This knowledge is essential to understand the

charge creation and separation processes that occur in organic photovoltaic devices. After that, a basic description of photovoltaic devices is given and the solar cells are characterised. This will help us to understand how the photovoltaic devices work. Finally, a few considerations regarding heat and mass transfer and interdiffusion due to annealing are discussed.

In Chapter 3, the materials and the experimental equipment used in this work are described. Donor and acceptor materials are discussed as well as some information about the polymer and carbon nanotubes/fullerene composites characterisation and preparation.

Chapter 4 outlines the sample preparation and the experimental procedures employed throughout this thesis. Three distinct sections describe the preparation of sample films, the sample device and construction and the different device characterisation methods used in this work.

In Chapter 5, some preliminary studies relating to the basic organic photovoltaic devices are carried out. In this Section, the characteristics of simple photovoltaic devices using an active polymer layer allowed us to determine and study different photovoltaic responses.

Chapter 6 describes main work of this research, the polymer and fullerene blends that are used to study the interdiffusion between the polymer and the fullerene. Annealing of the photovoltaic devices and morphology studies with Atomic Force Microscopy (AFM) and Scanning Electron Microscopy (SEM) shows the diffusion of the fullerenes into the polymer bulk. Larger improvements in terms of power conversion efficiencies are achieved by annealing the devices below the melting temperature. Differential Scanning Calorimetry analysis (DSC) is also carried out to understand the crystallinity of polymer and fullerene blends. Note that the polymer used in this section is microcrystalline exhibiting both a glass transition and a melting temperature.

Chapter 7 shows the effects of using carbon nanotube and polymer composites in organic photovoltaic devices. Both single-walled and multi-walled carbon nanotubes are used. Chemical Vapour Deposition (CVD) is introduced to demonstrate an improvement in nanotube processing and the potential to be included in photovoltaic devices. Optical properties of these last devices are also carried out.

Finally, Chapter 8 concludes this thesis by reviewing the research presented in the previous chapters. Also, future projects are considered.

# **CHAPTER 2 - INTRODUCTION TO PHOTOVOLTAIC DEVICES**

## **2.1 Introduction**

This chapter will outline the physical properties of solar cells in Section 2.2. Process of charge generation, separation, transfer and transport through a device will also outline in Section 2.2. This section will discuss all the processes that occur in organic photovoltaic devices such as single layer (SL) photovoltaic diodes and heterojunction diodes. Photovoltaic characterisation will be presented in Section 2.3, along with all the important parameters used to characterise these devices. Heat treatment and related issued will be discussed in Section 2.4.

## **2.2 Physical properties of organic materials**

The conversion of solar light into electrical energy requires the generation of both negative and positive charges as well as a driving force that can push these charges through an external electric circuit. When connected to the external electric circuit any electrical device may then utilise the converted solar energy.

### **2.2.1 Charge generation in conjugated polymers**

Polymers are long macromolecules consisting of repeating structural units called monomers that are linked together by covalent chemical bonds during polymerisation process. Polymers containing backbones of alternating single and double carbon-carbon bonds are termed Conjugated Polymers (CPs). 1977 heralded the amazing discovery that polyacetylene could be made electrically conductive by chemical doping and this work paved the way to a wide range of semiconducting polymers with behaviour ranging from insulating to near metallic. The semiconducting behaviour of these materials meant they had great potential in photovoltaic devices. Polymer solar cells utilize the semiconducting properties of conjugated polymers to convert light energy into electrical current. The photophysics of conjugated



polymer/fullerene solid composites has been particularly well investigated over the last few years.

The charge conduction mechanism appears to be more complex for semiconducting polymers than for inorganic semiconductors. Although the action of an incident photon on a conducting polymer excites an electron from the valence band into the conduction band, the resulting electron and hole are bound, and their motion through the material is coupled. These coupled moieties are known as excitons and are responsible for many of the electronic properties found in the most common and efficient polymer-based electronic devices.

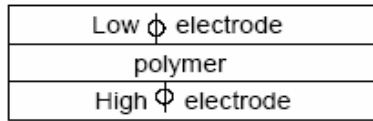
### **2.2.2 Single layer diodes**

The simplest polymer photovoltaic device is based on a single polymer layer (SL) sandwiched between two metal electrodes of different work functions. The different work functions of the electrodes cause the device to function as a diode, since a metal-semiconductor Schottky barrier is formed at each interface.

On absorption of light, excitons are generated in the polymer. An exciton is the bound state of an electron and hole pair and is the primary product of photoexcitation of a semiconductor, such as a CP. When a CP absorbs light, the energy excites an electron from the valence band into the conduction band. The missing electron in the valence band leaves behind a hole, which is positively charged and attracted to the electron by Coulomb force. The exciton can travel to states with lower energy level [12]. The typical life-time of the exciton [13, 14] is hundreds of picoseconds, and the diffusion length, is approximately 10 nm [15, 16]. All photoexcited excitons should reach a dissociation state. Excitons may travel through a polymer typically tens of nanometres before it can:

- Radiatively recombine to produce a photon, which is called photoluminescence.
- Non-radiatively recombine, resulting in the energy being dissipated in the form of phonons
- Be dissociated to produce a free electron and hole.

(1)



(2)

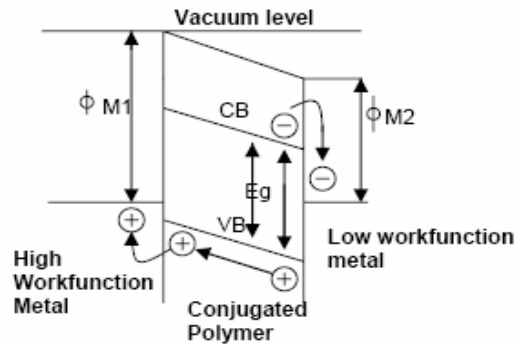


**Figure 2.1.** (1) Basic structure of a SL polymer photovoltaic device, (2) energy level diagram showing the operation of a SL polymer photovoltaic device under short circuit conditions. CB = conduction band = lowest unoccupied molecular orbital (LUMO), VB = valance band = highest occupied molecular orbital (HUMO),  $E_g$  = band energy gap,  $\phi$  = work function.

This may occur at any interface in the device, which in the case of Figure 2.1, is at the interface between polymer and either electrode.

Figure 2.1 is an energy diagram showing the operations of a single layer (SL) polymer photovoltaic device under short-circuit conditions. The difference in work function of the two electrodes causes their Fermi energies to equilibrate, creating an internal electric field which acts to transport the free charges to the opposite electrodes. In this so-called metal-insulator-metal (MIM) model the open circuit voltage of the device is given as the difference in work function of the two electrodes.

Earlier SL photovoltaic device based on poly (phenylene vinylene) (PPV) and poly[2,5-dimethoxy-(2'-ethylhexyloxy)-1,4-phenylenevinylene (MEH-PPV) used as semiconducting polymers gave relatively low efficiencies which are associated with a very low incidence of exciton dissociation in the device and poor transport of the separated charges to the respective electrodes.

### 2.2.3 Heterojunction diodes

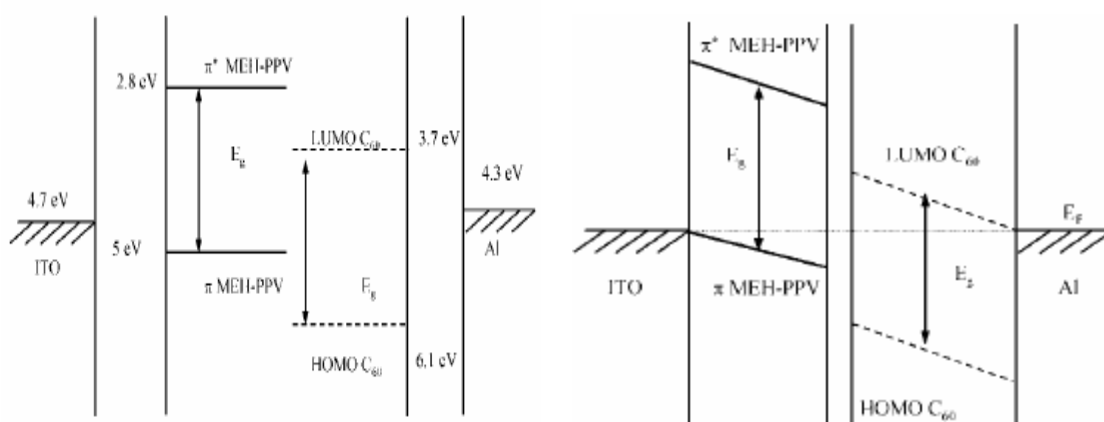
Given the problems faced in single layer polymer photovoltaic devices, the most obvious ways to increase the efficiency would be to:

- Increase the amount of interfaces
- Improve the electron mobility

This approach was first attempted by Tang in 1986 who demonstrated that the efficiency of dye based photovoltaic devices could be elevated by an order of magnitude by creating a heterojunction at the interface between two dye layers of different electronegativity, resulting in enhanced exciton dissociation.

Considering the energy band diagram of a bilayer in Figure 2.2 (1), the heterojunction formed between a conjugated polymer and  $C_{60}$  should have rectifying current-voltage characteristics even using the same metal contact on both sides (analogous to a p-n junction). One bias direction of such a device (electron injection on the semiconducting polymer side or hole injection on  $C_{60}$ ) is energetically unfavourable. This polarity of the device results in very low current densities. On the other hand, electron injection onto  $C_{60}$  or hole injection into the semiconducting polymer is energetically favourable. This polarity of the device results in relatively high current densities. Thus, devices of organic semiconductors using two layers with different electronic band structures as illustrated in Figure 2.2 (1) have rectifying diode characteristics. A photophysical interaction between the two molecular units (photo-induced electron transfer) happens at the interface and gives rise to photocurrent as well as a photovoltaic effect. In that sense the essential difference between the linear heterojunction of two organic thin films displayed in Figure 2.2 (1) and the bulk heterojunctions displayed in Figure 2.2 (2) is that the effective interactions are between the donor and acceptor components. In the linear heterojunction device it is the geometrical interface, in the bulk heterojunction it is the entire volume of the composite layer. This results in an enhancement of short circuit photocurrent for several orders of magnitude making the bulk heterojunction approach quite attractive.

(1)



(2)

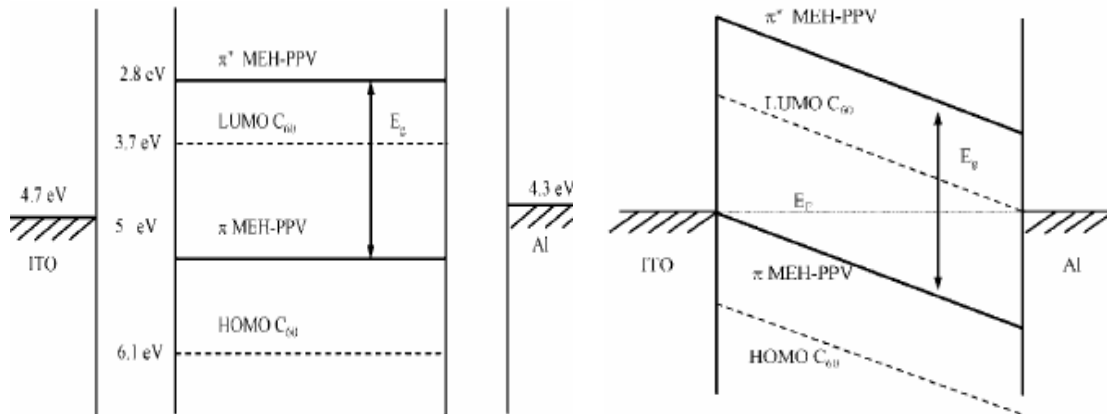


**Figure 2.2.** (1) Schematic diagram of a bilayer polymer photovoltaic device and energy levels under flat band conditions and under short circuit conditions. (2) Schematic diagram of a bulk heterojunction system under flat band conditions and under short circuit conditions. Reproduced from [17].

In 1994, the first polymer based bulk heterojunction device was constructed, which used a blend of MEH-PPV and  $C_{60}$  spin coated from xylene. This device exhibited a photosensitivity an order of magnitude higher than MEH-PPV, but its efficiency was still very low. The problem here was that there was not enough  $C_{60}$  in the blend to maximize charge separation and transport. However pure  $C_{60}$  has low solubility in organic solvents and crystallises during formations. These devices exhibited efficiencies two orders of magnitude higher than those that have been achieved with devices made with pure MEH-PPV, efficiencies of less than 0.01% [41].

To improve the solubility of  $C_{60}$ , derivatives such as phenyl-[6,6]- $C_{61}$ -butyric acid methyl ester (PCBM) were synthesized. This new material allowed for greater loadings of fullerene with respect to the polymer, so that the percolation network of the fullerene could be achieved within a PCBM/polymer composite, which would then lead to enhanced electron transport. Indeed, efficiencies of 1.5% under monochromatic light were obtained from devices using blends of PCBM with MEH-PPV. To this date, the polymer/PCBM blend represents the highest efficiency for solar cells. Devices based on blends of polymers such as Poly(3-hexylthiophene) (P3HT) and fullerenes PCBM have also shown better photovoltaic responses therefore higher efficiencies [47].

To summarize this section, we need to note that in organic photovoltaic

elements generally two different tasks are to be clearly distinguished:

- The photo-induced charge generation (electron transfer efficiency) and
- The transport of created charges to the electrodes (charge carrier mobility)

These two different tasks are expected to be fulfilled by one and the same material simultaneously. A possible strategy is to separate the two tasks by using separate components in a device for the charge transport and for the charge generation.

In conclusion in this section 2.2 the progress from single layer polymer devices to bulk heterojunction photovoltaic devices has been described.

## 2.3 Photovoltaic Characterisation of Solar Cells

The main properties to characterise the photovoltaic behaviour of a solar cell are described. The intention of this chapter is to give a basic understanding of organic photovoltaic devices. In the following section, the equivalent circuit diagram and the most important parameters of solar cells are explained. There are a few important parameters which are used to characterize the performance of solar cells and thus are used throughout this thesis.

### 2.3.1 Equivalent Circuit Diagram

The equivalent circuit diagram (ECD) describes the electric behaviour of complex devices in terms of components such as current or voltage sources, resistors, diodes and capacitors. Figure 2.3 shows a typical ECD used for inorganic solar cells. The components shown can be described as follows:

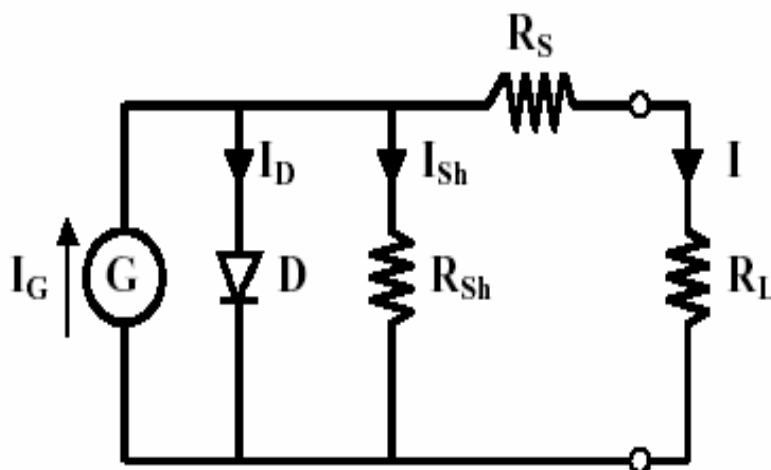


**Figure 2.3.** Equivalent Circuit Diagram for a typical solar cell.

- The current  $I_G$  generated by the source G. This current comes from dissociation of excitons into electrons and holes after photon absorption. It depends only on the charge carrier creation efficiency.

- The series resistor  $R_S$  depends on the mobility of charge carriers in the bulk of the solar cells. This mobility is influenced by defects and barriers.  $R_S$  will only increase with the thickness of the device due to the distance that the charges have to travel. The series resistor is given by the slope of the I-V curve at higher voltages.

- The shunt resistor  $R_{Sh}$  represents the recombination of holes and electrons after the exciton dissociation, but before the charge transport through the bulk occurs.

The sum of the series resistor  $R_S$  and shunt resistors  $R_{Sh}$  is given by the slope of the I-V curve at lower voltages, towards zero, when the cell operates in the short circuit regime.

The series and parallel resistances are calculated according to the formula

$$R_S = \left( \frac{dV}{dI} \right)_{V \rightarrow \infty}, \quad R_S + R_{Sh} = \left( \frac{dV}{dI} \right)_{V \rightarrow 0}$$

- The diode D, describes the asymmetric conductivity in the photovoltaic device.

- The resistor  $R_L$  only has an effect when the solar cell is connected to an external load. Otherwise, a source measure unit can be connected to calculate the I-V characteristics of the solar cell.

For an ideal solar cell,  $R_{Sh}$  would be infinitely large and  $R_S$  would be zero. Typical values for inorganic cells are  $R_{Sh}$  larger than 1000 Ohms and a few Ohms for  $R_S$ . These values can be different in organic devices due to the low mobility of carriers and charge recombination, increasing  $R_S$  and decreasing  $R_{Sh}$  respectively.

### 2.3.2 Important Parameters in Solar Cells

There are several parameters that are used to characterise the performance and mechanism of a solar cell, namely the open-circuit voltage ( $V_{oc}$ ), short-circuit current ( $I_{sc}$ ), the fill factor ( $FF$ ) and the power efficiency ( $\eta_e$ ). They are defined as follows:

- Open-circuit voltage ( $V_{oc}$ )

The voltage across the device when no current is flowing.

- Short-circuit current ( $I_{sc}$ )

The current produced by the device when there is no voltage across the device.

- Fill factor ( $FF$ )

The ratio of the maximum power output of the device  $(I.V)_{MAX}$  to the product of  $V_{oc}$  and  $I_{sc}$ .

$$FF = \frac{(I.V)_{MAX}}{V_{oc}.I_{sc}}$$

- Power conversion efficiency ( $\eta_e$ )

The ratio of the output electrical power to the incident light power

$$\eta_e = \frac{FF.V_{oc}.I_{sc}}{P_{inc}}$$

Where  $V_{oc}$  is in volts,  $I_{sc}$  is the current in  $\text{mA.cm}^{-2}$  and  $P_{inc}$  is related to the power of the incident light, in our case  $80 \text{ mW.cm}^{-2}$ .

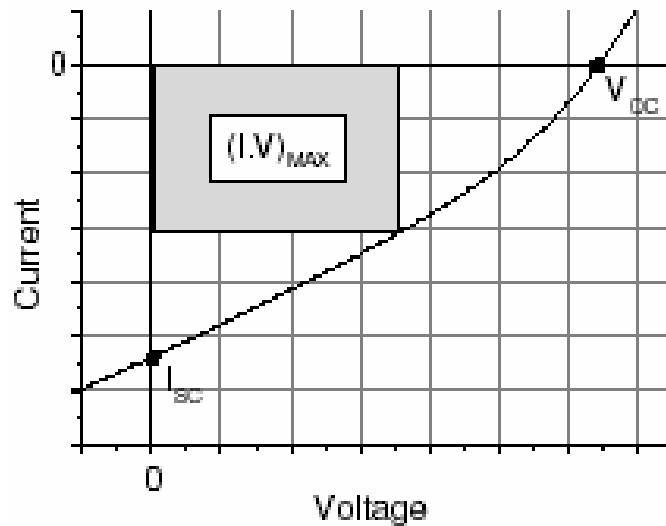


**Figure 2.4.** Sample I-V curve of a polymer photovoltaic cell showing  $V_{oc}$ ,  $I_{sc}$  and the maximum power rectangle  $(I.V)_{MAX}$ .

## 2.4 Annealing treatment

Considering that the most important aspect in organic photovoltaic devices is to get an efficient charge transfer between the donor material and the acceptor material, a good interaction in terms of dispersion is needed.

In this work the donor acceptor interface is studied in the vicinity of the glass

transition temperature of the polymer donor material (in our case, the polymer used was a regioregular poly(3-hexyl-thiophene-2,5-diyl), also named P3HT, with a glass transition temperature  $\sim 46^{\circ}\text{C}$ ). Measurements of the absorption, photocurrent spectra, I-V characteristics as well as calorimetric measurements are used to study the influence of heating processes.

Heat transfer and annealing treatment effects will be discussed.

### 2.4.1 Heat transfer

Heat can be transferred or transmitted by conduction, convection or radiation. Radiation is not taken into account due to the characteristics of the experimental set-up used for interdiffusion heating. The first two processes, conduction and convection will be described as follows.

#### Conduction

Heat conduction can be defined as the energy transport through a medium initiated by a thermal gradient. The kinetic energy in hotter regions is higher than in cooler areas, and thus, the energy can be transferred from hotter to cooler atoms.

When energy is transferred, a heat current  $H$  along the temperature gradient occurs.

$$H = \frac{dQ}{dt} = kA \frac{\Delta T}{L}$$

The heat transfer is defined as the passage of thermal energy through a volume of cross-sectional area  $A$ , of thickness  $L$  and where the temperature gradient is  $\Delta T$ .  $k$  is the thermal conductivity.

#### Convection

In the case of an interface between a solid surface and a moving fluid or gas at different temperature, apart from the heat transfer due to the internal vibrational energy of atoms there is also a heat transport due to the macroscopic motion of the bulk. There are different heat transfer velocities, near the interface the velocity is small due to random atomic motion, and further away the heat transfer due to the bulk motion will dominate. The heat current depends on the temperature difference between



the two phases (solid – fluid or gas) and the surface area as follows:

$$H = \frac{dQ}{dt} = h \cdot A \cdot \Delta T$$

Where  $h$  is called the convection heat transfer coefficient.

## 2.4.2 Annealing on a hot plate

The annealing procedure involved heating the samples on a hot plate at different temperatures is studied and each sample is analysed for higher efficiency and better photovoltaic responses – see high efficiencies photovoltaic devices in Chapter 6.

Notice that when we put a glass slide on a hot plate and it is in contact with a gas on the other side, the glass experiences a temperature drop. There are two different heat currents, one is the current flowing into the glass slide and the other is the current flowing out of the glass slide.

$$H_{int} = k_{glass} \cdot A \frac{T_{hp} - T_{surface}}{L}$$

$$H_{out} = h \cdot A(T_{surface} - T_{gas})$$

Where  $T_{hp}$  is the temperature of the hot plate and  $T_{surface}$  is the temperature of the glass at the air interface.

From the conservation of energy,  $H_{int}$  has to be equal to  $H_{out}$ ,

$$k_{glass} \cdot A \frac{T_{hp} - T_{surface}}{L} = h \cdot A(T_{surface} - T_{gas})$$

Therefore the temperature of the glass at the air interface is

$$T_{surface} = \frac{k_{glass} T_{hp} + h.L.T_{gas}}{k_{glass} + h.L}$$

Assuming that free convection occurs – since there is no forced air flow across the hot plate – the convection heat transfer coefficient is  $h=25 \text{ Wm}^{-2} \text{ K}^{-1}$ . The thermal conductivity of float glass is  $k_{glass} = 1 \text{ Wm}^{-1} \text{ K}^{-1}$ . The surrounding gas is at  $20 \text{ }^\circ\text{C}$ .

This last equation is very useful to determine the temperature that a film on a glass slide reaches during thermal annealing treatment.

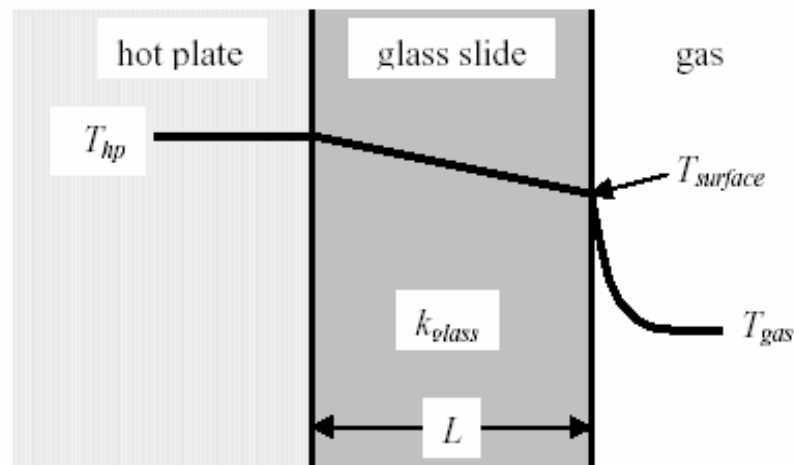


**Figure 2.5.** How the temperature drops if a glass slide is placed onto a hot plate.

As it can be seen in Figure 2.5, the temperature drops when a glass slide is placed onto a hot plate.  $T_{hp}$ ,  $T_{surface}$  and  $T_{gas}$  are the temperatures found on the hot plate, on the surface of the glass slide and in the gas zone respectively.

## 2.5 Conclusions

Many of the recent properties and developments on polymer solar cells have been reviewed in this Chapter. This part of the work summarizes the progress in photovoltaic devices from single layer (SL) photovoltaic devices to linear heterojunctions devices and also bulk heterojunctions devices. Photoinduced charge transfer from donor molecule to an acceptor molecule represents one of the most efficient processes in photovoltaic devices.

In order to characterise the photovoltaic cells used in this thesis, several parameters have been included explaining how important it is to know each parameter for a better understanding of photovoltaics.

It is seen that since the diffusion length in conjugated polymers is small, the shorter the path the charges have to cover the better photovoltaic response can be achieved, but this characteristic will be analysed more in detail in Chapter 5.

# CHAPTER 3 - MATERIALS AND EXPERIMENTAL BACKGROUND

## 3.1 Introduction

This chapter will outline the experimental procedures used in this thesis. In Section 3.2 the materials and their characterisation used in this work, such as polymers and carbon nanotubes, will be presented. This will be followed by the description and analysis of polymer nanotube composites preparation in Section 3.3. Finally, the different experimental techniques used will be presented in Section 3.4.

## 3.2 Materials

Materials with different functions were used in this work, from Indium Tin Oxide (ITO) substrates [18], donor polymers as poly[2,5-dimethoxy-(2'-ethylhexyloxy)-1,4-phenylenevinylene] (MEH-PPV) or Poly(3-hexylthiophene-2,5-diyl) (P3HT), to acceptor materials such as the Buckminsterfullerene C<sub>60</sub> or {6}-1-(3-(methoxycarbonyl)propyl)-{5}-1-phenyl-[5,6]-C<sub>61</sub> (commonly known as PCBM) [19]. Carbon nanotubes (both multi walled and single walled carbon nanotubes) were also used because of their good electron transport properties.

### 3.2.1 Indium-Tin-Oxide (ITO) coated glass

Indium Tin Oxide (ITO) coated glass slides were purchased from UQC Optics, Limited (Cambridge, England, <http://www.uqgoptics.com/>) [18]. The slides purchased consisted of 12mm x 12mm unpolished flat glass coated with approximately 120nm of ITO deposited on one side by a sputtering process with a sheet resistance of 8 to 12  $\Omega/\square$ . Note that we needed to be sure the surface of ITO was facing up before spin casting films on top.

Atomic force microscopy measurements showed that the ITO coated glass slides received were relatively smooth with roughness of the order of a few nanometres (see Figure 3.1).

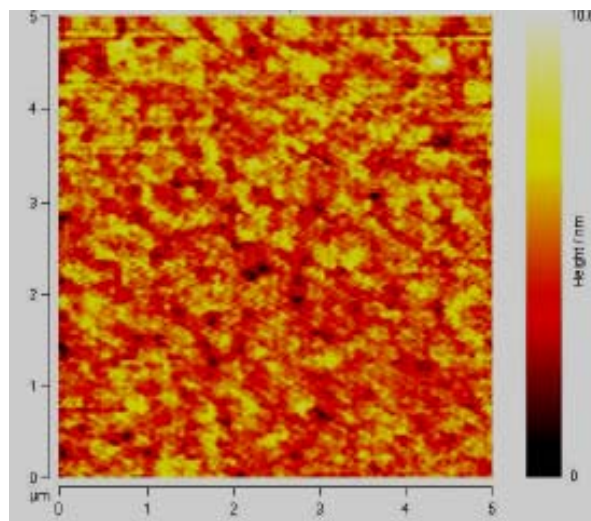


**Figure 3.1.** Atomic force microscopy image of the surface of the ITO glass slides.

The UV-vis absorption spectrum, see Figure 3.2, shows that the ITO glass slide allows the transmission of light down to 350nm, at which wavelength the flat glass begins to heavily absorb.

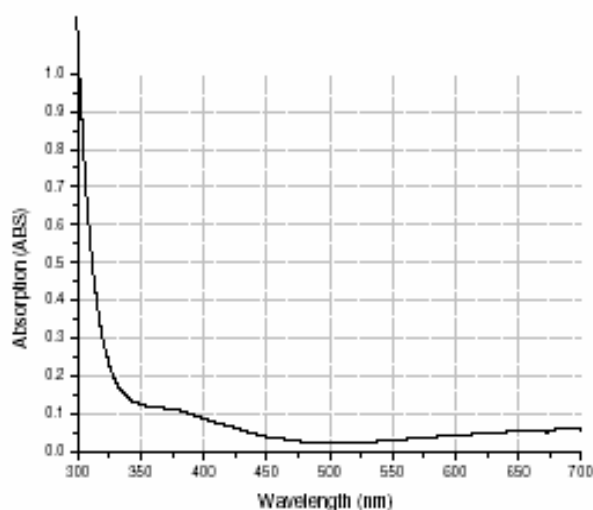


**Figure 3.2.** UV-Vis absorption spectrum of an ITO glass slide.

### 3.2.2 Electron donor MEH-PPV

One of the main conjugated semiconducting polymers used in this work is poly[2,5-dimethoxy-(2'-ethylhexyloxy)-1,4-phenylenevinylene] (MEH-PPV), which was used as the active layer in solar cells. It was chosen because of its particularly electron donor properties. It can be used for fabrication of light emitting displays, organic solar cells and biosensors. MEH-PPV has a small band gap of around 2.1 eV

and exhibits good mobility properties for electrons and holes. The mobility of the hole and the electron of MEH-PPV are  $\sim 10^{-6}$  and  $\sim 10^{-8}$   $\text{cm}^2/\text{Vs}$ , respectively. Chlorobenzene was used to make solutions of this particular polymer. MEH-PPV was purchased from American Dyes Source (Quebec, Canada, <http://www.adsdyes.com/>) [19].

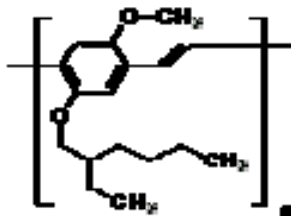


**Figure 3.3.** Repeat unit of the polymer MEH-PPV.

### 3.2.3 Electron donor P3HT and P3OT

Poly (3-hexylthiophene-2,5-diyl), hereafter referred to as P3HT, and Poly (3-octylthiophene-2,5-diyl), referred to as P3OT, are semiconducting polymers that have been intensely studied in photovoltaic device applications. Chloroform was the solvent used to prepare solutions of these two particular polymers.

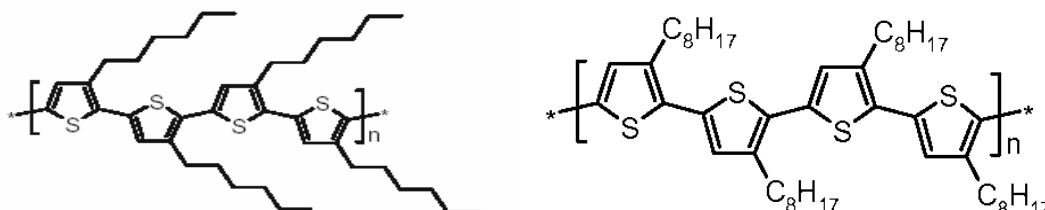


**Figure 3.4.** Repeat units of the polymers P3HT (left) and P3OT (right).

P3HT and P3OT were purchased from American Dyes Source (Quebec, Canada, <http://www.adsdyes.com/>) [19].

### 3.2.4 Hole transport PEDOT:PSS

Baytron P, the commercial aqueous dispersion of the conducting polymer PEDOT (Poly (3,4-ethylenedioxythiophene)) with PSS (polystyrenesulfonic acid).

PEDOT:PSS is excellent for transporting holes to the ITO anode. PEDOT:PSS films were prepared by spin coating at 2000 rpm and then drying under flowing nitrogen for at least 5 minutes at 120°C. PEDOT:PSS was supplied by Bayer, Leverkusen, Germany (<http://www.bayer-chemicals.com/>) [19].

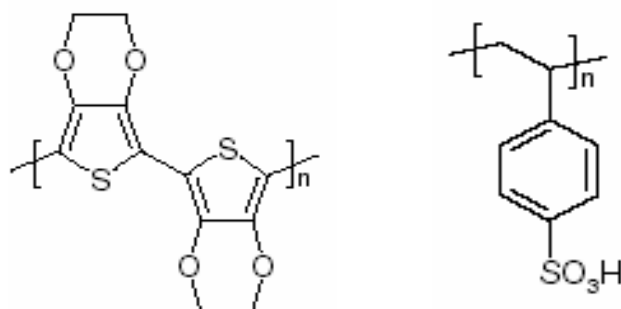


**Figure 3.5.** Chemical structures (left to right) of PEDOT and PSS.

### 3.2.5 Electron acceptor fullerenes C<sub>60</sub> and PCBM

Buckminsterfullerene C<sub>60</sub> is used as an electron accepting material in this work. This particular name was chosen from the architect R. Buckminster Fuller whose geodesic dome consisting of pentagonal and hexagonal structures provided a guide to the hollow cage structural hypothesis.

The general name, fullerene, has been adopted for all similar hollow shell carbon molecules C<sub>n</sub> closed by twelve pentagons. This particular acceptor material has been studied due to its ultra fast charge transfer, relative to other acceptor electrons such as Iron or nitrate. The HOMO level in C<sub>60</sub> is 6.1 eV and the LUMO level is 3.7 eV resulting in a HOMO-LUMO gap energy of 2.4 eV. This fullerene C<sub>60</sub> was added into the semi conducting polymer MEH-PPV using chlorobenzene as a solvent.

Further studies have shown the photo-induced electron transfer between conjugated polymers and C<sub>60</sub> to be ultra fast, metastable, reversible and with a quantum efficiency approaching 100 %.

PCBM ((6,6)-phenyl-C61-butyric acid) was also used as an acceptor material as well and transports electrons to the Aluminium cathode. This particular material is a derivative of the fullerene C<sub>60</sub> and exhibits good photovoltaic responses when is mixed with semi conducting polymers like MEH-PPV and P3HT. PCBM was purchased from American Dyes Source (Quebec, Canada, <http://www.adsdyes.com/>) [19]. Most of the concentration ratios used were 1:1 (polymer:fullerene) in weight.

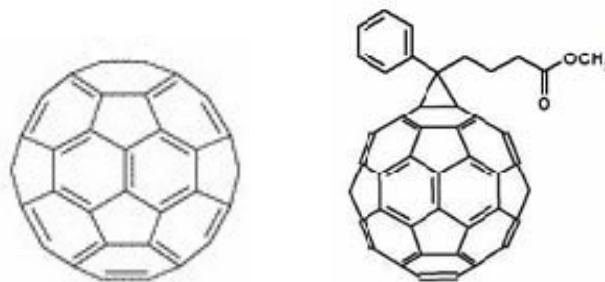


**Figure 3.6.** Chemical structures of C<sub>60</sub> (left) and PCBM (right) fullerenes.

Concentration ratios of C<sub>60</sub> and PCBM employed will be stated in Chapter 5.

### 3.2.6 Carbon Nanotubes

A carbon nanotube is an allotrope of carbon along with diamond, graphite and fullerenes. Diamond and graphite are the two well known forms of crystalline carbon. Diamond is a tetrahedral 3d matrix of sp<sup>3</sup> bonded carbon atoms and graphite consists of sheets of carbon atoms, with each atom sp<sup>2</sup> bonded to 3 other carbon atoms. The new carbon allotrope, fullerene, has five and six member rings of carbon coming together in a spherical structure. The best known example is C<sub>60</sub> with a truncated icosahedral structure formed by 12 pentagonal rings and 20 hexagonal rings; Figure 3.7 shows the fullerene C<sub>60</sub>.

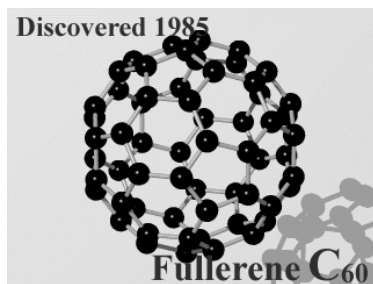


**Figure 3.7.** Schematic image of C<sub>60</sub>.

Fullerenes were discovered by Kroto *et al.* [20] in 1985 while investigating carbon present in interstellar space.

In 1990, Kratschmer *et al.* [21] found the soot produced by arc discharge of graphite electrodes contained C<sub>60</sub> and other fullerenes. It was the beginning of fullerene production in high quantities in the laboratory.

In 1991 Ijima and co-workers [22] observed that nanotubes of graphite were deposited on the negative electrode during the direct-current arcing of graphite for the

preparation of fullerenes. These nanotubes were concentric cylinders of graphite capped with half fullerenes. Nanotubes can be single-walled (SWNT) containing only one tube or multi-walled (MWNT) containing many concentric tubes surrounded by graphitic layers separated by few angstroms. Only multi-walled nanotubes were used in this work, see Chapter 7.

The simplest possible single-walled carbon nanotube can be visualised by cutting the  $C_{60}$  structure across the middle and adding a cylinder of graphite with the same diameter. Figure 3.8 shows the models of the three different types of nanotubes that can be formed.

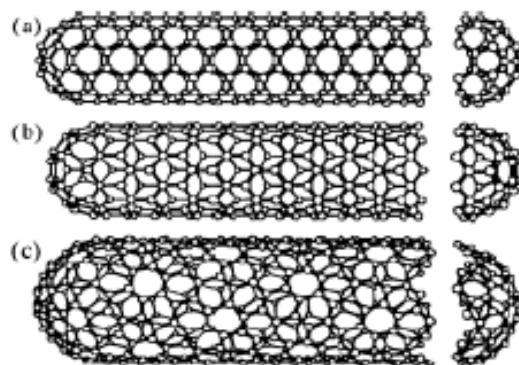


**Figure 3.8.** Models of (a) armchair, (b) zigzag, and (c) chiral nanotubes.

Nanotubes can be defined by a chiral angle  $\theta$  and a chiral vector  $C_h$  given by the following equation where  $j_1$  and  $j_2$  are unit vectors in a two dimensional graphene lattice and  $n$  and  $m$  are integers.

$$\vec{C}_h = n \cdot \vec{j}_1 + m \cdot \vec{j}_2$$

A number of possible chiral vectors can be specified by the last equation in terms of integer pairs  $(n,m)$ . Each pair defines different ways of rolling the graphene sheet to form a carbon nanotube of a certain chirality. Figure 3.9 shows the variables used to parameterise the hexagonal lattice that can be rolled to form nanotubes.

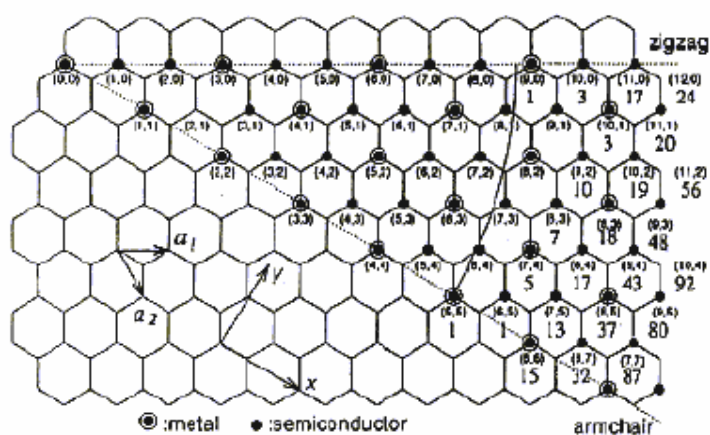


**Figure 3.9.** 2D graphene sheet showing chiral vector  $C_h$  and chiral angle  $\theta$ .



## Electrical properties of carbon nanotubes

Depending on the chiral vector, carbon nanotubes with a small diameter are either semi-conducting or metallic. The differences in conducting properties are due to the molecular structure that results in a different band structure and thus a different band gap. The band gap decreases with increasing diameter, making large diameter nanotubes and MWNT metallic.

The armchair structure is one of the 3 possible zigzag structures. These metallic zigzag tubes will have  $m$  and  $n$  such that  $|m-n| = 3q$  where  $q$  is an integer [23]. In strict terms only armchair tubes  $(m,n)$ , i.e. those nanotubes with  $q=0$  in the above equation, are metallic, in that they have bands crossing at the Fermi level. For those zigzag tubes that satisfy the above equation an infinitesimally small band gap is induced by the curvature of the hexagonal lattice. As this is much smaller than  $kT$ , electrons can be excited thermally at room temperature and these tubes thus act like metals. For nanotubes where  $m-n \neq 3q$  lattice curvature induces a larger band gap and so these tubes are semiconducting. As this gap is lattice strain induced, it decreases as the diameter increases as the tube gets more graphene like. This is described by the following equation:

$$E_{gap} = \frac{2a\gamma_0}{d}$$

Where  $\gamma_0$  is the C-C tight binding overlap energy,  $a$  is the distance between two neighbouring carbon atoms and  $d$  is the diameter of the carbon nanotube. This has been measured by scanning tunnelling spectroscopy (STS) [24] which gives a value of  $\gamma_0=2.7$  eV in good agreement with 2.5 eV for a single graphene sheet [25].

Figure 3.10 illustrates an armchair carbon nanotube with different behaviour.

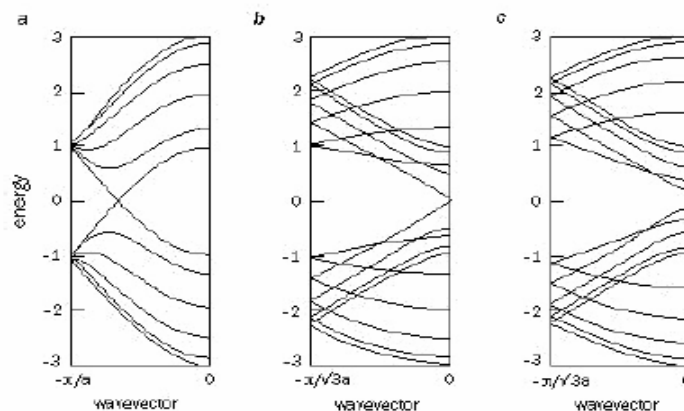


**Figure 3.10.** Band structure for single walled carbon nanotubes. (a) Metallic nanotube, (b) semi-conducting nanotube with zero bandgap acting as a metallic tube at all temperatures above absolute zero and (c) a semi-conducting nanotube with a band gap.

## Mechanical properties of carbon nanotubes

Carbon nanotubes have a very large Young's modulus in their axial direction. The nanotube as a whole is very flexible because of the great length. Therefore, these compounds are potentially suitable for applications in composite materials that need anisotropic properties [26, 27].

Impressive mechanical properties were theoretically predicted for carbon nanotubes long before the first experiments were possible. Overney et al calculated a Young's modulus ( $Y$ ) of 5 TPa for SWNT in 1993 [28]. In 1999 Srivastava et al [29] computed the critical stress of a SWNT to be 153 GPa for a 12% compressed nanotube in good agreement with a measured value of 135 – 147 GPa by Lourie et al [30]. Lourie's analysis required assuming a conservative  $Y$  value of 1.2 TPa for nanotubes based on another relatively early experiment carried out by Treacy in 1996. That experiment to evaluate  $Y$  for MWNT was a TEM method where one end of the nanotube was effectively clamped at the edge of a grid while an oscillating deflection was induced at the other end. A model was applied to the magnitude of deflection and calculations yielded  $Y = 1$  TPa. More recent experiments [31] in 1998 using Raman Spectroscopy have measured a value of  $Y = 2$  TPa for a MWNT and 3 TPa for a SWNT. The approximate agreement between these theoretical and measured values is encouraging research worldwide to focus on the potential of carbon nanotubes as reinforcing fillers.

## Carbon nanotube production methods

Carbon nanotubes can be produced by arc discharge, chemical vapour deposition or laser ablation.

In arc discharge, carbon nanotubes are readily prepared by striking an arc between graphite electrodes in 2-3 atm (~500 Torr) of helium, considerably higher than the pressure of helium used in the production of fullerene soot. A current of ~100 Amps across a potential drop of about 25 V gives high yields of carbon nanotubes. The arcing process can be optimised such that the major portion of the carbon anode is deposited on the cathode in the form of carbon nanotubes.

Chemical Vapour Deposition (CVD) is used to grow carbon nanotubes. This technique was the one used in this work and it will be explained in more detail in Section 3.4.6.

Laser Ablation is a very costly method that produces SWNT's by focussing a laser on a graphite target in an argon atmosphere. This gives a typical yield of around 70% and varying the temperature of the furnace gives the advantage of better diameter control.

### 3.3 Polymer and carbon nanotube/fullerene composites

#### 3.3.1 Characterization of carbon nanotubes

The carbon nanotubes used during this work were produced by catalytic vapour deposition and were functionalised with –OH. These nanotubes were purchased from Nanocyl S.A. (Sambreville, Belgium, <http://www.nanocyl.com/>) [19].

Characterisation		
		Method of measurement
Average inner diameter	<b>4</b> nm	TEM
Average outer diameter	<b>15</b> nm	TEM
Lengths	Up to <b>50</b> $\mu$ m	TEM

Composition			
	Crude (wt. %)	Purified (wt. %)	Method of assay
Carbon Purity	> <b>80</b>	> <b>95</b>	TGA
Impurities			
Metal oxide	< <b>20</b>	< <b>5</b>	PIXE, TGA

**Figure 3.11.** Characteristics of thin multi-walled carbon nanotubes used during this work. Nanotubes purchased from Nanocyl S.A.

#### 3.3.2 Preparation of composites

Thin multi-walled nanotubes were added into a polymer solution and agitated using a high power ultrasonic tip for five minutes. Different concentrations of nanotubes were added into the polymer solutions. This is used to break up and disperse the large aggregates present in the nanotube powder. But if we leave this polymer nanotube composite for a long time in the sonic tip we can break up the

nanotubes as well. For this reason, and to ensure good dispersion, our solution is placed in a sonic bath and sonicated for two hours.

After this last sonication it is necessary to allow the solution to settle during one day or so, and after this, most of the impurities will be precipitated.

The last stage is the decantation of the top two thirds to yield a composite of organic material, a large amount of nanotubes and very little extraneous carbonic material. The rest of the solution and impurities are left in the bottom of the original sample bottle.

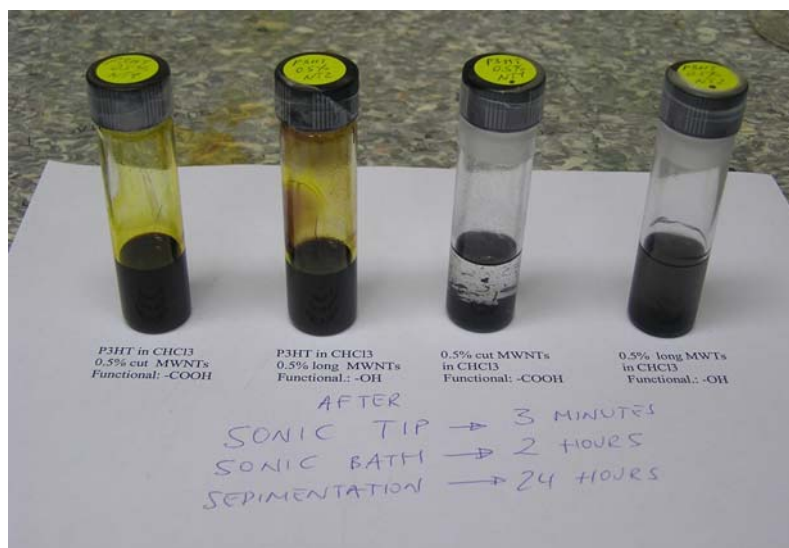


**Figure 3.12.** Picture of samples of different composites solutions.

Polymer and fullerene composites, such as P3HT:PCBM do not need to be ultrasonically agitated using a higher power sonic tip, a good dispersion of the polymer fullerene composite (e.g.: P3HT:PCBM composite) can be got by leaving the solution in a sonic bath for 20 minutes. Multiwalled nanotubes were also dispersed into the P3HT:PCBM solution using ultrasonic tip and ultrasonic bath.

## 3.4 Experimental equipment

### 3.4.1 Glove box, I-V and photocurrent spectroscopy setup

Figure 3.13 represents a diagram of the glove box. It has five gloves and two air locks, one at either end of the box. The gloves are organised into two pairs, this pairing allows for simultaneous device testing and device fabrication. The fifth glove

is located in the manual airlock compartment at the far left and is used for mounting samples into the vacuum system.

Nitrogen is supplied to the glove box and the gas can be controlled using the four flow meters on the front. The flow meters control the humidity of the glove box and the display panel gives a measurement of the humidity in terms of the dew point inside the box. The dew point is the temperature at which that amount of humidity will condense and is related to the percentage of water concentration. The glove box usually runs at a dew point between  $-30\text{ }^{\circ}\text{C}$  and  $-40\text{ }^{\circ}\text{C}$  corresponding to a water concentration of 0.3% - 0.1%.

All the measurements and analysis were performed under nitrogen atmosphere.



**Figure 3.13.** Glove Box used for electrical measurements (School of Mathematical and Physical Sciences, University of Newcastle, Australia).

Current-voltage (IV) curves and short-circuits photocurrent action spectra (Spectral Response, SR) can be taken inside the glove box. Devices are slotted into a special mount that addresses each of the electrodes. Care should be taken to ensure that the pins coincide with the ITO pads on the device as some tolerance has been allowed for slight variations in substrate size.

These electrodes are wired via an electrical feed-through to test and measurement equipment external to the glove box. A switching box is used to select the device under test and the measurement to be performed (IV or SR).

Spectral responses (SR) curves were taking using the HP-Vee program. The light source for the SR measurements is external to the glove box, mounted on an optical board on the glove box's roof. White light from a 12 V 100 W tungsten lamp

is chopped by a chopper, passed through a computer controlled Oriel monochromator and fed via fibre bundle into the glove box. From the exit of the fibre bundle it diverges before being focused via lens onto the sample and in particular onto a determined device.

SR measurements require the lock-in, monochromator, chopper, lamp power supply and lamp fan to be switched on. The schematic of the experimental setup is shown in Figure 3.14.

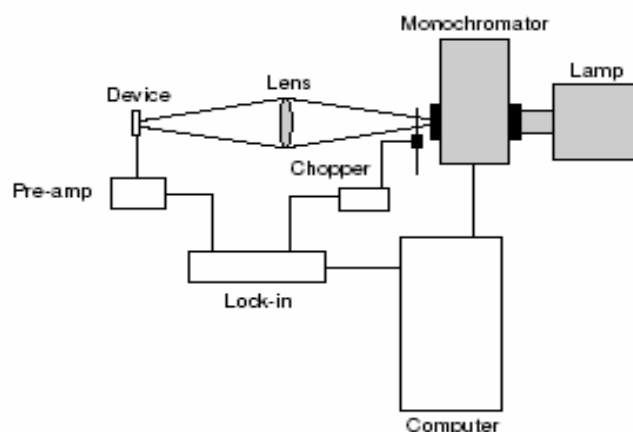


**Figure 3.14.** Schematic of the experimental setup used for taking short-circuit photocurrent spectra (School of Mathematical and Physical Sciences, University of Newcastle, Australia).

### 3.4.2 Profilometry

Film thickness was measured using a Tencor Alpha-Step 500 surface profilometer (School of Mathematical and Physical Sciences, University of Newcastle, Australia). Polymer films for measurements were spin-coated onto glass substrates. Steps were created in the polymer film by scratching a short strip of polymer using the end of a pair of stainless steel tweezers. Care was taken to ensure that there was no damage to the underlying substrate (avoid scratching the glass substrate surface). The thickness of each film was measured in at least two or three different positions and the thickness average was taken. To confirm reliable measurements we also checked the thicknesses of films using atomic force microscopy (AFM) measurements.

### 3.4.3 Absorption spectroscopy

Absorption spectroscopy was performed using a Shimadzu UV-Vis spectrophotometer and computer controlled using WinUV software. This instrument has a double beam, direct ratio photometric measuring system using a dynode feedback method.

### 3.4.4 Atomic force microscopy

Atomic force microscopy (AFM) images of films were taken with a Digital Instruments Nanoscope microscope operating in contact mode and tapping mode. The AFM used was a Multimode Nanoscope IIIA purchased from Veeco.

Originally, AFM used a sharp diamond tip that was attached to a flexible cantilever and placed close to a sample surface. The STM tip, kept at a constant distance from the cantilever, was used to determine the vertical movement of the cantilever, and so the forces experienced by the cantilever could be measured using Hooke's Law. The AFM cantilever was deflected due to the interaction forces between the tip and the surface while the tip was in contact with the surface. A feedback loop was used to keep the force acting on the tip constant and the tip was scanned across the surface producing a topographic image. The deflected beam is detected by a photomultiplier array and the voltage output is then converted into cantilever deflection via calibration process.

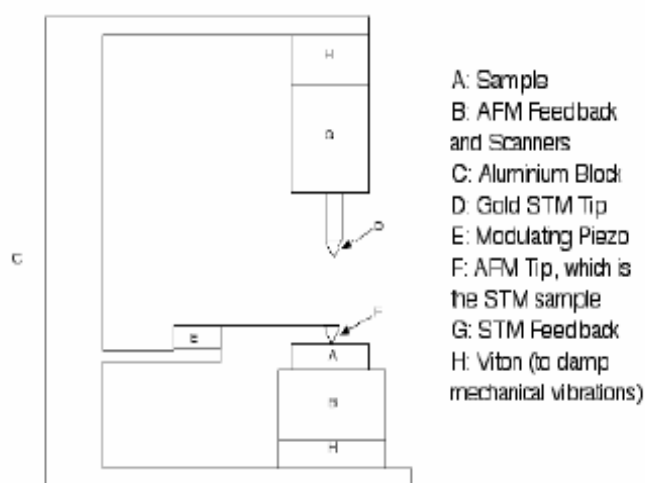


**Figure 3.15.** AFM design.

For the AFM of the samples in this thesis, the height and phase images were obtained simultaneously operating in the tapping mode under ambient conditions.

### 3.4.5 Differential scanning calorimetry

Differential Scanning Calorimetry (DSC) is an advanced technique which measures the heat flow through our samples when the sample is heated at a controlled temperature rate. DSC analysis is taken from the characteristics of the material depending on whether the material is amorphous or crystalline. If the material is amorphous, a shift in the heat flow will be observed when the amorphous chains are given enough thermal energy to facilitate movement of chains. The temperature at which this change in material properties occurs is referred to as the glass transition temperature,  $T_g$ , when the material changes from a rigid state to more rubbery state as the chains become more flexible.  $T_g$  is observed as a small endothermic transition as the sample absorbs the heat. If the material is crystalline, the change in the heat flow is observed as the crystals melt or crystallise. Since the melting is an endothermic process, a peak in the heat flow occurs before returning to the baseline upon termination of melting. Conversely, crystallisation appears as an exothermic peak.

There parameters used to describe DSC experiments are, the glass transition ( $T_g$ ), the melting point ( $T_m$ ), the crystallisation time and temperature ( $T_c$ ) and the percentage of crystallinity.

To find the percentage of crystallinity, the area of the  $T_c$  and  $T_m$  peaks is considered. The area under the DSC curve is being used to calculate the enthalpy required to melt ( $\Delta H_m$ ) or crystallise ( $\Delta H_C$ ) the sample.

As we discussed before, melting is observed as an endothermic peak on the heat scan. Crystallisation comes from an exothermic peak on the cooling scan.

The crystalline fraction of our samples can be calculated using the following equation

$$\chi = \frac{\Delta H_m}{\Delta H_{100\%}}$$

Where  $\Delta H_{100\%}$  is the enthalpy of melting of a theoretical 100% crystalline sample. Also, the crystallinity can be calculated using the ratio between the melting enthalpy value of the polymer and the melting enthalpy value of the composite.



### 3.4.6 Chemical Vapour Deposition

Chemical Vapour Deposition (CVD) is a technique used to grow carbon nanotubes. A substrate is placed in the oven as shown in figure below at high temperatures from 600°C to 1100°C and a carbon containing gas such as acetylene ( $C_2H_2$ ) is slowly flowed into the furnace with combination of an active gas as argon (Ar). During the process the gas decomposes and recombines to grow as nanotubes. A catalyst can be put onto the substrate to increase efficiency and growth positioning control.

Two different CVD setup were used during this work. The one used in Trinity College consists of a quartz glass tube and only one furnace and the one used in Wollongong University (Figure 3.16 below) consists of a quartz glass tube and a dual furnace fitted with independent temperature controllers. In the Trinity set-up carbon nanotube forests with any orientation are grown, but using the one in Wollongong, oriented aligned carbon nanotubes with lower thicknesses can be grown. Note that large quantities of carbon nanotubes can be produced on a substrate simultaneously, with a high degree of morphological control. In fact, in the past year inventive methods have illustrated the possibility of control over growth, position, and direction of carbon nanotubes [32, 33, 34, and 35].

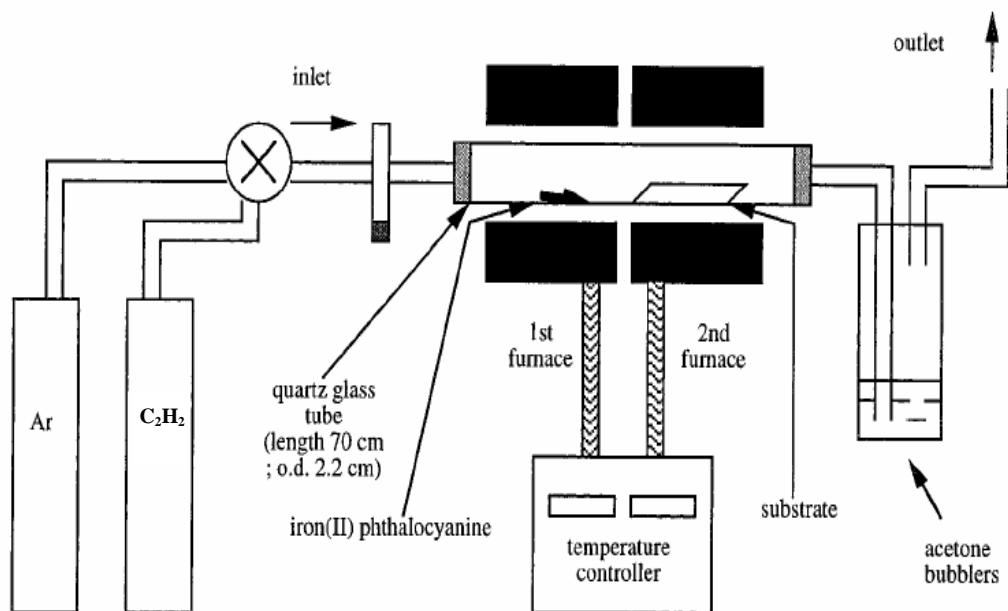


**Figure 3.16.** Chemical Vapour Deposition (CVD) set-up for the generation of aligned carbon nanotubes by pyrolysis of FePc. IPRI (Intelligent Polymer Research Institute, University of Wollongong, Australia).

### 3.5 Conclusions

Materials' preparation as well as characterisation technique used in this work was presented in this Chapter.

Polymers such as MEH-PPV or P3HT were purchased from American Dyes Source (Quebec, Canada, <http://www.adsdyes.com/>).

The multi-walled carbon nanotubes were prepared by chemical vapour deposition in our laboratory and also thin multi-walled carbon nanotubes were purchased from Nanocyl S.A. (Sambreville, Belgium, <http://www.nanocyl.com/>) and then used in a polymer nanotube composite form.

The device structure tested in this work was formed from ITO, polymer composites and aluminium on top. Organic photovoltaic devices were characterised using all the equipment required, such as the glove box, where we found current-voltage and spectral response setups, and also absorption spectroscopic studies were carried out in order to understand the optical properties of these devices.

# CHAPTER 4 - SAMPLE PREPARATION AND CHARACTERIZATION PROCEDURES

## 4.1 Introduction

In this Chapter the preparation of polymer solutions and how to make photovoltaic devices will be described. Device fabrication and characterisation will also be discussed. Basically, polymer solar cells were fabricated by spin casting different polymer solutions on ITO substrates and by thermally evaporating aluminium electrodes on top.

## 4.2 Preparation of sample films

### 4.2.1 Substrate preparation

ITO (Indium Tin Oxide) coated glass substrates were used in this work. ITO was used as an anode (injecting holes) because of its transparency, low resistivity ( $5\Omega/\text{m}$ ) and high work function (4.8 eV). 12 mm x 12 mm pieces of ITO coated glass substrates purchased from UQC Optics, Limited (Cambridge, England, <http://www.uqgoptics.com/>) were used [36]. The substrates were etched using an etching technique with acid solutions in order to obtain continuous strips of ITO. Afterwards, the substrates were cleaned in a surfactant, Decon 90, to remove any grease, then they were rinsed in acetone and deionised water solutions. After drying all slide substrates were left in isopropyl alcohol until required.

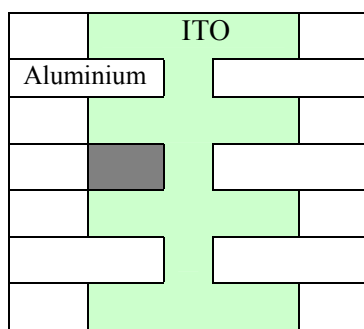


**Figure 4.1.** Top view of device architecture of polymer solar cells. The photovoltaic area ( $0.04\text{ cm}^2$ ) of one of the six devices used in each sample (grey coloured area) is shown.

## 4.2.2 Solution preparation

Different solutions were prepared in this work. MEH-PPV and P3HT, described in previous section 3.2, were mixed in solvents to prepare solutions required to make devices. Chlorobenzene was the solvent used for MEH-PPV and chloroform was used for P3HT. The most common concentration used was 10 g/l and all solutions were sonicated in the sonic bath before use.

## 4.2.3 Spin coating of polymer films

There are different methods for producing organic films: spin coating, drop casting, thermal evaporation, etc. The films of polymers used here were prepared using spin coating from the polymer solutions. The spin coater used was a Convac 1001. The films were spun in the glove-box using different spin speeds of between 500 rpm and 3000 rpm to get different layer thicknesses. In general, the thickness of the spin-coated film is determined by the spin-speed and solution viscosity.

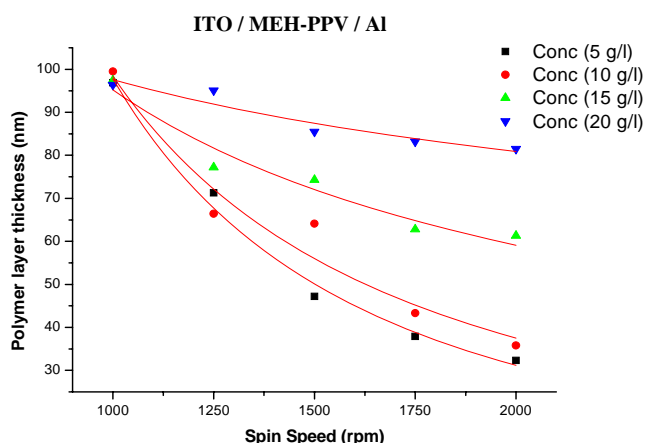


**Figure 4.2.** MEH-PPV film thickness as a function of different spin casting speeds for four concentrations. Results reproduced from laboratory work.

Figure 4.2 shows the polymer films thicknesses as a function of spin casting. Other parameters such as the acceleration rate do not affect the film thickness [37].

The thickness of each film can be calculated from the following equation :

$$t = A.f^{-b}$$

Where  $t$  is the film thickness,  $A$  is a function of the concentration,  $f$  is the spin speed and  $b$  is a constant approximately equal to 1/2 [38].

## 4.3 Sample design and construction

### 4.3.1 General device structure

The general device structure of organic solar cells devices studied in this work was described in previous section 4.2.1 and is shown again in the Figure 4.3 below. The active layer is sandwiched in between the anode (ITO) and cathode (Aluminium) electrodes. Illumination of the devices would be through the anode ITO.

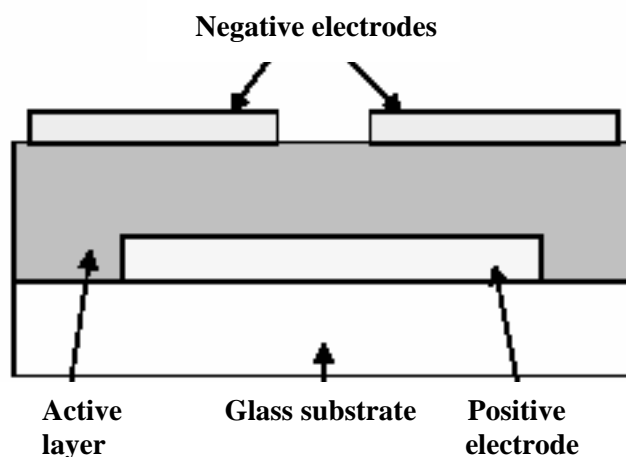


**Figure 4.3.** General device structure for photovoltaic devices.

This choice of making devices is very common for photovoltaic devices, but is not the only one possible. Note the importance of the work functions of the positive and negative electrodes indicating the direction of charge transport. Here, in order to obtain improved absorption of light, transparent electrodes were used.

### 4.3.2 Device construction

The generic device architecture used throughout this project was the single layer sandwich structure, with one layer of photo-active material sandwiched between ITO and a vacuum evaporated metal film. The active polymeric layer was deposited by spin-coating onto prepared 12 mm x 12 mm patterned ITO substrates. In order to ensure clean, particle free films all spin coating were performed in the glove box.

The ITO was patterned or coated in order to form six devices per substrate, with each device being the overlap between the ITO and the top aluminium electrode

(see Figure 4.1). The top metal electrode was deposited by vacuum evaporation through a mask. The thicknesses of these top electrodes layers were between 50 to 100 nm. Also thin semi-transparent aluminium electrodes were prepared in order to perform photovoltaic device characterisations through this electrode.

### **4.3.3 Metal deposition**

Metal deposition of thin (30-40 nm) films of aluminium was carried out in a purpose built high-vacuum chamber with a base of  $10^{-6}$  mbar. High purity metals (99% for aluminium) were deposited by thermal evaporation.

## **4.4 Device characterisation**

### **4.4.1 Current-voltage measurements**

Current-voltage (IV) curves were measured using computer driven custom made electronics controlled by HP-Vee software. IV curves were acquired by sweeping the voltage applied to the devices while recording the current produced by the device. The voltage applied to the devices was typically swept at a rate of 200 mV/s.

Simulated sunlight for testing in photovoltaic mode was provided by a Solux MR16W quartz halogen lamp which has a spectral profile similar to the one shown in the figure 4.4 and with a range of light from 400 to 500 nm.

Cells were placed at 30 cm from the lamp so that  $\sim 80 \text{ mW/cm}^2$  of white light was incident directly on the cells when 12V was applied, as measured by a power meter. The I-V characteristics of each device was plotted using a graphing program.

A reference solar spectrum is shown in Figure 4.4.

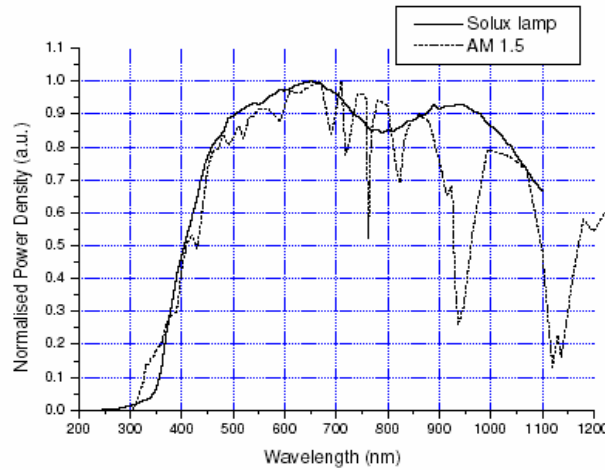


**Figure 4.4.** Spectral profile of a Solux lamp compared to the AM 1.5 solar mass spectrum (own data). (The AM 1.5 spectrum is the standard spectrum, at  $1000 \text{ W/m}^2$  irradiance, used in the testing of solar cell devices).

#### 4.4.2 Photocurrent spectroscopy. Spectral response

The experimental setup is as described in Section 3.4.1. The short-circuit current was measured as function of the wavelength (nm). A tungsten halogen lamp was used as the broad-spectrum light source (Osram 12 V 100 WHLX 64625, housed in an Oriel 66057 lamp housing) and passed through a monochromator (Oriel Cornerstone 130) and chopper (Rofin-Sinar 7020) to give a modulated monochromatic light of variable wavelength. The short-circuit current from the device was then measured by feeding the signal from the device into current to voltage converter and amplifier (that holds the device at short-circuit) and then into a lock-in amplifier (Ithaco Dynatrac 395) referenced to the chopper frequency. Data acquisition and monochromator control was carried out by a computer running custom written DT-VEE software. The spectral response of the source-monochromator system was measured using a calibrated silicon photo diode (Newport 818-SL head and 840 meter) pointed at our device for recording and monochromator system was automatically corrected for in our device measurements using the DT-VEE software.

#### 4.4.3 Absorption analysis

Absorption spectroscopy involves measuring the absorption of the material as a function of wavelength over a range extending from the infrared to ultraviolet. The absorption is usually measured in reference to a blank sample in a double beam

arrangement, to eliminate variations caused by the differences in lamp intensities at different frequencies. As photons pass through a material, it is possible that photons of a suitable energy can interact with the material, resulting in an electron being excited to a higher energy state, and the photon being absorbed. By measuring the amount of light absorbed for a particular wavelength, it is possible to deduce information about the electronic structure of the material.

#### **4.4.4 Surface microscopy analysis**

##### **SEM (Field Emission Scanning Electron Microscopy)**

Field Emission Scanning Electron Microscopy of gold-coated samples was analysed on a Hitachi S-4300 Scanning Electron Microscope. The SEM shows very detailed 3-D images at higher magnifications. For the samples to be analysed, it is necessary to have the sample in a vacuum inside the microscope. The samples are coated with a very thin layer of gold by a sputter coater. An electron beam is scanned across the sample required for analysis, secondary electrons are knocked out from the surface, and then a detector counts these electrons and send the signals to an amplifier. The final image comes from the number of electrons emitted from the sample at each position where the beam was scanned.

##### **AFM (Atomic Force Microscopy)**

Atomic force microscopy (AFM) images of films were taken with a Digital Instruments Veeco microscope operating in tapping mode. Using tapping mode characterisation AFM operates in ambient air by scanning a tip attached to the end of an oscillating cantilever across the sample surface. The cantilever is oscillated at or near its resonance frequency with an amplitude ranging typically from 20nm to 100nm. By maintaining a constant oscillation amplitude, a constant tip-sample interaction is maintained during imaging. The oscillating tip is then moved toward the surface until it begins to lightly touch, or “tap” the surface. As the oscillating cantilever begins to intermittently contact the surface, the cantilever oscillation is necessarily reduced due to the energy loss caused by the tip contacting the surface. The reduction in oscillation amplitude, compared to a constant oscillation amplitude, is used to identify and measure surface features. When the tip passes over a bump in the surface, the cantilever has less room to oscillate and the amplitude of oscillation



decreases. Conversely, when the tip passes over a depression, the cantilever has more room to oscillate and the amplitude increases.

Images are generated by mapping the vertical distances that the scanner moves to maintain the constant amplitude during scanning. Typical scan speeds during recording were 0.3-1 lines/s using scan heads with a maximum range of  $16 \times 16 \mu\text{m}^2$ . The phase images represent the variations of relative phase shifts and are thus able to distinguish materials by their elastic properties.

#### **4.4.5 Calorimetry measurements**

5.8 mm aluminium disk pans were used for Differential Scanning Calorimetry analysis (DSC). Each disk was found to weigh  $4.0 \pm 0.3$  mg and two disks were used in the calorimetric measurements. Samples were dried in the oven in order to remove the solvent and were prepared by carefully placing the film disks into the aluminium sample pan in layers to ensure maximum thermal transfer through the entire sample. Flowing helium gas was employed to purge any remaining solvent in the sample.

Our samples were heated from  $0^\circ\text{C}$  to  $280^\circ\text{C}$  at a rate of  $40^\circ\text{C}/\text{min}$  and held at  $280^\circ\text{C}$  for one minute to allow the system to equilibrate before controlled cooling to  $0^\circ\text{C}$  at  $40^\circ\text{C}/\text{min}$  using a controlled liquid nitrogen feed. A hold step of one minute was applied at  $0^\circ\text{C}$  before a second heating scan was started from  $0^\circ\text{C}$  to  $280^\circ\text{C}$  at  $40^\circ\text{C}/\text{min}$  to ensure that no solvent or residual particles are still in our composite. A consistent baseline using empty sample pans was obtained before taking all measurements.

### **4.5 Conclusions**

Sample preparation as well as all experimental methods studied in this work were presented in this chapter. All the preparations needed in order to get all the samples ready to test were discussed. Substrate and solution preparation, spin coating and metal deposition were the main processes required to produce organic PVs.

I-V measurements, spectral responses (SR), absorption spectroscopy characterisation (UV-vis), Scanning Electron Microscope (SEM), Atomic Force Microscopy (AFM), Differential Scanning Calorimetry (DSC) were the methods used in this work to get a global analysis, evaluation and characterisation of the samples.

# **CHAPTER 5 – LOW EFFICIENCY MEH-PPV PHOTOVOLTAIC DEVICES**

## **5.1 Introduction**

MEH-PPV is a good hole transporting material, but does not transport electrons well, so only electrons that are created by exciton dissociation close to the aluminium electrode will be extracted out of the device and contribute to the photocurrent. As the photons must travel through the MEH-PPV before being absorbed to contribute to the photocurrent, only a few of photons will reach this region and thus lower photocurrents will be extracted from the device. After these results, it can be discussed MEH-PPV acting as an optical filter by reducing the transmitted light for certain wavelengths.

This chapter will outline the results taken from the first samples made in this work. In Sections 5.3 differences in photovoltaic responses between single layer and double layer devices will help us to understand the operation of these devices. The aim of changing the polymer film thickness, from single layer devices to double layer devices, is to compare and analyse their different photovoltaic responses.

The optical filter effect in polymer solar cells will also be discussed. Finally blend devices using MEH-PPV and fullerenes will be presented.

## **5.2 Experimental**

Solutions of MEH-PPV for spin coating were prepared by dissolving the required masses of each material in chlorobenzene. The concentration of MEH-PPV used was always 10 mg/ml. For making organic photovoltaic devices the solutions were mixed by means of a sonication bath for 1 hour before being immediately spun cast onto ITO patterned substrates. The thicknesses of the spin coated layer were different for analysis, as confirmed by profilometry. An aluminium cathode was then evaporated on top of the polymer layer. J-V characteristics, photocurrent spectral responses and absorption spectra were carried out on these samples.

## 5.3 Results and discussion

### 5.3.1 Single layer devices

Purification of MEH-PPV solution was necessary when there were impurities or particles produced when spin casting films. The low-weight impurities were separated from the high-weight polymer by adding a concentrated solution of the polymer in chlorobenzene drop-wise to a solvent that the polymer was not soluble in such as methanol. The height-weight material precipitates out with the low weight material remained in solution. The mixture was passed through a filter. The collected precipitate was transferred into a beaker and dried overnight. Once dried, the polymer was weighed again and dissolved in chlorobenzene to get the desired concentration.

Following the device construction described in section 4.4.2, single layer devices films were spin-cast at 2000 rpm. A 85 nm MEH-PPV layer was spin-cast on top of ITO. An aluminium electrode around 50-75 nm was evaporated on top of this layer. The J-V characteristics of the single layer devices in the dark and under illumination for MEH-PPV polymer is shown in Figure 5.1.

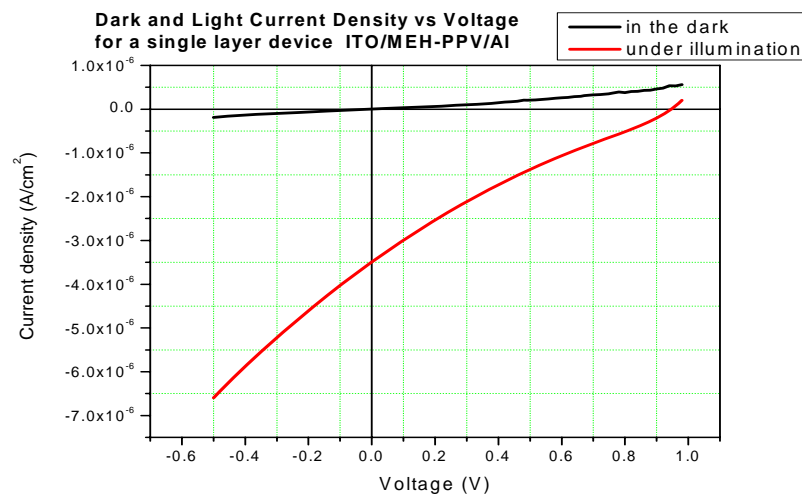


**Figure 5.1.** J-V characteristics of a MEH-PPV single layer device in the dark and under 80 mW/cm<sup>2</sup> white light illumination.

The graph in Figure 5.1 shows the J-V characteristics of the device. The open circuit voltage  $V_{oc}$  of MEH-PPV single layer device is 0.93 V and its short circuit current  $J_{sc}$  is  $-3.50 \times 10^{-3}$  mA/cm<sup>2</sup> at white light illumination of 80 mW/cm<sup>2</sup>. This

representation gives information about the fill factor of the solar cell and therefore gives some essential information about the efficiency of the cell.

The single layer devices show a very low,  $FF$ , which is below 0.25 (in this case it is 0.21). Fill factors below 0.25 typically indicate that there is a blocking contact at one of the electrodes inhibiting charge extraction out of the device. The low fill factors of single layer PPV devices are symptomatic of other processes reducing device efficiency. While low fill factors seem to be common for organic devices in general, the results of Tang [39] show that these shortcomings can be overcome. Tang's results suggest that low fill factors in organic devices are caused by the existence of continuous and separate pathways for the two types of charge carriers from anode to cathode [40], as well as by resistive losses due to low mobilities of the photogenerated charges. In terms of a circuit model of the cell, the low fill factors can be understood as arising from a low parallel shunt resistance and a large serial resistance.

It was mentioned earlier that, in principle, the open-circuit voltage is determined by the difference between the work functions of the two metal electrodes,  $\Delta\Phi = 1.2$  eV and 1.9 eV respectively [41], but an anomaly is observed for aluminium. The difference between the work functions of aluminium and ITO is 0.5 eV, whereas the typical open-circuit voltage is 0.8 V, with voltages up to 1.3 V reported [42]. The open circuit voltage can also be calculated from the difference between the HOMO of the donor and the LUMO of the acceptor when double layer devices or blend devices are made using donor materials such as P3HT and acceptor materials such as fullerenes  $C_{60}$  or PCBM. This will be explained again in more detail in Section 6.

The spectral photocurrent response and the absorption spectra of MEH-PPV devices are shown in Figure 5.2 and Figure 5.3.

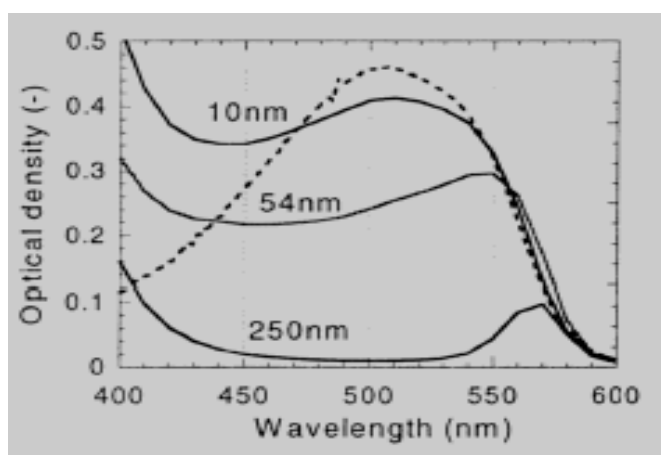


**Figure 5.2.** Spectral photocurrent response (solid line) of ITO/MEH-PPV/Al device for three different polymer film thicknesses. Also shown is the absorption spectra of a 38 nm MEH-PPV film (dotted line). Reproduced from [43].

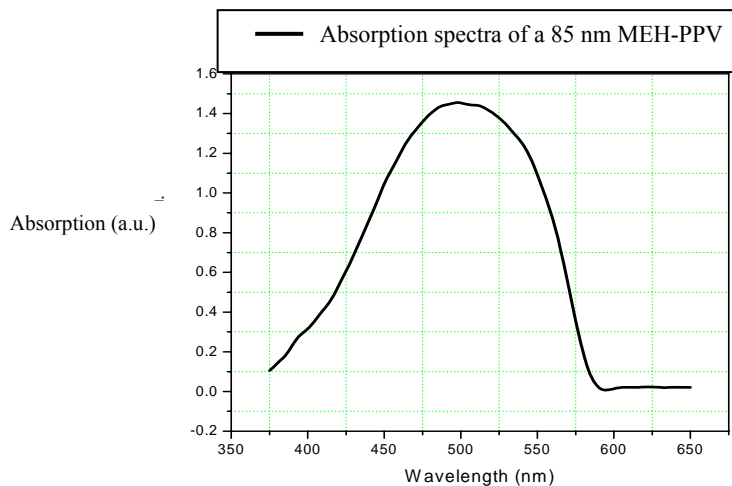


**Figure 5.3.** UV-vis absorption spectra response of a MEH-PPV single layer device in this work. The solid line shows the absorption after spin casting a layer of 85 nm onto ITO substrate.

The MEH-PPV has an absorption peak at 500 nm and an onset at 590 nm. No appreciable change in the absorption spectra of MEH-PPV thin films from others authors [43] was observed.

### 5.3.2 Double layer devices

Again solutions of MEH-PPV in chlorobenzene at the same concentration were used in double layer devices. Thin layers of 30 nm MEH-PPV were spin-cast as a buffer layer at 3500 rpm on top of ITO. This first layer was then dried at 100 °C for 3 hours. After another 85 nm film of MEH-PPV was spin-cast at 2000 rpm on top of the first buffer layer. The device structure of ITO / MEH-PPV / MEH-PPV / Al is shown below in Figure 5.4. No state of interface between layers is expected. In this section what it is important is the total thickness of the polymer layer and also its influence on the final photovoltaic response.

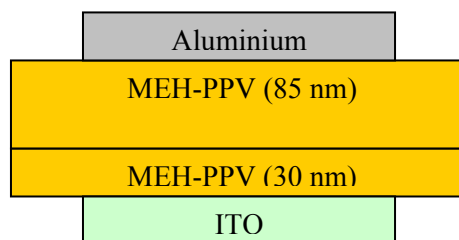


**Figure 5.4.** Device structure of double layer MEH-PPV device.

Current-voltage characteristics of this MEH-PPV double layer device are shown in Figure 5.5.

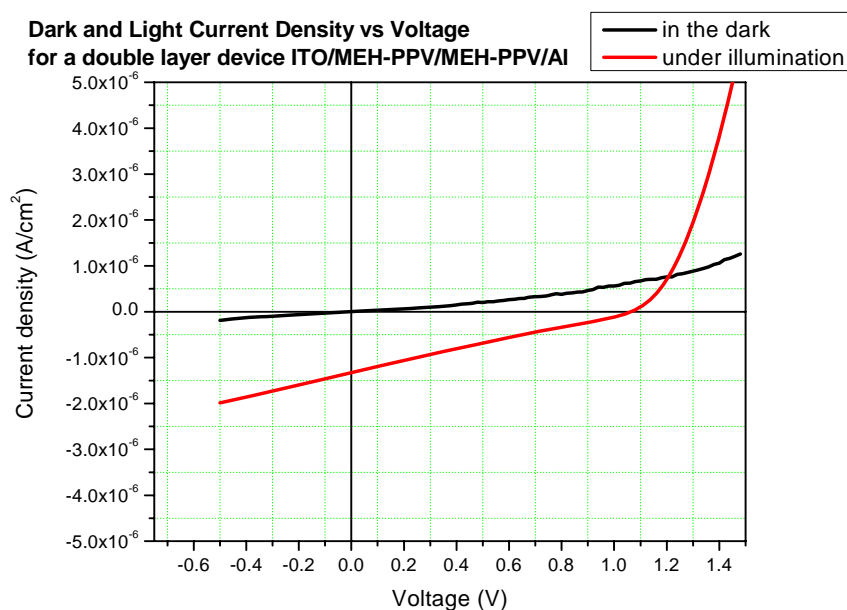


**Figure 5.5.** J-V characteristics of a MEH-PPV double layer device in the dark and using 80 mW/cm<sup>2</sup> white light illumination.

As it can be seen in Table 1, the open circuit voltage  $V_{OC}$  of the MEH-PPV double layer device is 1.06 V and its short circuit current  $J_{SC}$  is  $-1.30 \times 10^{-3}$  mA/cm<sup>2</sup> using 80 mW/cm<sup>2</sup> white light illumination. The double layer device shows a fill factor FF of 0.24.

Film thickness (nm)	Jsc ( $\times 10^{-3}$ mA/cm <sup>2</sup> )	Voc (V)	(JV)max ( $\times 10^{-4}$ mA.V/cm <sup>2</sup> )	FF (%)	$\eta_e$ ( $\times 10^{-3}$ %)
85	-3.50	0.93	-6.67	20.49	0.83
115	-1.30	1.06	-3.36	24.38	0.42

**Table 1.** Short circuit density ( $J_{SC}$ ), open circuit voltage ( $V_{OC}$ ), maximum power  $(JV)_{MAX}$ , fill factor (FF) and power efficiency  $\eta_e$  of ITO / MEH-PPV / Al solar cells as a function of the thickness of the polymer MEH-PPV layer (single and double layer devices respectively).

The spectral response SR of the ITO substrate and double MEH-PPV layer on top of this substrate is shown in Figure 5.6.

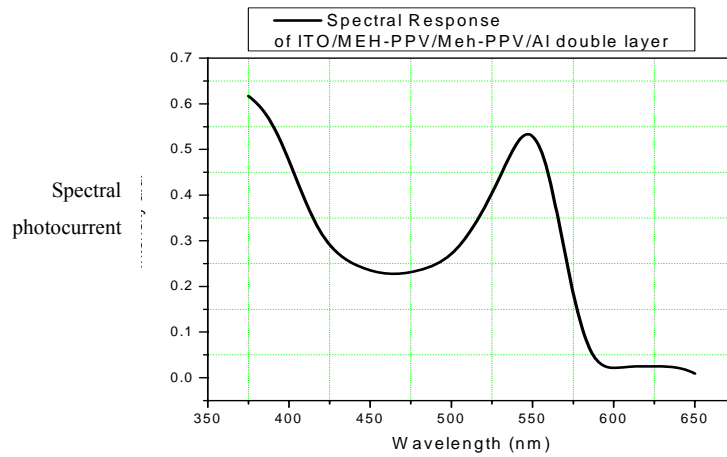


**Figure 5.6.** Spectral photocurrent response of a MEH-PPV double layer device.

Due to short exciton diffusion lengths most organic cells have a bulk thickness that is considerably larger than the active layer near the polymer/aluminium interface (to avoid short circuits, see Figure 5.8). Thus these spectral responses SR show a strong filter effect resulting in SR maxima at wavelengths where the optical density (OD) is low and SR minima where the OD is too high to allow many photons to reach the active region. Optical density is often defined without regard to the length of the sample.

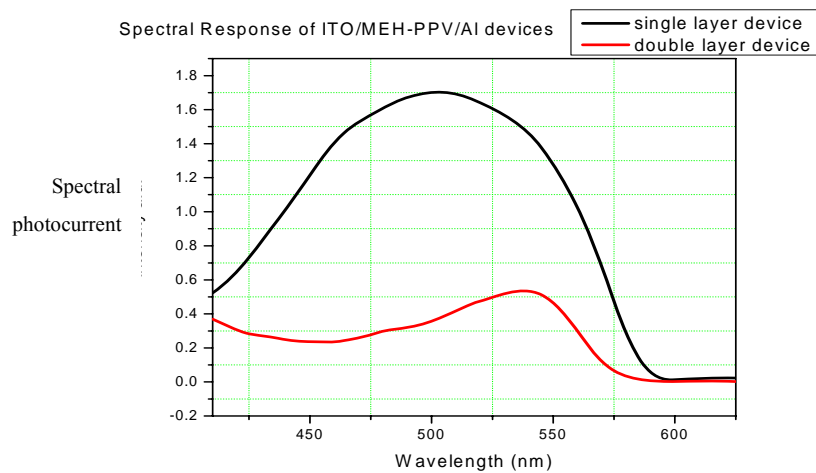


**Figure 5.7.** Spectral photocurrent response of a MEH-PPV single and double layer devices.

Photocurrent spectra responses of single and double layer devices are shown in Figure 5.7 . Photocurrent in double layer device is lost, only thin layer devices rise to photocurrent. Therefore, an important photocurrent reduction can be observed.

It is important that all the results are reproducible. This was achieved using MEH-PPV as a polymer layer and a variation of film thickness.

### 5.3.3 Filter effect

Considering photovoltaic devices such as a single and double layer device of ITO / MEH-PPV / Al, the results show that for these devices, the cell's short circuit current  $J_{SC}$  as well as its power efficiency  $\eta_e$  increase as the thickness of the polymer layer decreases. This characteristic is shown in Table 2.

Film thickness (nm)	$J_{sc}$ ( $\times 10^{-3}$ mA/cm <sup>2</sup> )	Voc (V)	(JV)max (mA.V/cm <sup>2</sup> )	FF (%)	$\eta_e$ ( $\times 10^{-3}$ %)
85	-3.50	0.93	$-6.67 \times 10^{-4}$	20.49	0.83
115	-1.30	1.06	$-3.36 \times 10^{-4}$	24.38	0.42
140	-1.14	1.12	$-3.12 \times 10^{-4}$	24.43	0.39

**Table 2.** Short circuit density ( $J_{SC}$ ), open circuit voltage ( $V_{OC}$ ), maximum power ( $(JV)_{MAX}$ ), fill factor (FF) and power efficiency  $\eta_e$  of ITO / MEH-PPV / Al solar cells as a function of the thickness of the polymer MEH-PPV layer.

To explain the filter effect it was considered that the absorption in organic semiconducting polymers is strongly dependent on the wavelength. The light at weakly absorbed wavelengths can propagate into the whole film and absorbed into the bulk of the material, but the light at strongly absorbed wavelengths will be absorbed in the surface layer and does not penetrate into the bulk. The film in this case acts as an optical filter.



The photocurrent in thick single layer devices is lost, since only thin active layer devices give rise to photocurrent. This phenomenon is actually called Filter Effect. Only light absorbed in the active layer contributes to the photocurrent, in other words, the photovoltaic response increases using thinner layer devices. The layer that absorbs light before reaching the active region (active layer) is called the optical filter.

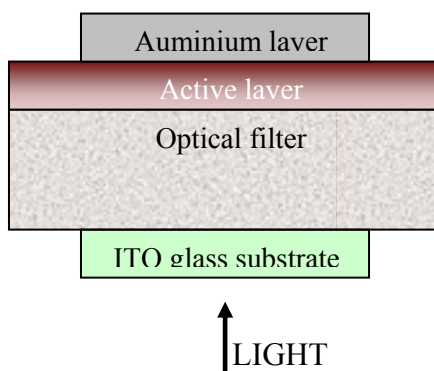


**Figure 5.8.** Schematic picture explaining the filter effect.

As it can be seen in Table 2, the power efficiency decays as a function of the MEH-PPV layer thicknesses. Figure 5.9 shows this decay.

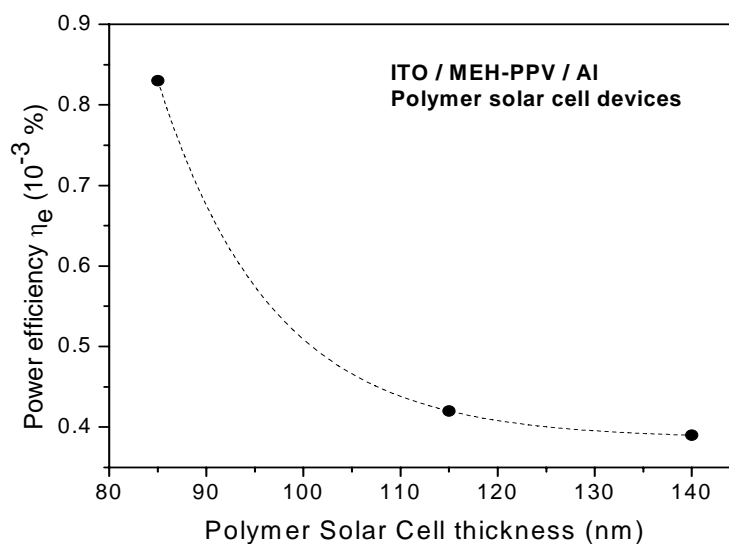


**Figure 5.9.** Power efficiency of ITO / MEH-PPV /Al as a function of the MEH-PPV layer's thicknesses.

### 5.3.4 MEH-PPV and fullerene devices

A different approach is to create a bulk-heterojunction between polymers, such as MEH-PPV, and fullerenes, such as  $C_{60}$  or PCBM, by blending the two materials in solution and spin-coating devices from this blend.

The polymer MEH-PPV and the fullerene  $C_{60}$  were firstly blended. Secondly, devices using the fullerene derivative PCBM were made, the devices were ITO / MEH-PPV:PCBM / Al and the polymer MEH-PPV and PCBM blended at weight 1:0.2 ratio. All the blends were spin casting at different spin speeds in order to get the same thickness  $\sim 70$  nm.

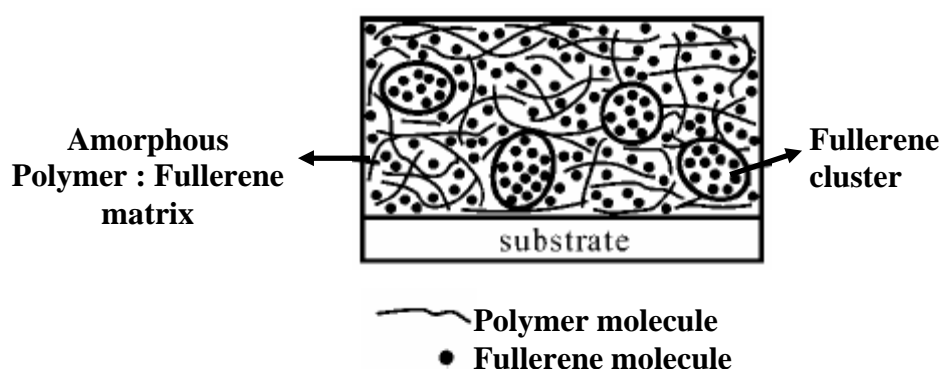


**Figure 5.10.** Illustration of a polymer/fullerene network in a composite. Reproduced from [44].

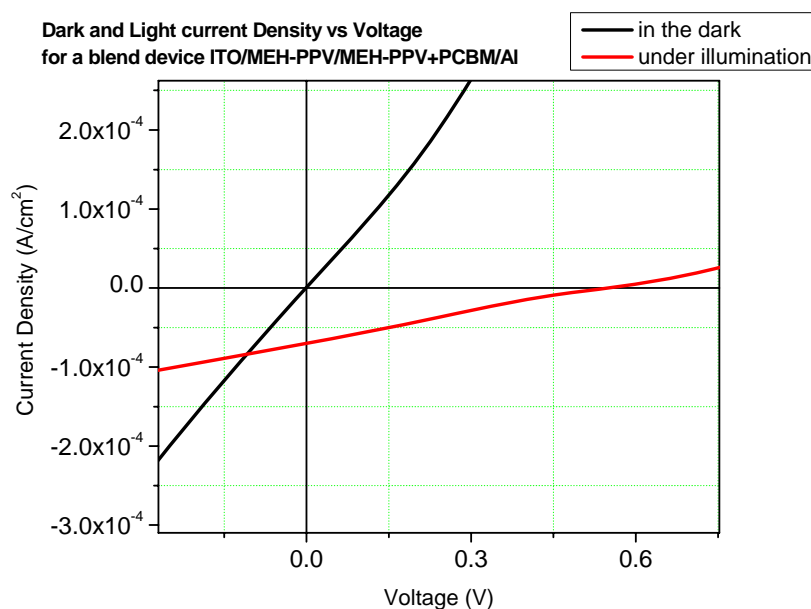


**Figure 5.11.** J-V characteristics of ITO / MEH-PPV:PCBM(20%w.) (70nm) / Al layer device in the dark and using  $80 \text{ mW/cm}^2$  white light illumination.

As it can be seen in Figure 5.11, the open circuit voltage  $V_{oc}$  of MEH-PPV:PCBM (1:1 ratio) device is 0.51 V and its short circuit current  $J_{sc}$  is  $-7.05 \times 10^{-2}$  mA/cm<sup>2</sup> using 80 mW/cm<sup>2</sup> white light illumination. I-V characteristics of ITO / MEH-PPV:PCBM (1:1 ratio, 85nm) / Al are not shown in this work.

Comparison of the photovoltaic response parameters of single layer MEH-PPV device and blend MEH-PPV:PCBM device is shown in table 3.

Sample Device	Jsc (mA/cm <sup>2</sup> )	Voc (V)	(JV)max (mA.V/cm <sup>2</sup> )	FF (%)	$\eta_e$ (%)
MEH-PPV (85nm)	$-3.50 \times 10^{-3}$	0.93	$-6.67 \times 10^{-4}$	20.49	0.83 $\times 10^{-3}$
MEH-PPV:PCBM (70nm)	$-7.05 \times 10^{-2}$	0.55	-0.010	23.20	0.01

**Table 3.** Short circuit density ( $J_{sc}$ ), open circuit voltage ( $V_{oc}$ ), maximum power ( $(JV)_{max}$ ), fill factor (FF) and power efficiency  $\eta_e$  of different polymer composites solar cells.

Another polymer commonly used in polymer based photovoltaic devices is Poly(3-hexylthiophene) P3HT due to its donor electron capacity. The MEH-PPV and the P3HT absorption spectra profile were compared. Figure 5.12 shows the absorption spectra of MEH-PPV and P3HT. Polythiophenes are considered to possess an enhanced photostability compared to PPVs, while their absorption spectra show a better overlap with the solar emission spectra (see Figure 4.4 in Section 4.4.1). Works and results of P3HT devices are included in the next Chapter 6.

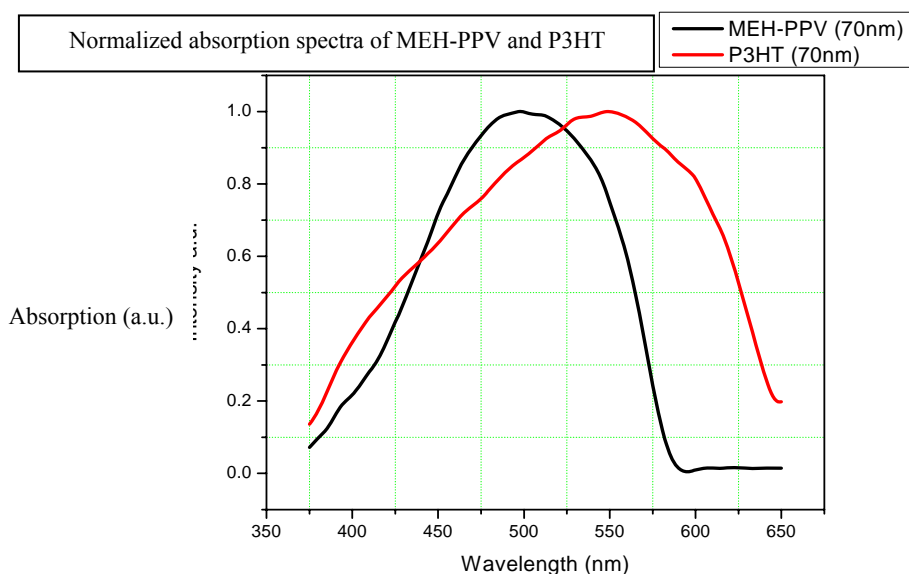


**Figure 5.12.** UV-vis absorption spectra response of MEH-PPV and P3HT devices.

MEH-PPV has an absorption peak at 500 nm and an onset at 590 nm and the P3HT has an absorption peak at 550-560 nm, a shoulder at 600 nm and an onset at 650 nm showing better red absorption. Peaks were normalised to the same height.

## **5.5 Conclusions**

In order to characterise the photovoltaic response of a conjugated polymer, MEH-PPV single layer (SL) devices were prepared and characterised. The filter effect was discussed with regard to a conjugated polymer such as MEH-PPV. It was found that only thin layers contributed to the photocurrent. This resulted in better power efficiencies for thinner polymer solar cells.

Fullerenes such as PCBM were blended with MEH-PPV in order to study their optical density and their efficiencies. Variety of composites such as MEH-PPV:PCBM were tested.

Using composite blends with PCBM, the fill factor increases and the efficiencies were improved. So far, 0.01 % for MEH-PPV:PCBM blend was the highest efficiency found.

# **CHAPTER 6 – HIGH EFFICIENCY P3HT/PCBM PHOTOVOLTAIC DEVICES**

## **6.1 Introduction**

In Chapter 5 the limitations of using MEH-PPV photovoltaic devices was analysed. This chapter will outline the results of using Poly(3-hexylthiophene) (P3HT) in polymer based photovoltaic devices due to its excellent solubility in common organic solvents, fine stability and important contribution to increase the photovoltaic response. Photovoltaic devices using polythiophenes and fullerene blends were first reported by Roman et al [45]. MEH-PPV and P3HT were compared in Chapter 5 to see differences between I-V's and spectra response of each polymer.

In this chapter a thorough investigation into the changes in photovoltaic performance of devices based on blends of P3HT and PCBM that occur after annealing are presented. Important processing parameters, such as the blend ratio and the solvent from which it is spin cast are optimized. The effect of the two key annealing parameters, time and temperature, on the optical properties and surface morphology of the blends is then assessed. Current-voltage measurements, absorption spectroscopy as well as photocurrent spectroscopy analysis and differential calorimetric measurements were carried out to characterise all the photovoltaic devices made.

This intense study to find the optimum composition and processing conditions of P3HT:PCBM blends to maximize photovoltaic performance will be carried out to analyse the mechanisms by which phase separation occurs in this blend on annealing and the nature of the phase separated regions.

## **6.2 Experimental**

Solutions of P3HT and PCBM for spin coating were prepared by dissolving the required masses of each material in chloroform or chlorobenzene. The concentration of P3HT used was always 10 mg/ml. For making Schottky devices the solutions were mixed by means of a sonication bath for 1 hour before being immediately spun cast onto PEDOT coated ITO substrates. The thickness of the spin coated blend layer was

approximately 70 nm, as confirmed by profilometry. A 30 nm PEDOT:PSS layer was previously coated onto the ITO substrates and dried by baking on a hot plate at 80 °C for 10 minutes. After an aluminium cathode was evaporated on top of the blend layer the I-V characteristics and spectral responses of the device were obtained before the devices were annealed at 140 °C for 4 minutes and re-tested.

## 6.3 Results and discussion

### 6.3.1 Inclusion of PEDOT:PSS

PEDOT:PSS films smoothed the rougher ITO layer and provided better wetting for the next layers. It is also improved the interaction between the active layer (50-50 wt.-% P3HT:PCBM composite) and the bottom electrode (ITO) as can be observed by the increasing the open circuit voltage  $V_{oc}$ , by improving the hole injection into the electrode. It also improved the device lifetime by preventing indium migration into the active layer of the device [47]. The photovoltaic mechanism of ITO / PEDOT:PSS / P3HT:PCBM device, and how it works in terms of organic solar cells, is explained as follows:

Photons excite electrons from HOMO into LUMO of the P3HT, which are transferred to LUMO of the PCBM, from which they can be collected by a negative Al electrode with work function  $\Phi \sim 4.2 \text{ eV}$ . Similarly holes are collected via the PEDOT:PSS which has work function  $\Phi \sim 5.0 \text{ eV}$ , by the positive ITO electrode with a work function  $\Phi \sim 4.8 \text{ eV}$ .

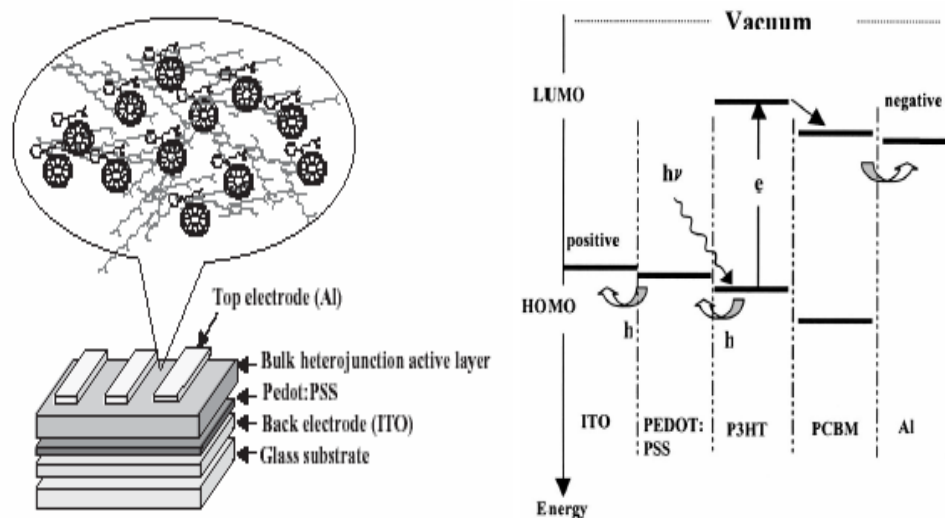


**Figure 6.1.** Device structure and operation principle on ITO / PEDOT:PSS / P3HT:PCBM / Al devices.

As discussed previously, spin coating a PEDOT:PSS layer onto ITO will improve the hole transport to the ITO electrode and will increase the open circuit voltage. Current-Voltage characteristics of ITO / P3HT:PCBM / Al and ITO / PEDOT:PSS / P3HT:PCBM / Al shown in Figure 6.2 confirm this statement.

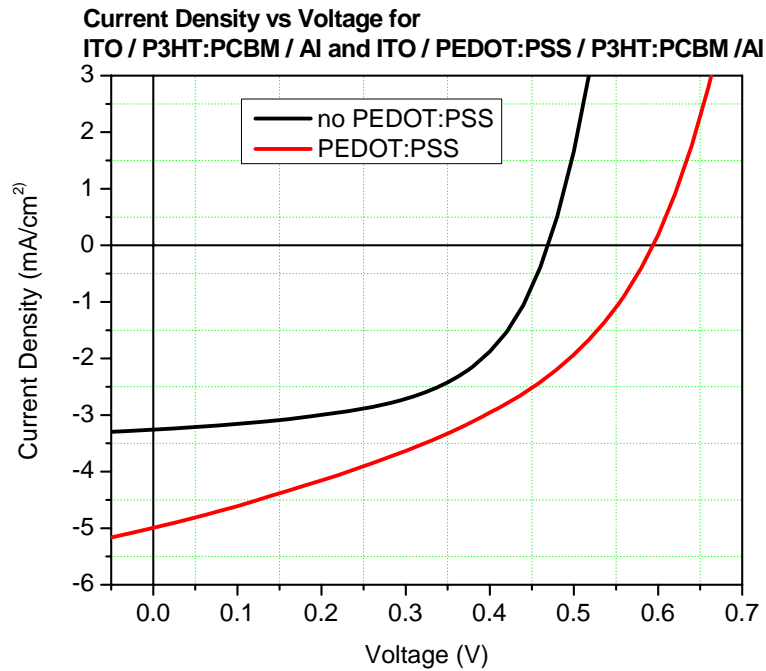


**Figure 6.2.** J-V characteristics of a P3HT:PCBM (70 nm) layer device with and without PEDOT:PSS (30nm) layer using 80 mW/cm<sup>2</sup> white light illumination.

The open circuit voltages  $V_{oc}$  of P3HT:PCBM (70 nm) devices were 0.47V and 0.59V and their short circuit currents  $J_{sc}$  were -3.25 mA/cm<sup>2</sup> and -4.98 mA/cm<sup>2</sup> for devices with and without the PEDOT:PSS layer spun on ITO respectively.

Sample	$J_{sc}$ (mA/cm <sup>2</sup> )	$V_{oc}$ (V)	(JV) <sub>max</sub> (mA.V/cm <sup>2</sup> )	FF (%)	$\eta_e$ (%)
Without PEDOT:PSS	-3.25	0.47	-0.84	54.90	1.04
With PEDOT:PSS	-4.98	0.59	-1.18	40.10	1.47

**Table 4.** Short circuit density ( $J_{sc}$ ), open circuit voltage ( $V_{oc}$ ), maximum power ( $JV$ )<sub>MAX</sub>, fill factor (FF) and power efficiency  $\eta_e$  of ITO / P3HT:PCBM / Al and ITO / PEDOT:PSS / P3HT:PCBM / Al devices.

As it can be seen in Table 4, there was an increase in the open circuit voltage  $V_{oc}$  and also in the short current density  $J_{SC}$  resulting in higher power efficiency  $\eta_e$  when the PEDOT:PSS layer was added.

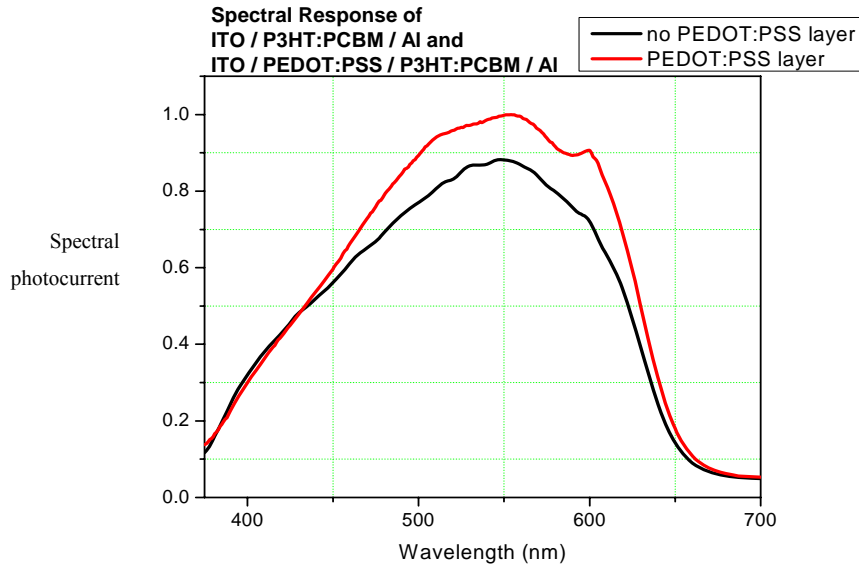


**Figure 6.3.** Representative spectral photocurrent response of a P3HT:PCBM layer device with and without PEDOT:PSS.

The spectral photocurrent response on films for samples with and without PEDOT:PSS are shown above in Figure 6.3. The device with no PEDOT:PSS layer shows a strong peak at 550 nm and a smooth shoulder at 600 nm. Once PEDOT:PSS is spun in between the ITO and the active layer P3HT:PCBM, the peak at 550 nm is stronger and the shoulder at 600 nm is not as smooth or flat as in the device with no PEDOT:PSS.

### 6.3.2 Annealing Process

The process of thermal annealing has been demonstrated to considerably increase the efficiency of P3HT solar cells [47]. The effect of device annealing and its consequences were studied on organic ITO / PEDOT:PSS / P3HT:PCBM / Al photovoltaic devices.

To better understand the importance of  $T_g$  (glass transition temperature),  $T_m$  (melting temperature) and  $T_c$  (crystallisation temperature) on the interdiffusion process, heat cycles at temperatures above  $T_g$  ( $46^\circ\text{C}$ ), and below  $T_m$  ( $200^\circ\text{C}$ ), around  $T_c$  ( $120^\circ\text{C}$ ) were chosen. The initial temperature was  $140^\circ\text{C}$  and the duration was for 4 minutes



[46]. This resulted in an optimum photovoltaic response after annealing, see Figure 6.4.

Calorimetric analysis of P3HT and also of P3HT:PCBM are discussed in the next Section 6.3.7 and from this, the optimum annealing temperature for improved photovoltaic performance of the devices was determined.

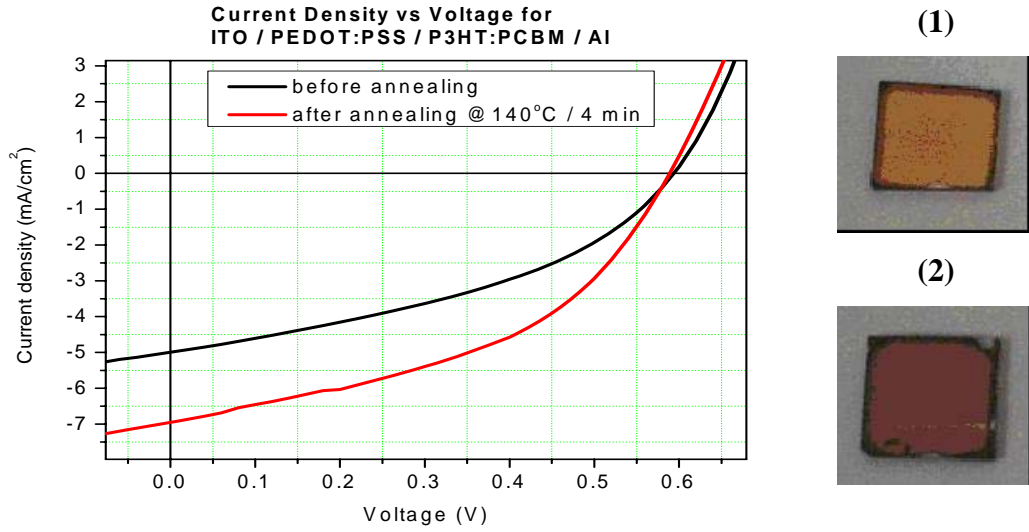


**Figure 6.4.** J-V characteristics of an ITO/PEDOT:PSS (30nm)/P3HT:PCBM (70 nm)/Al photovoltaic device before and after annealing treatment at 140°C for 4 minutes using 80 mW/cm<sup>2</sup> white light illumination. Pictures (1) and (2) show the colour of the composite film before and after annealing respectively. P3HT film colour predominates after annealing.

All the devices parameters increase after thermal annealing treatment except  $V_{oc}$ : the open circuit voltage  $V_{oc}$  of the ITO/PEDOT:PSS/P3HT:PCBM/Al device before annealing is 0.59 V and its short circuit current is  $J_{SC}$  is -4.98 mA/cm<sup>2</sup> at a monochromatic illumination of 80 mW/cm<sup>2</sup>; after annealing the sample at 140°C for 4 minutes on a hot plate the open circuit voltage  $V_{oc}$  was 0.58 V and its short circuit current  $J_{SC}$  was -7.00 mA/cm<sup>2</sup>. An important increase in the short circuit current was achieved. Moreover there is also an increase in the total power conversion efficiency.

Treatment	Jsc (mA/cm <sup>2</sup> )	Voc (V)	(JV)max (mA.V/cm <sup>2</sup> )	FF (%)	$\eta_e$ (%)
Before annealing	-4.98	0.59	-1.18	40.16	1.47
After annealing	-7.00	0.58	-1.82	45.02	<b>2.28</b>

**Table 5.** Short circuit density ( $J_{SC}$ ), open circuit voltage ( $V_{oc}$ ), maximum power  $(JV)_{MAX}$ , fill factor (FF) and power efficiency  $\eta_e$  of ITO / PEDOT:PSS / P3HT:PCBM / Al devices before and after annealing at 140°C for 4 minutes.

The improvement obtained from annealing was explained in terms of an increase in the hole mobility of the polymer resulting from enhanced crystallisation from heating above the glass transition temperature [46]. The external electric field was expected to inject charges into the polymer which would help orient the polymer chains in the direction of the applied field, resulting in enhanced conductivity [46].

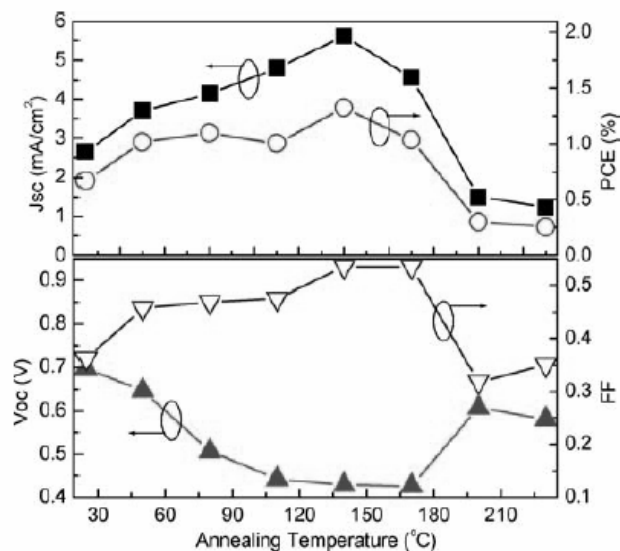


**Figure 6.5.** Short circuit current, efficiency, open circuit voltage and fill factor for P3HT:PCBM (1:1 by weight) blend film devices as a function of annealing temperature. Reproduced from [47].

In Figure 6.5 above, it is shown that the highest power conversion efficiency (in this case 1.4%) was achieved by annealing devices at 140°C for 4 minutes [46]. For the rest of this work this annealing temperature was used for all devices studied.

### 6.3.3 Variation of Fullerene PCBM

The photovoltaic performance of ITO/PEDOT:PSS/P3HT:PCBM/Al devices were studied for different PCBM weight ratios. These devices were constructed with varying PCBM contents. Current-voltage analysis for different weight ratios, 1:0, 1:0.25, 1:0.50, 1:0.75 and 1:1, before and after annealing at 140 °C for 4 minutes, are shown in Figure 6.6. Note that current-voltage analysis for weight ratios beyond 1:1 did not contributed to better results. These results are not shown in this work.

Comparison of the device performance parameters obtained from devices based on blends of different ratios of P3HT and PCBM, before and after annealing will be explained in detail.

Spectral responses from photovoltaic devices based on P3HT:PCBM will be also analysed.

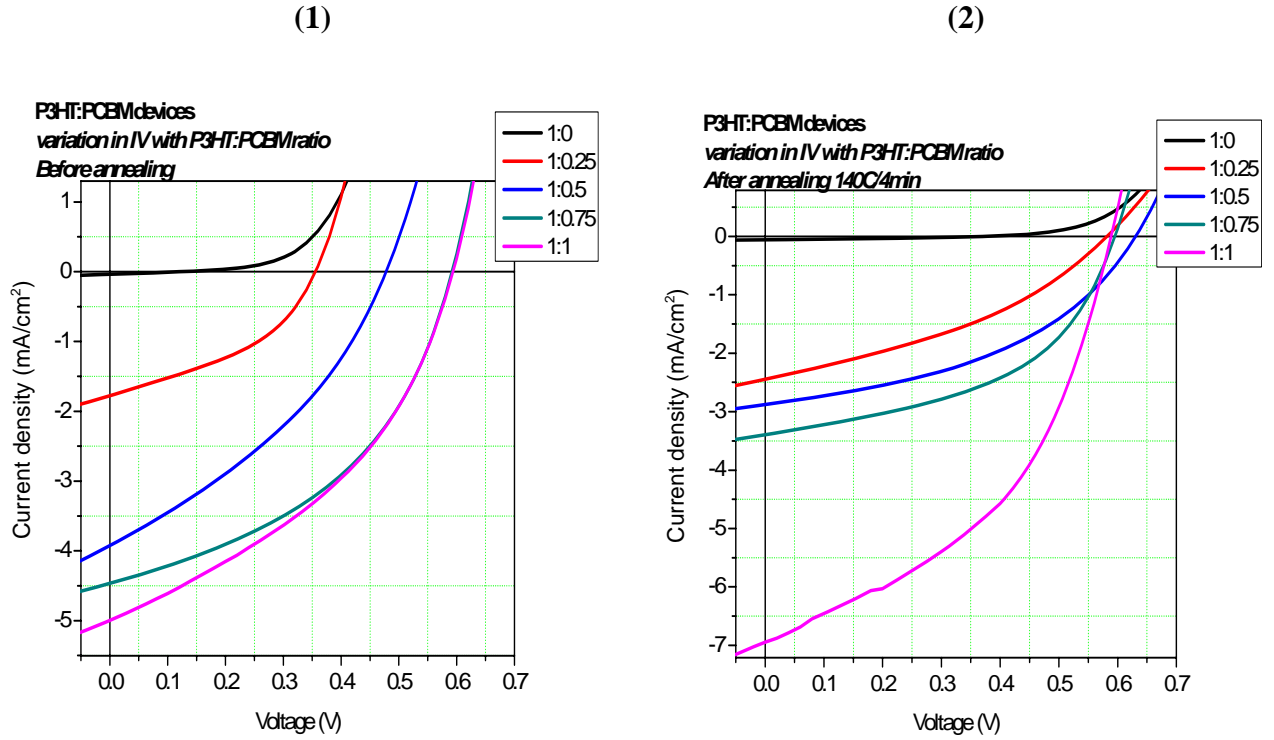
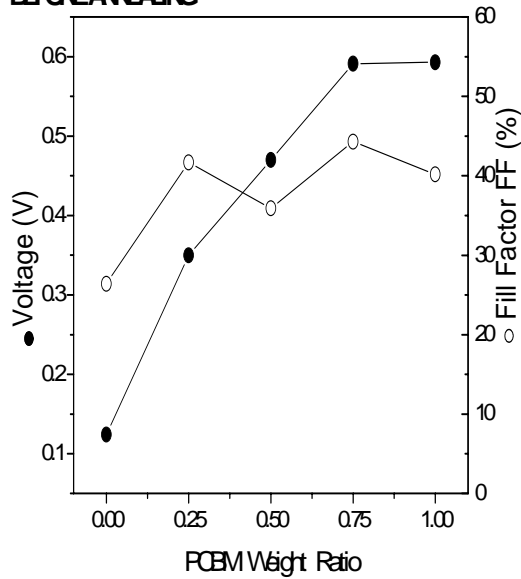


**Figure 6.6.** J-V characteristics of an ITO/PEDOT:PSS(30nm)/P3HT:PCBM(70nm)/Al photovoltaic device before (1) and after annealing at 140°C for 4 minutes (2) using 80 mW/cm<sup>2</sup> white light illumination as a function of PCBM weight ratio.

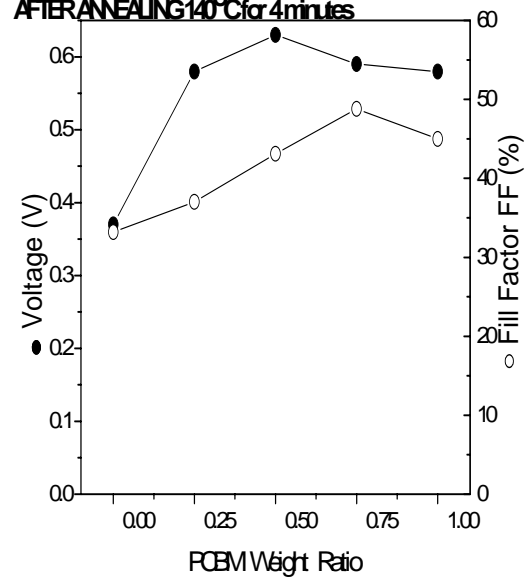
As it can be seen in Figure 6.6 there is a trend confirming that the addition of PCBM to P3HT significantly improves the efficiency of the device. For un-annealed devices short circuit current  $J_{SC}$  increases by almost two orders of magnitude. There is also a gradual increase in the open circuit voltage  $V_{oc}$  with increasing PCBM content from less than 0.2 V for pure P3HT to approximately 0.6 V for 1:1 blend ratio.

After annealing there is an improvement in the performance of all devices regardless of the PCBM content of the blend. Even for a pure P3HT device  $V_{oc}$  doubles and  $J_{SC}$  increases by almost 50%. A perhaps surprising observation is how the  $V_{oc}$  for blends containing PCBM does not appear to vary a great deal with PCBM content after they are annealed. However there is a trend toward higher currents and higher efficiencies as the PCBM content is increased up to a 1:1 ratio, suggesting this ratio gives the best photovoltaic performing devices.

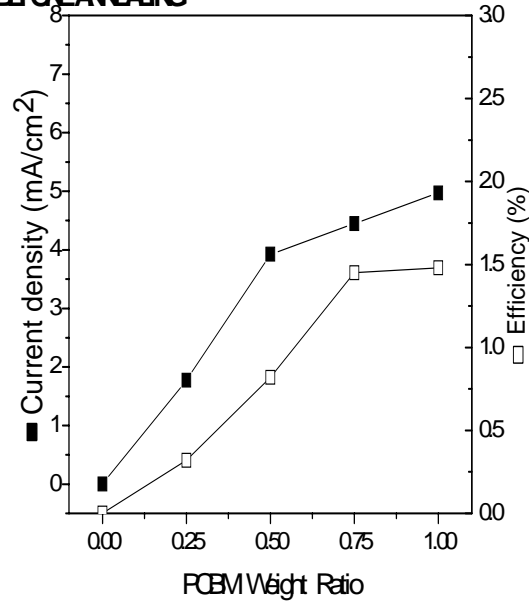
**Voltage and Fill Factor for ITO/PEDOT:PSS/P3HT:PCBM/AI BEFORE ANNEALING**



**Voltage and Fill Factor for ITO/PEDOT:PSS/P3HT:PCBM/AI AFTER ANNEALING 140°C for 4 minutes**



**Current Density and Efficiency for ITO/PEDOT:PSS/P3HT:PCBM/AI BEFORE ANNEALING**



**Current density and Efficiency for ITO/PEDOT:PSS/P3HT:PCBM/AI AFTER ANNEALING 140°C for 4 minutes**

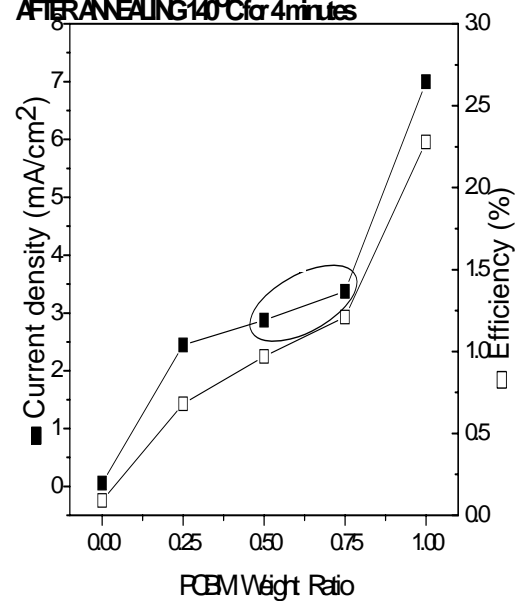


**Figure 6.7.** Short circuit current, efficiency, open circuit voltage and fill factor for PEDOT:PSS/P3HT:PCBM blend film devices as a function of PCBM Weight Ratio.

Figure 6.7 shows the photovoltaic performance parameters as a function of PCBM weight ratio before and after annealing. Both current density and power efficiency increased as the PCBM ratio in P3HT:PCBM composite is increased.

Higher values for the current density are expected for the annealed devices, but for the P3HT:PCBM (1:0.50) and P3HT:PCBM (1:0.75) samples the current density

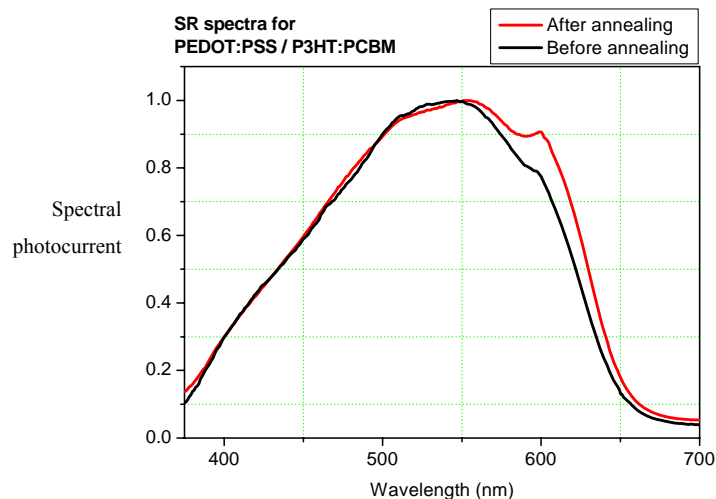
decreased to 2.87 mA/cm<sup>2</sup> and 3.37 mA/cm<sup>2</sup> respectively (marked in circle in the graph). However their fill factor values and their power efficiencies were higher after annealing (see Table 6) and thus better photovoltaic performance was achieved. The open circuit voltages generally increase after annealing, but they stabilise around 0.6V after PCBM weight ratio is increased. Fill factors became constant around 45% after annealing. The best performance was observed for the P3HT:PCBM (1:1 weight ratio) which is in accordance with previous reports [47, 48].

Table 6 shows all the photovoltaic parameters for P3HT:PCBM with different PCBM weight ratios. A maximum efficiency without any treatment was found at around 1.47 % and for the annealed samples, 2.28 % was the maximum efficiency achieved.

Treatment	Weight ratio	Jsc (mA/cm <sup>2</sup> )	Voc (V)	(JV)max (mA.V/cm <sup>2</sup> )	FF (%)	$\eta_e$ (%)
Before annealing	1:0	-0.04	0.12	-1.23 x 10 <sup>-3</sup>	26.2	1.53e-3
	1:0.25	-1.78	0.35	-0.26	41.7	0.32
	1:0.50	-3.92	0.47	-0.66	35.9	0.82
	1:0.75	-4.45	0.59	-1.16	44.3	1.45
	1:1	-4.98	0.59	-1.18	40.1	1.47
After annealing	1:0	-0.05	0.37	-7.23 x 10 <sup>-3</sup>	33.2	9.12e-2
	1:0.25	-2.44	0.58	-0.52	37.0	0.68
	1:0.50	-2.87	0.63	-0.78	43.1	0.97
	1:0.75	-3.37	0.59	-1.83	48.8	1.21
	1:1	-7.00	0.58	-1.82	45.0	<b>2.28</b>

**Table 6.** Short circuit density ( $J_{SC}$ ), open circuit voltage ( $V_{OC}$ ), maximum power ( $(JV)_{MAX}$ ), fill factor (FF) and power efficiency  $\eta_e$  of ITO / PEDOT:PSS / P3HT:PCBM / Al devices before and after annealing at 140°C for 4 minutes as function of P3HT:PCBM weight ratio.

The effect of thermal annealing on PEDOT:PSS/P3HT:PCBM devices have been also observed in the absorption spectra and the spectral photocurrent response. Figure 6.8 shows the spectral photocurrent response of P3HT:PCBM composites with a PEDOT:PSS layer film before and after annealing.



**Figure 6.8.** Spectral photocurrent response of PEDOT:PSS/P3HT:PCBM before and after annealing at 140°C for 4 minutes.

A small increase in the photocurrent intensity can be observed at 600 nm, which has been associated with improved inter-chain order, while almost no change was observed in the peak at 550 nm.

### 6.3.4 Solvent comparison

As reported in Section 3.2.3, polythiophenes P3OT and P3HT are highly soluble in organic solvents such as chlorobenzene or chloroform. Therefore the next experiment was to compare the photovoltaic response of ITO/PEDOT:PSS/P3HT:PCBM/Al blended P3HT:PCBM in chloroform (the same solvent used in previous Sections) and also blended in another organic solvent, chlorobenzene. Blend solutions with P3HT:PCBM (1:1 weight ratio) were prepared in chloroform and chlorobenzene at a solution concentration of 10 mg/ml. These solutions were stirred for more than 24 hours at room temperature to ensure that polymer and fullerene blends were well mixed in solvents.

Current-voltage characteristics of these last composites were studied and also different time annealing times were used to see if there was any difference in the photovoltaic performances. Annealing times of 140 °C for 4 minutes (maximum power efficiency expected) and for 30 minutes were analysed. Dark and light current densities versus voltage graphs are shown in Figure 6.9.

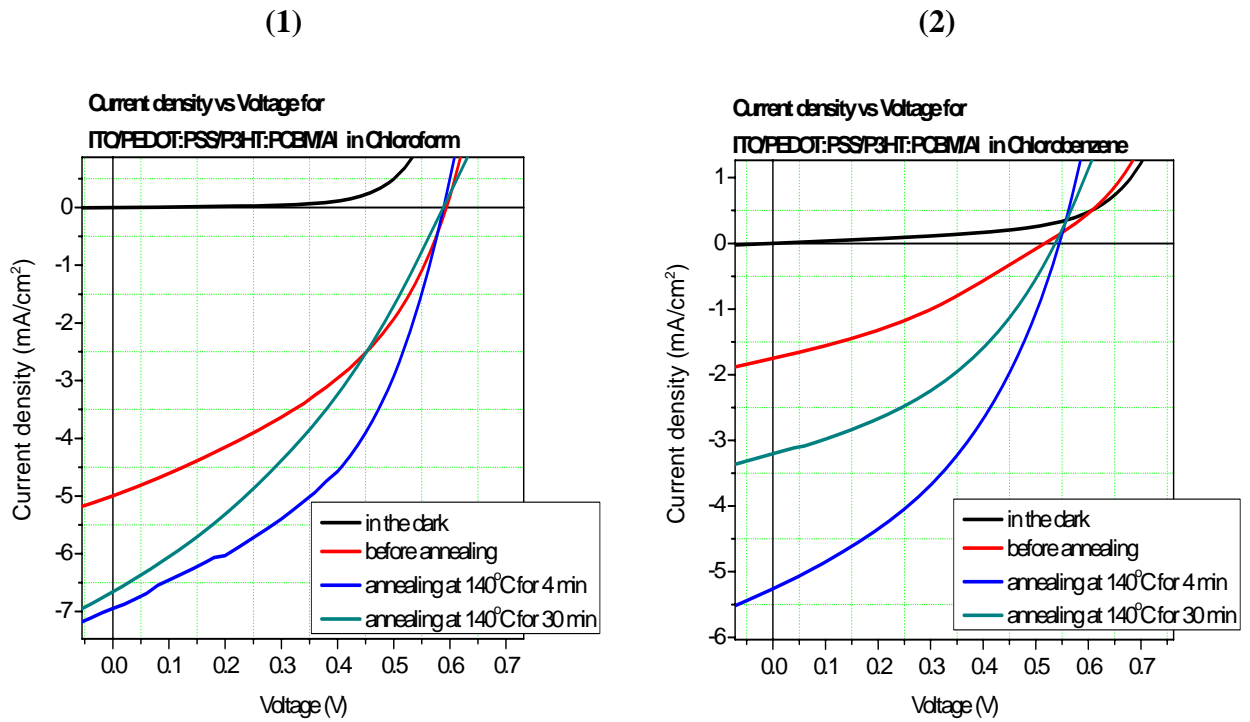


**Figure 6.9.** J-V characteristics of a ITO / PEDOT:PSS(30nm) / P3HT:PCBM(70 nm) / Al photovoltaic device before annealing and at different annealing times under 80 mW/cm<sup>2</sup> white light illumination in Chloroform (1) and Chlorobenzene (2).

All photovoltaic performance parameters of two different solar cells prepared in two different solvents, chloroform and chlorobenzene, taken after annealing at 140 °C for 4 minutes, are shown in following Table 7.

Solvent	J <sub>sc</sub> (mA/cm <sup>2</sup> )	V <sub>oc</sub> (V)	(JV) <sub>max</sub> (mA.V/cm <sup>2</sup> )	FF (%)	$\eta_e$ (%)
Chloroform	-7.00	0.58	-1.82	45.02	<b>2.28</b>
Chlorobenzene	-5.26	0.54	-1.13	39.80	1.41

**Table 7.** Short circuit density (J<sub>SC</sub>), open circuit voltage (V<sub>OC</sub>), maximum power (JV)<sub>MAX</sub>, fill factor (FF) and power efficiency  $\eta_e$  of ITO / PEDOT:PSS / P3HT:PCBM / Al devices after annealing at 140°C for 4 minutes as a function of solvent used.

Results before annealing and also after annealing, at 140°C for 30 minutes, are not shown in this work because they do not contribute to get optimum efficiencies.

Finally, as it can be seen in Table 7, the maximum power conversion efficiency observed in this work, 2.28%, using chloroform as solvent, is higher than previously reported in reference [46], 1.4%.

### 6.3.5 Effects of postproduction treatment

Postproduction treatment, such as applying an external electric field on plastic solar cells, has been shown to give significant improvements in photovoltaic devices' performances [49]. This treatment involves annealing on a hot plate while applying an external voltage greater than the open circuit voltage simultaneously. It improves the performance of solar cells based on poly(3-hexylthiophene) P3HT and [6,6]-phenyl C<sub>61</sub>-butyric acid methyl ester (PCBM), as can be observed by the increase of the short circuit current [49].

As it can be seen in Figure 6.10, there is an important increase in the short circuit current possibly resulting from an increase of the hole carrier mobility. There is also an increase in the open circuit voltage compared to untreated devices, which is presumed to result partly from a burning of shunts.

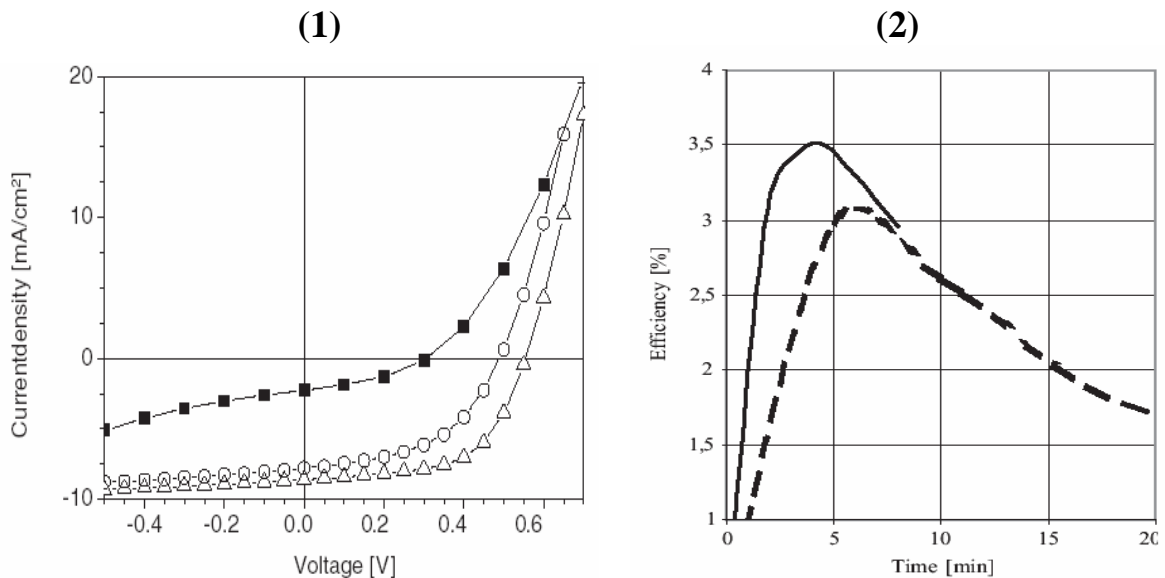
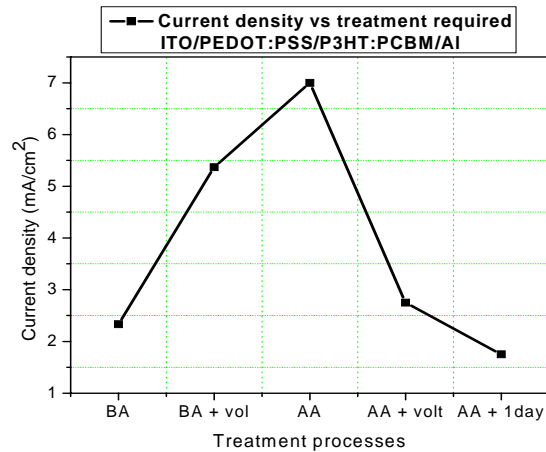


**Figure 6.10.** J-V curves of P3HT:PCBM (1:1 weight ratio) under illumination at white light 80 mW/cm<sup>2</sup>. Produced solar cell (filled squares), annealed solar cell (open circles), solar cell simultaneously treated by annealing and applying an external electric field (open triangles) (1). Influence of the duration of the postproduction treatment. Annealing (dotted line), annealing plus external voltage (solid line) (2). Reproduced from [49].

Figures 6.10 (1) and 6.10 (2) also show values of  $V_{OC} \sim 0.30$  V,  $J_{SC} \sim -5$  mA/cm<sup>2</sup> and a power conversion efficiency of around 0.4% without any treatment. Values of  $V_{OC} \sim 0.50$  V,  $J_{SC} \sim -7$  mA/cm<sup>2</sup> and a power conversion efficiency of around 2 % when the solar cell was annealed for 4 min were observed. Values of  $V_{OC} \sim 0.55$  V,  $J_{SC} \sim -8.5$  mA/cm<sup>2</sup> and a power conversion efficiency of around 3.5 % when the sample was annealed while an external voltage greater than the open circuit voltage was



simultaneously applied. The influence of the duration of the postproduction treatment is shown in Figure 6.10 (2). A maximum efficiency is found for treatment duration of 5-6 minutes for annealing only and 4 minutes for annealing while simultaneously applying a potential. Longer postproduction treatment times tend to decrease the efficiency dramatically. From devices such as ITO/PEDOT:PSS/P3HT:PCBM/Al studied in Section 6.3.2, the maximum efficiencies were found by heating the samples up to 140 °C for a duration of 4 minutes.



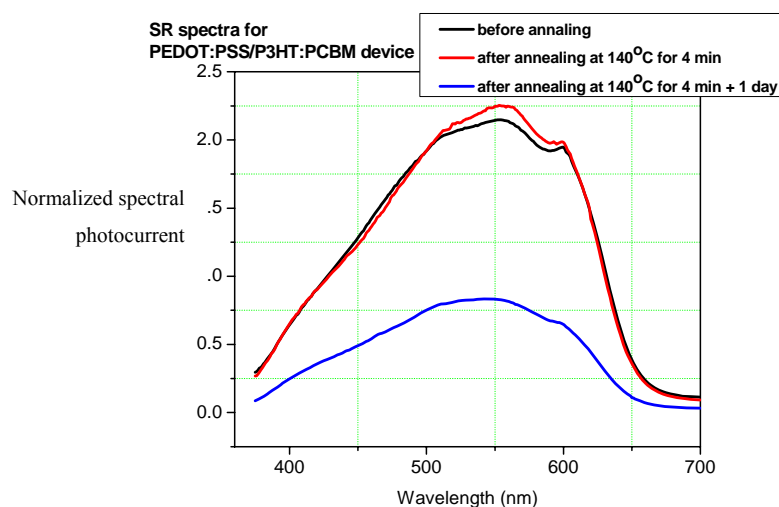
**Figure 6.11.** Current density decay after different treatment processes.

Figure 6.11 shows the current density results after different treatment processes. The aim was to study the current density decay to see how the device performance devices changed after different treatment processes. ITO/PEDOT:PSS/P3HT:PCBM/Al solar cells were analysed for comparison of the different treatments. Firstly, the solar cell was analysed before annealing (*BA*) and the measured current density found was 2.33 mA/cm<sup>2</sup>. Another solar cell sample had a higher voltage in the dark (*BA + volt*) to enhance the photocurrent density and improve the charges mobility in the device, in other words, the sample was excited in the dark from 0 volts to 10 volts in order to see the behaviour of the device afterwards. In this device the current density found was higher, 5.33 mA/cm<sup>2</sup>. Previously another sample was annealed at 140 °C for 4 minutes (*AA*) and even greater current densities than before annealing were observed with the short circuit current density found to be around 7.00 mA/cm<sup>2</sup>. A fourth sample was annealed and afterwards a higher voltage (*AA + volt*) was applied in the dark, the short circuit current density found, 2.75 mA/cm<sup>2</sup>, was lower than measured without applying any additional voltage. The last test was taken after leaving the sample for one day in the glove box under nitrogen atmosphere and also after annealing the device before testing (*AA + 1 day*), 1.75 mA/cm<sup>2</sup> was the short circuit value found.

### 6.3.6 Optical properties of blend films

Optical properties of P3HT/PCBM blends have been studied before and after annealing. Spectral responses and also absorption spectroscopy of these blends were analysed in detail.

Figure 6.12 shows the photocurrent spectral response of pristine P3HT / PCBM blends using different time annealing treatments. There was an increase in the photocurrent intensity after annealing at 140°C for 4 minutes, the spectral response between 520 nm and 650 nm increases according to previous results [48] but just a small increase is observed.



**Figure 6.12.** Normalized spectral photocurrent response of PEDOT:PSS/P3HT:PCBM before annealing, after annealing at 140°C for 4 minutes and after annealing for 24 hours.

The sample left in the glove box under a nitrogen atmosphere for a day was retested to try and reproduce the same performance got directly after annealing. The performance of the device was worse than the day before as the photocurrent intensity had decreased. The spectral response of the PEDOT:PSS/P3HT:PCBM decreased after a day under a nitrogen atmosphere compared to the day before. This leads to a decrease the overall short circuit current density, the spectral response, and therefore, the final power conversion efficiency.

The decrease in the spectral response indicates that the mobility of the charge carriers had fallen since the day before. So the photocurrent response has decreased, probably due to the degradation of contacts. The photoactive layer had lost its performance which contributed to get lower power conversion efficiencies.

As it can be seen in Figure 6.13, there was no change in the absorption spectrum

of P3HT after annealing, just a small increase in the absorption intensity. As the P3HT is annealed, the absorption intensity peak at the wavelength 520 nm remained constant relative to the unannealed film. The height of the peak at the wavelength 550 nm increased compared with that of the unannealed sample. The absorption shoulder is observed at the same wavelength, 620 nm, for the unannealed and annealed P3HT component.

In the case of the PEDOT:PSS/P3HT:PCBM composite or P3HT:PCBM (note that the addition of PEDOT:PSS did not change the absorption spectrum of the composite films) three peaks can be distinguished in the absorption spectrum of the unannealed film. The peaks found around 285 nm and 340 nm resulted from the PCBM compound, while the peak at 460 nm represents the contribution of P3HT. Note that before annealing PCBM inhibits the peak of P3HT. After annealing an important change in the absorption spectrum was found, the PCBM peaks at 285 nm and 340 nm remained almost unchanged, just a small change in the absorption intensity could be seen, but in the region of the P3HT absorption a red shift was observed, improving the spectral overlap with the solar emission spectrum.

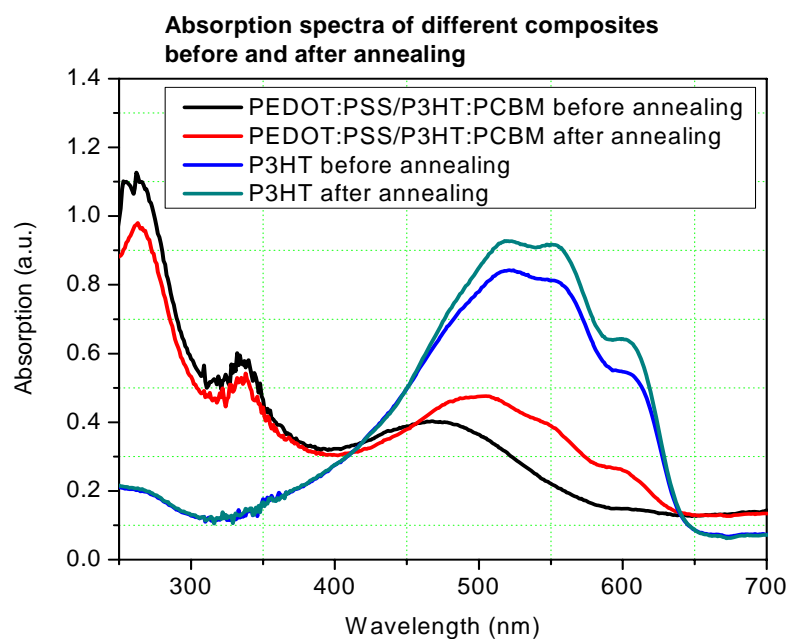


**Figure 6.13.** UV-Vis absorption spectra of PEDOT:PSS/P3HT:PCBM composite film and P3HT films before and after thermal annealing at 140°C for 4 minutes.

The peak around 460 nm was shifted to higher wavelengths 510 nm after 4 minutes of annealing treatment on a hot plate at 140 °C degrees. There was also another peak observed at 550 nm and an absorption shoulder was found around 600

nm. The overall absorption spectra found was quite different compared to the untreated case. The peaks at 250 nm and 340 nm are the contribution of the PCBM on its own.

An explanation of the differences in absorption spectra, is given as follows: when the P3HT:PCBM film is heated to a certain temperature, in this case up to 140°C, the fullerene PCBM diffuses into the P3HT polymer matrix increasing the volume of the latter. This is when PCBM clusters appear [48]. As explained before in Section 5.5.2, PCBM molecules disorder the molecular structure of P3HT chains and hence reduce the density of the aggregates that cause the red absorption. For P3HT:PCBM there are no well defined shoulders in the absorption spectra, just a smooth curve at much lower absorption, that indicates there is no crystallinity and possibly also the polymer inter-chain order is much smaller. X- ray diffraction shows no crystallisation before annealing [44], this is because PCBM is small enough in size to get in between the P3HT chains so the polymer can not crystallise. After annealing, there is some diffusion of PCBM into domains outside the polymer, so the polymer can crystallise again resulting in better photovoltaic performance. This analysis of changes in the film morphology suggests that the improved photovoltaic responses after annealing were due to changes in the films crystallinity and aggregation within the PCBM nanophase.

Absorption spectra for P3HT:PCBM films treated for different annealing times were analysed. A pronounced red shift was observed, which became more evident when the annealing time exceeded 4 minutes.

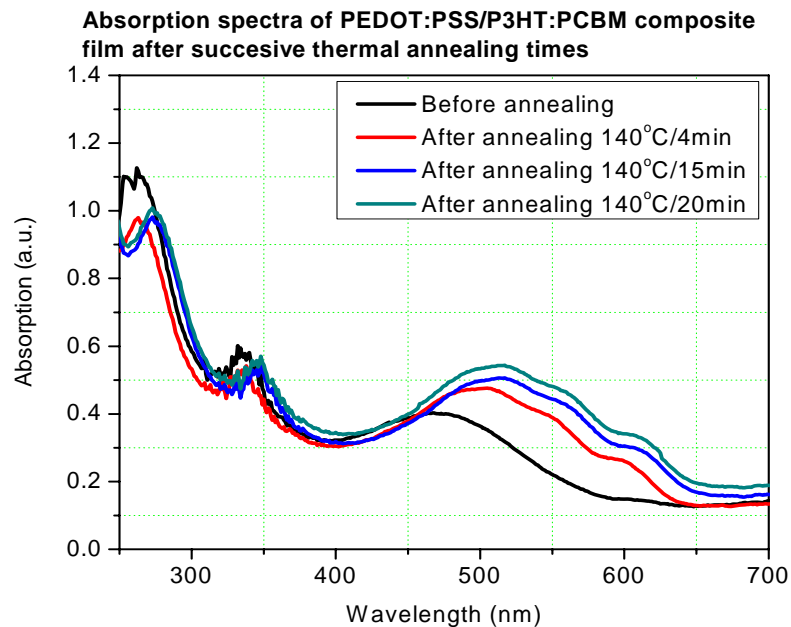


**Figure 6.14.** UV-Vis absorption spectra of PEDOT:PSS/P3HT:PCBM composite film after successive thermal annealing steps.

As it can be seen in Figure 6.14, when the films were annealed at 140°C for more than 4 minutes, the peaks at wavelengths of 510 nm and 550 nm are shifted to higher wavelengths. After 15 minutes peaks at 530 nm and 570 nm were observed and also the absorption shoulder was shifted to around 620 nm. The red shift became more evident after 15 and 20 minutes of thermal annealing.

Absorption spectra for P3HT:PCBM as a function of the PCBM weight ratio is shown in Figure 6.15. A red shift is observed as the concentration of PCBM into P3HT:PCBM composite is increased after annealing. However for increasing smaller amounts of PCBM added, the absorption profile becomes closer to that of pure P3HT. Note that P3HT remained unchanged after annealing.

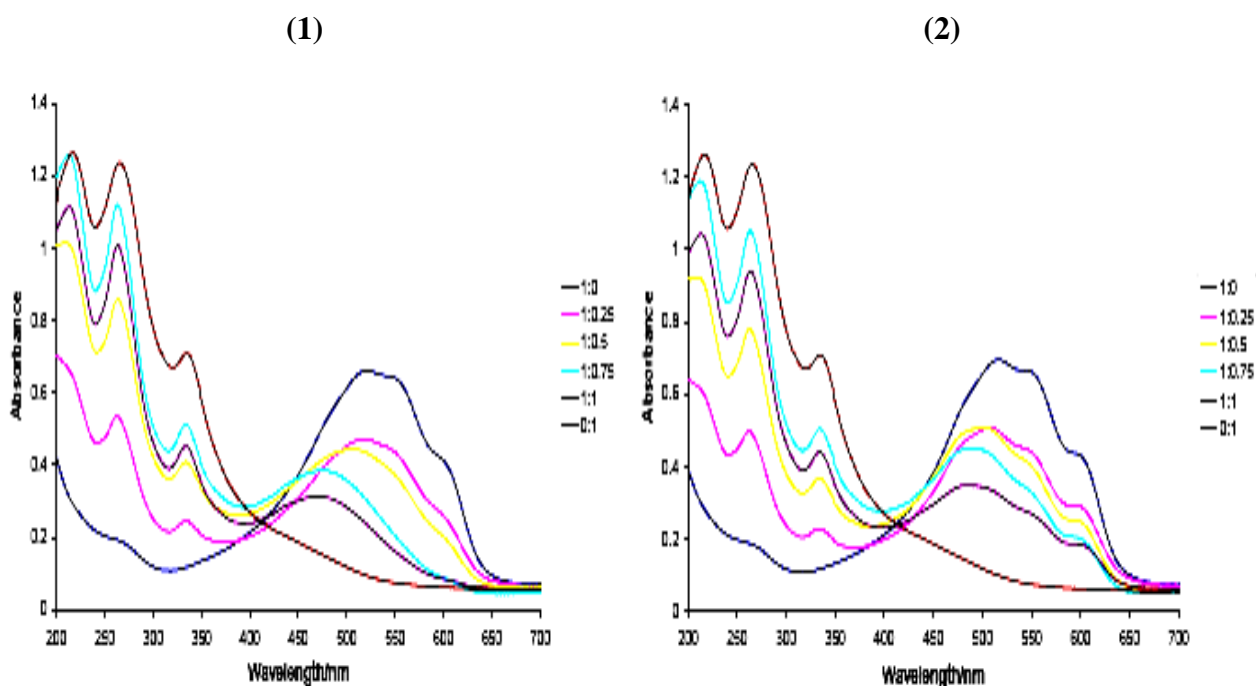


**Figure 6.15.** UV-Vis absorption spectra of P3HT:PCBM composite films as function of PCBM weight ratio before annealing (1) and after annealing at 140°C for 4 minutes (2).

It was also observed that the thermal evaporation of aluminium electrodes can result in the samples being annealed. The evaporator can be used at temperatures up to 250°C and when the samples were removed and the absorption spectra of the films after evaporating and compared the result to the films before and after evaporation were compared it was found that they were similar to the samples annealed at 140 °C for 4 minutes. In conclusion, we acknowledge that evaporation annealed the films but not as much as the hot plate did. The results are shown in next Figure 6.16. It is evident that the heat which the blend films are exposed to during evaporation of the cathode is sufficient to anneal them. However, if the blend is then annealed at 140°C for 4 minutes, the absorption bands become still better defined and the magnitude of

absorption increases. This observation implies that that annealing conditions caused by the evaporation process are less severe than that when the device is annealed for testing.

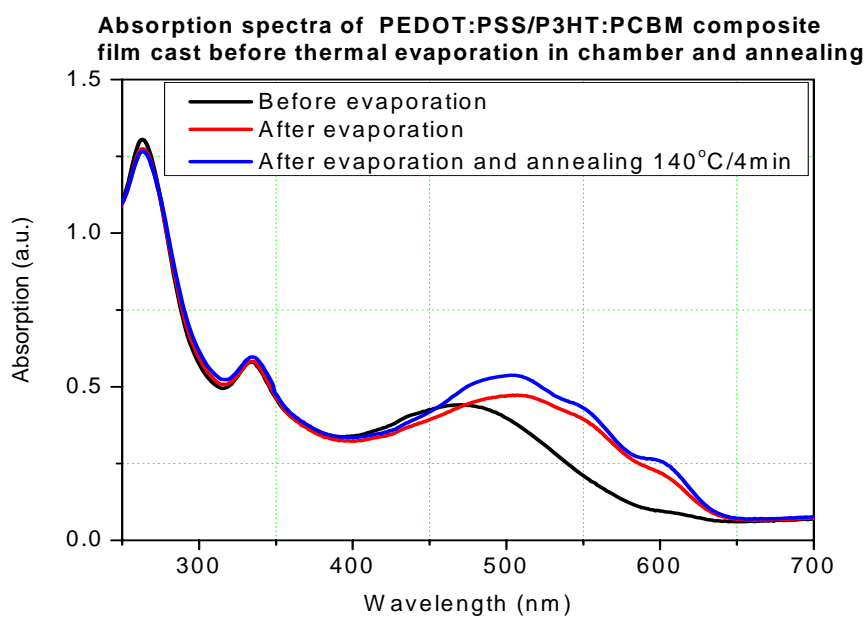


**Figure 6.16.** UV-Vis absorption spectra before evaporation Al electrodes, after evaporation, and after evaporation and annealing.

### 6.3.7 Differential Scanning Calorimetry analysis

The thermochromic properties of poly(3-alkylthiophene)s (P3AT)s have been studied in the early 1990s [50-56]. In the case of partially crystalline P3ATs, the thermochromic transition (change in colour as a function of temperature) is remarkable over the temperature range for order-disorder phase transition, i.e. the crystal melting.

Poly(3-hexylthiophene) (P3HT) is one of the most studied P3ATs, and is known as a semicrystalline polymer. The crystalline structure of P3HT has been investigated by a number of research groups [57-58].

Differential Scanning Calorimetry (DSC) analysis was carried out on all samples. Firstly, the crystallisation of the polymer P3HT was investigated. Secondly, the interaction of the PCBM and their influence on crystallisation in blends such as P3HT:PCBM was investigated. Finally, DSC on fullerene PCBM was carried out.

According to Zhao et al [59], the glass transition and the melting point temperatures of P3HT were 12 °C and 178 °C, respectively, whereas Chen et al [61] determined a melting temperature of 240-245 °C for regioregular P3HT, and no

indication for a glass transition was given.

In this case, Figure 6.17, the onset of the glass transition ( $T_g$ ) of the P3HT polymer was observed at  $\sim 46$  °C while a strong melting point appeared at  $\sim 224$  °C. The thermal transition behaviour reported in this work is totally different from that reported from Zhao et al [58] or D. D. C. Bradley et al [47, 60].

As it was discussed in Section 4.4.5, normally in DSC, the initial heat of the heat-cool-heat cycle is used to eliminate the thermal history of a sample and the second heat step is accepted as the true melting characteristic of the sample [62]. The DSC heat-cool-heat cycle of just the P3HT polymer powder is shown in Figure 6.17.

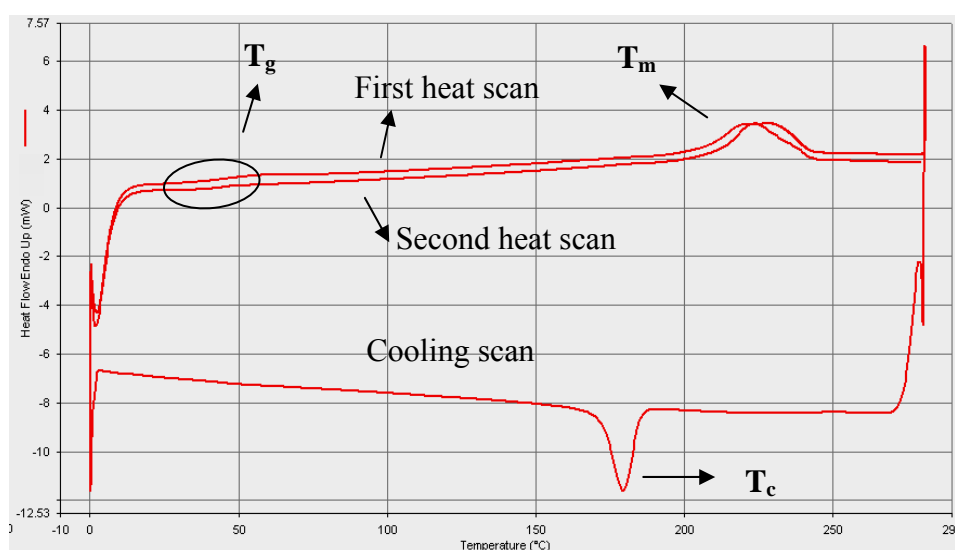


**Figure 6.17.** DSC results obtained of P3HT.

As discussed in Section 4.4.4, each aluminium disk was found to weigh  $4.0 \pm 0.3$  mg and two disks were used in the calorimetric measurements, one used as a reference and the other one containing the sample to be analysed. Flowing helium gas was employed to purge any remaining solvent from the sample.

Most of the samples were heated from 0 °C to 280 °C at a rate of 40 °C/min and then cooled to 0 °C at 40 °C/min using a controlled liquid nitrogen feed, apart from the PCBM which was heated up to 340 °C. Note that baselines were taken using empty pans to ensure better calorimetric results of all the samples to be analysed.

Figure 6.18 shows the glass transition temperature ( $T_g$ ), the melting temperature ( $T_m$ ) and the crystallisation temperature of ( $T_c$ ) of the P3HT polymer in Figures (1), (2) and (3) respectively, magnified from Figure 6.17.

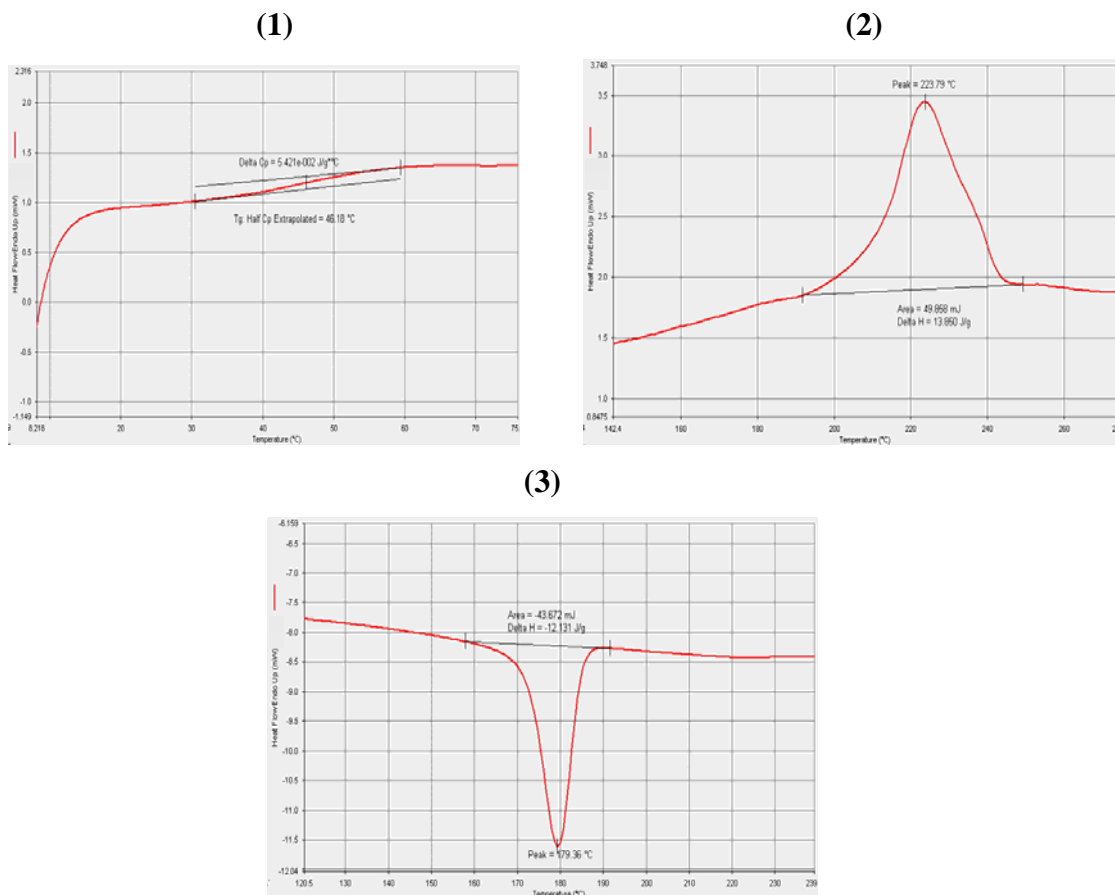


**Figure 6.18.** DSC results obtained of P3HT.  $T_g$ ,  $T_m$  and  $T_c$  temperatures are shown.

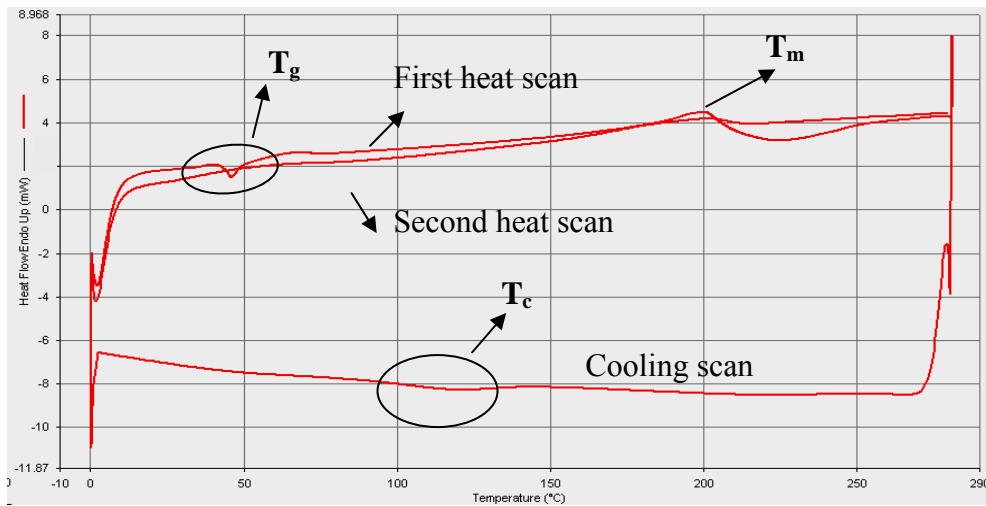
As commonly observed in polymers, the melting temperature depends on the crystallisation conditions. The transition enthalpy as determined from the data in Figure 6.18 (2) was  $\Delta H = 13.850 \text{ J/g}$ , obtained by integration of the heat capacity curve between two temperatures,  $190 \text{ }^\circ\text{C}$  and  $250 \text{ }^\circ\text{C}$  in this case. Annealing of P3HT films can result in slightly increased crystallinity, depending on the drying conditions of the cast films [63].

DSC analysis of P3HT:PCBM composite films were studied to see differences in melting and crystallisation temperatures. Figure 6.19 shows the results of P3HT:PCBM composite.

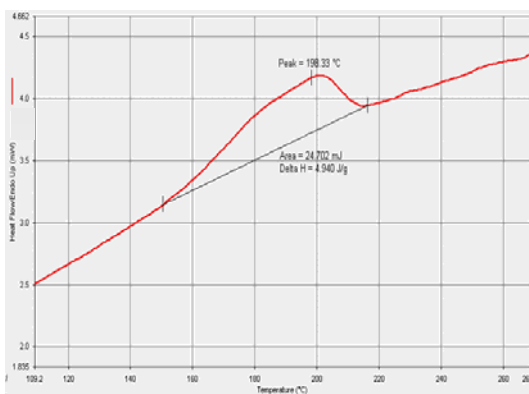
As discussed previously in Section 6.3.6, in P3HT:PCBM composite, the PCBM suppresses the formation of polymer crystallites. PCBM is dispersed on a molecular basis between alkyl chains preventing P3HT aggregation or crystallisation. It can be observed that the main effect of annealing was the redistribution of PCBM. At elevated temperatures above the glass transition, isolated molecules of PCBM begin to diffuse into larger aggregates. In these PCBM regions the P3HT aggregates can be converted into P3HT crystallites. This would lead to better electron transport in PCBM clusters and improvement in the absorption properties of P3HT crystallites.



(1)



(2)



(3)

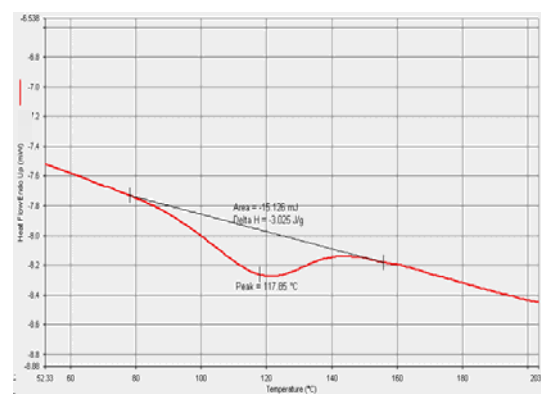


**Figure 6.19.** DSC results obtained of the P3HT:PCBM composite with  $T_m$  and  $T_c$ .

In Figure 6.19, the transition enthalpy of the melting temperature as determined from the data in Figure 6.19 (2) was  $\Delta H = 4.940$  J/g (integration range: 140 °C - 215 °C). The crystallization and cooling extend over a large temperature range as it is typical for semicrystalline polymers [58]. The crystallisation temperatures observed for P3HT and P3HT:PCBM blends were  $\sim 180$  °C and  $\sim 120$  °C respectively, while the melting temperatures were  $\sim 225$  °C and  $\sim 200$  °C. Figure 6.19 shows that in P3HT:PCBM composite, PCBM reduces the formation of polymer P3HT crystallites. This decrease in temperatures is due to the fact that the fullerenes can play the role of lubricants of the polymer chains facilitating their fluidity. The transition enthalpy of crystallisation exothermic peaks is very different: in P3HT it was  $\Delta H = 12.131$  J/g and once PCBM were added the enthalpy decreased to  $\Delta H = 3.025$  J/g, value taken from Figure 6.19 (3). So the crystallinity of P3HT:PCBM is reduced when PCBM is added.

As discussed in Section 6.3.6, comparing the absorption spectra of P3HT and P3HT:PCBM the well defined peaks and shoulders at 500 nm, 550 nm and 600 nm change their forms to a smooth curve when PCBM is added to P3HT, this indicates

there is no crystallinity when the composite film is unannealed, but P3HT crystallises again when the composite is annealed. Despite this reduction in the crystallinity, the P3HT is still being crystallised in P3HT:PCBM composites.

Figure 6.20 shows DSC analysis of the fullerene PCBM taken for higher temperatures (0 °C - 340 °C). Values of the melting temperature  $T_m$  around 290 °C and its enthalpy  $\Delta H = 11.908$  J/g (integration range: 260 °C - 300 °C) were found. Lower heating rates of 10 °C/min and 5 °C/min were used.

After taking a look at the DSC diagram in Figure 6.20, one can see that there is no crystallisation of PCBM on cooling, but in some way this is not real. There is no glass transition temperature ( $T_g$ ) appreciable, the crystallisation exothermic peak is not represented and another melting peak appears after the second heating scan (these surprising results were reproducible). These effects are not very clear and they could be related to the reorder of the organic part of the fullerene, the degradation of the fullerene or even due to the cold crystallization. The concept of cold crystallization means the appearance of the crystallization during the heating process. The process of cold crystallization takes place when a crystalline structure reorganizes low energetic defects of the crystal. This process of crystallization is different from the molten crystallization where the material, initially in liquid state, crystallises below its melting temperature  $T_m$  and over its glass transition temperature  $T_g$  during the cooling process. So there is PCBM crystallization at certain level. Different results with no reference for PCBM crystallites showed that the PCBM is not crystallised in P3HT:PCBM composites [44].

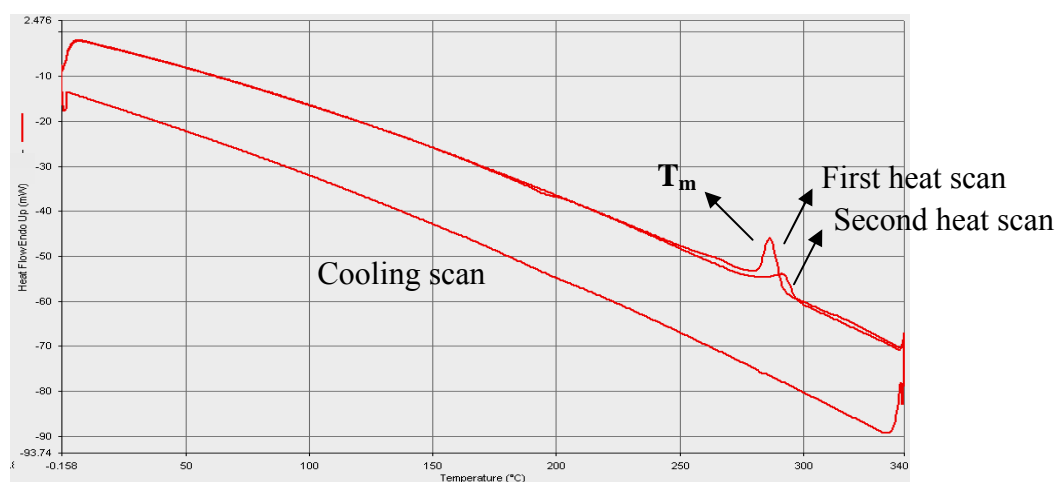


**Figure 6.20.** DSC results obtained of fullerene PCBM.

A problem sometimes found in crystallization studies is that a certain number of materials do not crystallise completely, even partially on cooling.

Going back to the P3HT:PCBM blend, heating the blend up to more than

300°C, the P3HT melting peak appears but the PCBM peak does not, which means that the decomposition temperature of PCBM decreases within the blend, suggesting that the PCBM can be unstable in the blends and the highest percentage of crystallization is almost coming from the polymer P3HT. Also, as is shown in Figure 6.4, in Section 6.3.2, as the organic part of the fullerene disappears after annealing, the colour of the blend gets darker recovering the coloration of the polymer indicating that the crystallisation of the P3HT has increased by annealing.

As discussed before, annealing treatments produced better hole conductivity through P3HT, and also due to the large value of the short circuit current density, there is an increased electron mobility and transport in the PCBM resulting in higher efficiencies, 2.28 % in this case.

### 6.3.8 Morphology studies

To probe the crystallisation of P3HT:PCBM film composites, AFM images were taken before annealing and after annealing. P3HT:PCBM composite films were spun on quartz substrates and AFM images were taken under tapping mode. The surface images of the prepared devices are shown in Figure 6.21.

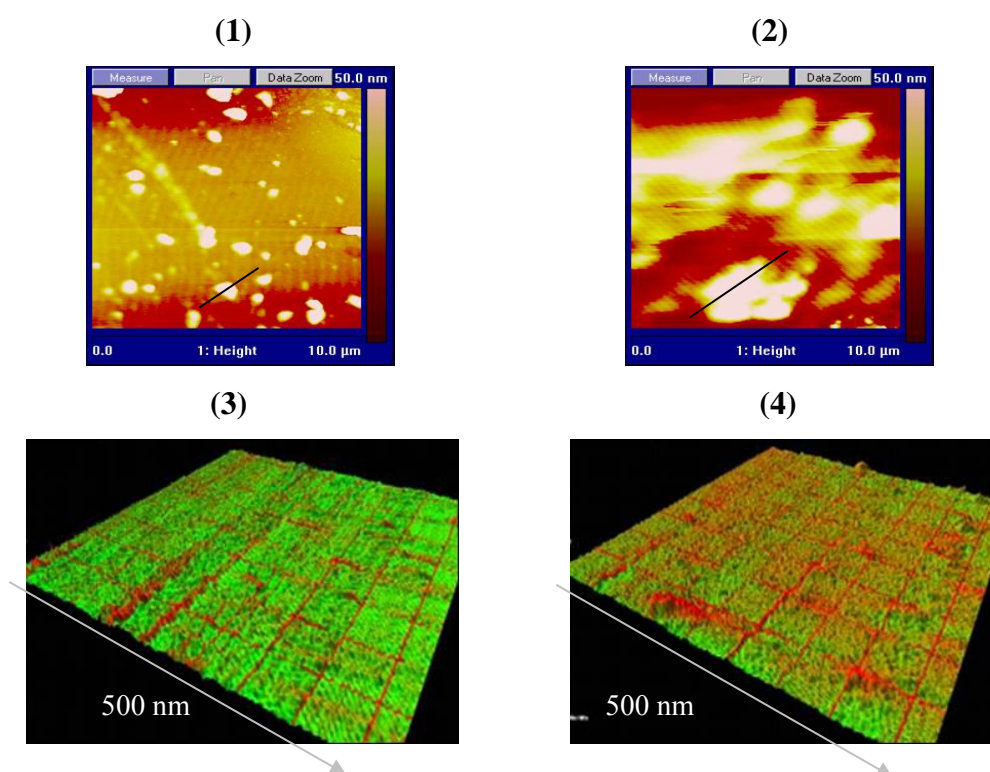


**Figure 6.21.** AFM images of P3HT:PCBM composite films in pristine conditions (1) and after annealing treatment at 140 °C for 4 minutes (2). 3-Dimensional AFM comparison of P3HT:PCBM composite films in pristine conditions with average height ~ 30 nm (3) and annealed conditions at 140 °C for 4 minutes with average height ~ 50 nm (4). Grid size 500nm.

As it can be seen in Figure 6.21 (1), big clusters of PCBM appear when AFM images of the unannealed composite films are taken. In particular the lateral size and height of these features are  $\sim 0.7 \mu\text{m}$  and  $\sim 80 \text{ nm}$ , respectively.

As discussed previously, the presence of PCBM seems to suppress the formation of polymer crystallites. Most likely, PCBM is dispersed between the chains of the P3HT preventing the formation of P3HT crystallites. For this reason the photovoltaic response of these devices are worse before annealing than after annealing, but it needs to be considered that there is a big improvement in photovoltaic performance when PCBM is added to P3HT. After annealing, PCBM begins to diffuse into larger aggregates; a redistribution of PCBM can be seen in Figure 6.21 (2), where features at  $\sim 90 \text{ nm}$  in height and approximately  $\sim 4\text{-}5 \mu\text{m}$  lateral size were found. Therefore, annealing effect causes the redistribution of PCBM into bigger clusters contributing to the electron transport, and also the crystallisation of P3HT contributes to the hole transport while PCBM clusters contributes to the electron transport through the clusters. It has been mentioned from different research groups [65, 66, and 67] that these big PCBM are also crystals.

Figures 6.21 (3) and 6.21 (4) show 3-Dimensional AFM images taken on P3HT:PCBM composites films. It can be seen that the average roughness increases after annealing due to the bigger PCBM clusters.

It has to be also mentioned that generally the phase separation within the blend starts already in the solution because the relative solubilities of the two components in the solvent are significantly different, but is halted the moment by the film formation during spin coating process. The spin coated film represents a frozen-in picture. This higher roughness after annealing provide perhaps a greater surface area on the cathode resulting in larger effective device areas as well as conducting paths and also better photovoltaic responses.

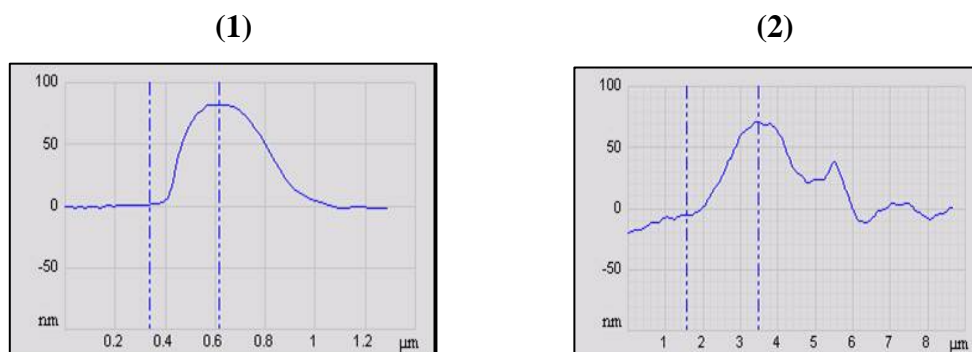


**Figure 6.22.** Height line scans taken across the P3HT:PCBM composite film device AFM images of Figures 6.21 (1) and 6.21 (2) respectively.

Scanning Electron Microscopy (SEM) was another technique used to understand the performance and nanoscale morphology of the composite films. SEM images, shown in Figure 6.23, were taken of the surface of P3HT:PCBM composite films.

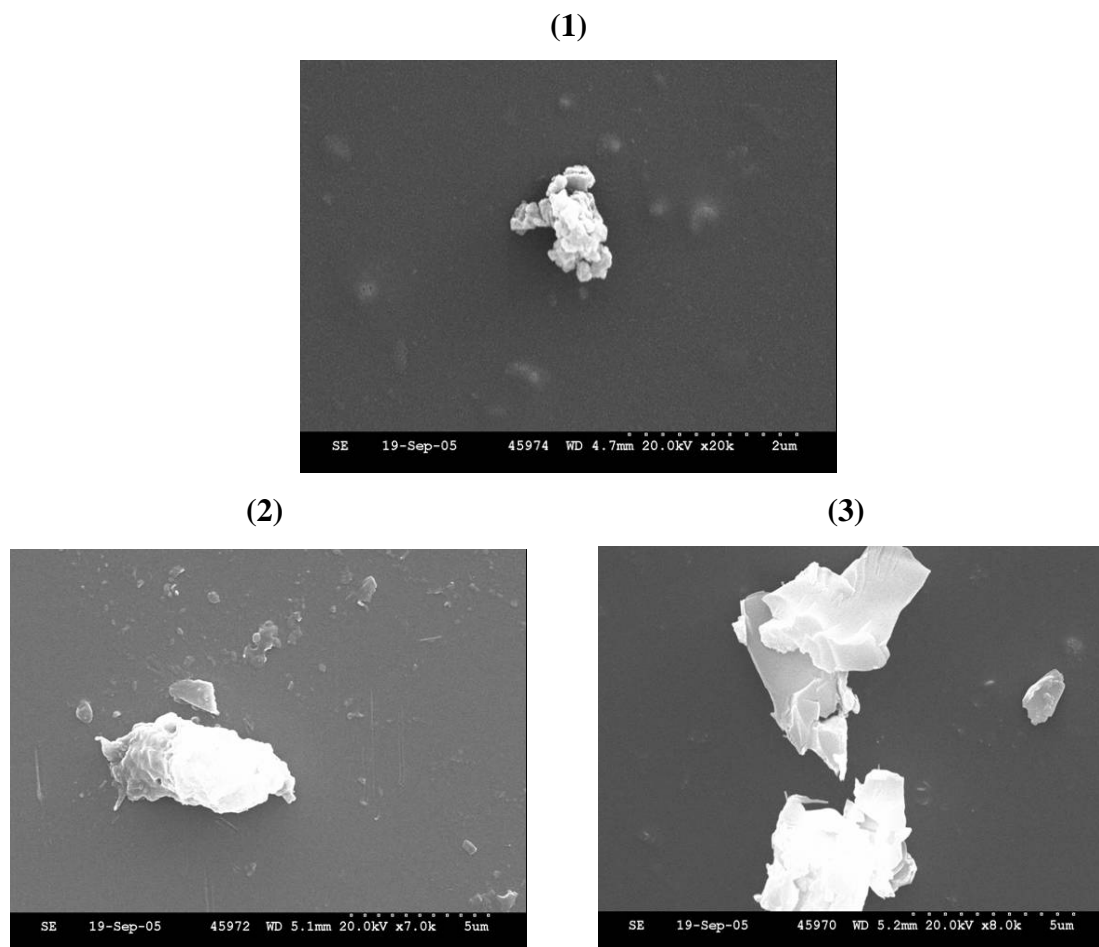


**Figure 6.23.** SEM images of P3HT:PCBM (1:1) composite film in pristine conditions, (1), and after annealing at 140 °C for 4 minutes, (2) and (3).

As it can be seen in Figure 6.23 (1), the presence of PCBM in the unannealed polymer is not very clear even if a small feature around 0.5-1.0  $\mu\text{m}$  is shown. Whether this feature is real or not is not very clear. What is very clear is that after annealing big clusters embedded in the polymer layer were found. Figure 6.23 (2) shows some of the polymer crystals after thermal annealing treatment. Figure 6.23 (3) shows big clusters of PCBM, about 4-5  $\mu\text{m}$  of length, also after thermal annealing treatment.

A conclusion taken from the last images is that the appearance of clusters of PCBM covered by the polymer could explain the improved photovoltaic performance after thermal annealing. This situation increases absorption intensities and also electron transport through the PCBM clusters.

Transmission Electron Microscopy (TEM) images taken of P3HT:PCBM film composites shown in Figure 6.24 show the nanomorphology of the composite films.

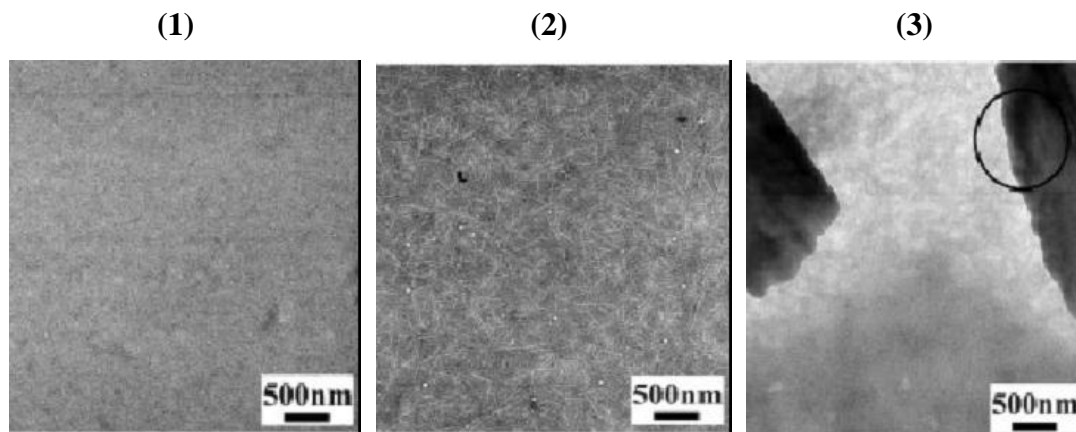


**Figure 6.24.** TEM images of P3HT:PCBM (1:1) composite film in pristine condition, (1), after annealing at 80 °C, (2), and after annealing at 130 °C, (3). Reproduced from [64].

In Figure 6.24 above, the PCBM nanoclusters are quite small and cannot be easily observed before thermal annealing treatment. After thermal annealing featureless appearance of the film changed into visible fibrillar regions stemming from the formation of P3HT crystals and big PCBM clusters.

## 6.4 Conclusions

In this Chapter, the studies of thermally-controlled interdiffusion of a conjugated polymer and fullerenes in organic photovoltaic devices that were introduced in the last Chapter were continued.

Polythiophene and fullerene blends were characterised by current-voltage analysis, spectral photocurrent response, UV-Vis absorption spectroscopy, DSC analysis and morphology studies for unannealed and annealed devices.

An important observation taken from the I-V analysis is that the photovoltaic response of ITO/PEDOT:PSS/P3HT:PCBM/Al was improved after thermal annealing treatment. Here, the open circuit voltage, short circuit current, and fill factor values were significantly higher compared to the unannealed device, leading to a better power conversion efficiency of 2.28 % which was the maximum efficiency achieved in this work. Definitely a higher value found in comparison with other previous works.

Absorption spectra of the pure P3HT and P3HT:PCBM composite films were investigated. Upon annealing the absorption spectra of P3HT:PCBM blends undergo a

strong red-shift, improving the spectral overlap with the solar emission spectrum, which results in an increase of the power efficiency of solar cells. Almost no change was observed in the case of the pure P3HT.

From DSC analysis it has been demonstrated that short annealing times at higher temperatures leads to the formation of a new ordered crystalline structure of PCBM and also an increased crystallization of P3HT. Differences between DSC results taken from P3HT, P3HT:PCBM and PCBM have been also explained.

AFM and SEM images show that annealing the composite above the glass transition temperature of the polymer leads to an increase of the crystallinity of the composite suggesting that the PCBM has reorganized within the crystallised P3HT layer.

This study has therefore not only confirmed the optimal blend ratio for P3HT and PCBM for photovoltaic performance, but has explored the conditions under which phase segregation occurs on annealing, how it occurs and how this links to photovoltaic performance.

# CHAPTER 7 - INFLUENCE OF CARBON NANOTUBES

## 7.1 Introduction

In this Chapter, the effects of using carbon nanotubes and polymer composites in organic photovoltaic devices will be shown. Carbon nanotubes possess excellent mechanical and electrical properties [68]. It is well established that fullerene based molecules are extremely effective in providing phototinduced charge transfer and enhanced electron transport when incorporated into polymer based photovoltaic devices [47]. However significant concentrations of fullerene are required in order to form percolation networks in the device to provide sufficient charge transport. Single walled carbon nanotubes (SWNT) have been previously blended with Poly(3-octylthiophene) (P3OT) and incorporated into photovoltaic devices, raising the short circuit current by two orders of magnitude and giving a two-fold increase in the open circuit voltage compared to a device with no SWNT. This work provided evidence that the interface between the SWNT and polymer was effective in charge separation and that the SWNT were acting as efficient channels for transferring the free electrons [67].

In this work, only composites using multi walled carbon nanotubes (MWNT) and blends of P3HT and PCBM had been fabricated, in the hope of analysing how adding further electron transporters can affect the performance of a blend already capable of producing relatively high efficiencies in PVs. The results presented in this work using single walled nanotubes (SWNTs) were included and taken as a reference.

In order to study the mechanisms of annealing in more in detail, absorption spectroscopy (UV-vis) has been performed on P3HT:PCBM:MWNT blends that have been annealed for various lengths of time. Chemical Vapour Deposition (CVD) has also been used to provide more information about the interaction between polymers and carbon nanotubes due to the growth of the nanotubes can be controlled.

## 7.2 Experimental

Solutions of P3HT and PCBM for spin coating were prepared by dissolving the required masses of each material in chloroform. The concentration of P3HT used was



always 10 mg/ml. Details of the characteristics of the MWNT used can be seen in Section 3.3.1. The required mass of MWNT was dispersed into the P3HT:PCBM solution using a high powered tip for 5 minutes followed by hour in a low power ultrasonic bath at 50 °C. Films were spin cast onto PEDOT:PSS coated ITO patterned substrates immediately after sonication to keep phase separation in solution to a minimum. The PEDOT:PSS layer was previously spin coated onto ITO and dried by baking on a hot plate at 80 °C for 10 minutes. After an aluminium cathode was evaporated on top of the blend layer the devices were tested, the devices were then annealed at 140 °C/4 minutes and re-tested.

## 7.3 Results and discussion

### 7.3.1 Single walled carbon nanotubes

In this Section, single-walled nanotubes (SWNT) in photovoltaic devices were selected as a reference for a better understanding of the function of the nanotubes as they allow the electrons to be efficiently transported to the aluminium electrode via their continuous conductive network [71].

Polymer/single-walled nanotube composites were studied. Poly(3-octylthiophene) (P3OT), which act as the photoexciton electron donors, is blended with low concentrations (>1%) of single walled carbon nanotubes, which act as the electron acceptors [71].

This stable solution has previously been shown to contain pure SWNT as the carbonaceous impurities which have been effectively removed by sedimentation [68-70]. These solutions were used to prepare organic photovoltaic devices, as shown below in Figure 7.1.

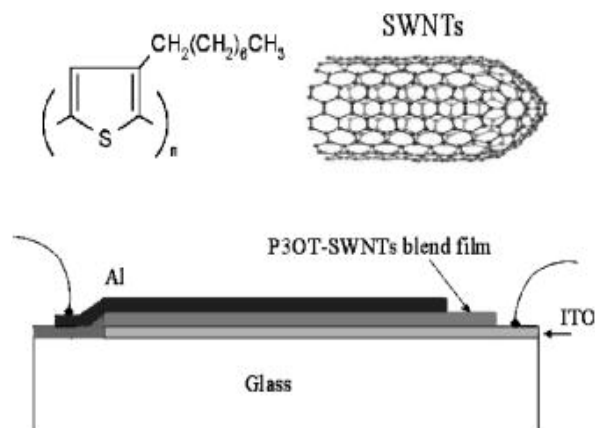


**Figure 7.1.** Chemical structures of P3OT and SWNTs, and device architecture of the P3OT / SWNT photovoltaic cell. Reproduced from [71].

The photovoltaic parameters of the composite and of the device prepared with just the polymer P3OT are shown in Table 8.

Sample	Jsc (mA/cm <sup>2</sup> )	Voc (V)	(JV)max (mA.V/cm <sup>2</sup> )	FF (%)	$\eta_e$ (%)
P3OT	$0.70 \times 10^{-3}$	0.35	$7.35 \times 10^{-5}$	30.05	$2.50 \times 10^{-5}$
P3OT / SWNT	0.12	0.75	$3.60 \times 10^{-2}$	40.10	0.04

**Table 8.** Short circuit current density ( $J_{SC}$ ), open circuit voltage ( $V_{OC}$ ), maximum power ( $JV)_{MAX}$ , fill factor (FF) and power efficiency  $\eta_e$  of ITO / P3OT / Al and ITO / P3OT:SWNTS / Al devices. Reproduced from [71].

Using 80 mW/cm<sup>2</sup> white light illumination, the P3OT / SWNT blend device shows a short circuit current density of 0.12 mA/cm<sup>2</sup> and an open circuit voltage of 0.75 V with an efficiency of 0.04 %, compared to the P3OT device which shows values of  $0.7 \times 10^{-3}$  mA/cm<sup>2</sup>, 0.35 V and  $2.5 \times 10^{-5}$  %.

One can see that the interaction of the nanotubes with the polymer allows efficient charge separation of the photogenerated excitons in the polymer and improves electron transport to the electrode through the nanotubes. This is shown by the improved photovoltaic performance after the addition of SWNT, which resulted in an efficiency three orders of magnitude greater than the sample without nanotubes. These results show that polymer-SWNT composites represent an alternative organic semiconducting material that can be used in organic photovoltaic cells.

### 7.3.2 Multi walled carbon nanotubes

In this Section, multi walled nanotubes were selected (MWNT) as an active layer in a photovoltaic device.

Previous studies [72] have used buffer layers between an indium tin oxide (ITO) anode and the composite layer in order to avoid short-circuits between both electrodes, ITO and aluminium, which can occur in single-layer composite cells due to the highly conductive nature of MWNT. The choice of MEH-PPV as the thin buffer layer (30-40 nm) was motivated by the need to isolate the composite layer and to provide a good hole transport medium. Therefore, the main solar cells produced were ITO / MEH-PPV / PPV + MWNT / Al, as these were previously shown to give good performance – see Table 9 [72].

A comparison of different solar cells using multi-walled nanotubes as efficient charge transport media is shown in the following Table 9.

Sample	Jsc ( $\times 10^{-3}$ mA/cm <sup>2</sup> )	Voc (V)	FF (%)	$\eta_e$ ( $\times 10^{-4}$ %)
MEH-PPV	-0.84	0.95	16.40	1.63
PPV	-3.40	1.18	15.50	7.75
MEH-PPV / PPV	-0.34	1.05	22.90	1.01
MEH-PPV / PPV + MWNT	-4.05	1.33	16.70	11.2

**Table 9.** Short circuit density ( $J_{SC}$ ), open circuit voltage ( $V_{OC}$ ), fill factor (FF) and power efficiency  $\eta_e$  for each photovoltaic cell: ITO / MEH-PPV / Al, ITO / PPV / Al, ITO / MEH-PPV / PPV / Al and ITO / MEH-PPV / PPV + MWNT / Al. Reproduced from [72].

The spectral response of the MWNT photovoltaic cell exhibited a wide response, while the cells without MWNT showed a narrow response. This result, related to as the optical filter effect, discussed in Section 5.4, is a consequence of the high optical density in the photovoltaic cells without nanotubes. The optimum relative efficiency was obtained for a nanotube mass ratio of 1.2 %.

Previous studies have been shown that the addition of MWNT has increased the short circuit current density and the power conversion efficiency of the device [72].

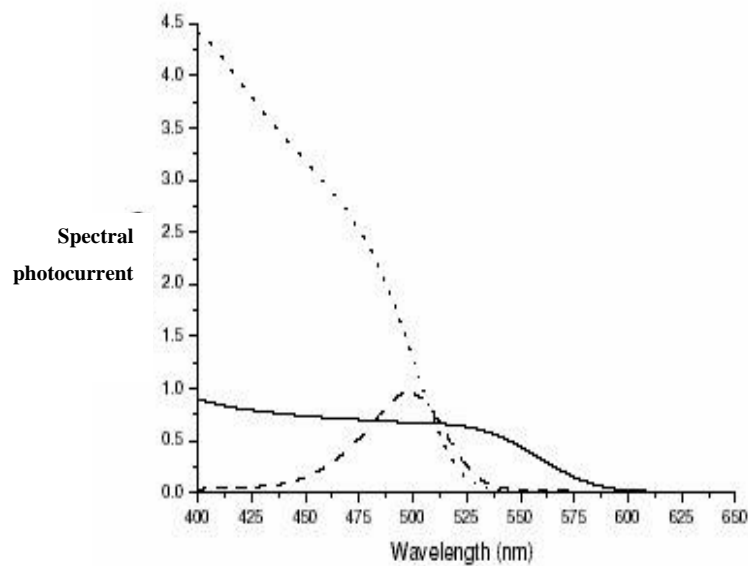


**Figure 7.2.** Spectral photocurrent response of ITO/MEH-PPV/Al (solid line), ITO/MEH-PPV/PPV/Al (dash line) and ITO/MEH-PPV/PPV+MWNT/Al (dotted line). Reproduced from [72].

From Figure 7.2, it was assumed that the introduction of MWNT has widened the active layer. Electron transfer from MEH-PPV to MWNT occurred at the MEH-PPV / PPV+MWNT interface.

Kymakis et al. [71] attributed their two orders of magnitude increase in short circuit current to an efficient charge transfer and transport through SWNT, while Ago et al. [67] explained their increase in quantum efficiency by an energy transfer and partial hole transfer from PPV to MWNT. This suggests that, although some charge and energy transfer is likely to occur in the MWNT photovoltaic cell, we are not seeing the full effect of these processes and the efficient charge transport via the continuous conductive nanotube path to Al electrode, following charge dissociation at the MEH-PPV / PPV interface, could play a more important role.

Figure 7.3 below shows the variation in spectral response for MEH-PPV and MWNT blend as a function of nanotubes weight concentration. The spectral response is wider as the concentration of nanotubes increases.

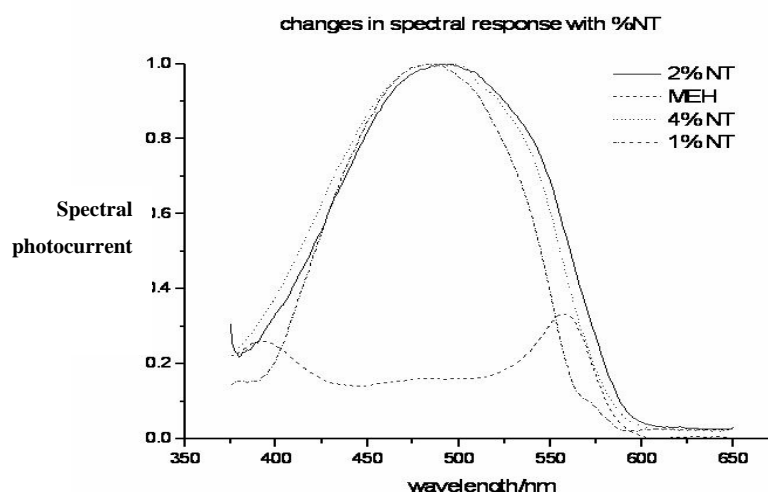


**Figure 7.3.** Spectral photocurrent response of MEH-PPV and MWNTs as a function of % nanotubes weight ratio concentration.

As discussed in Chapter 6, polythiophenes such as poly(3-octylthiophene) (P3OT) and poly(3-hexylthiophene) (P3HT) can be used as electron donor materials in organic photovoltaic devices.

In this work, P3HT polymer and multi-walled carbon nanotubes (MWNT) were used to make composites for production of solar cells. P3HT and MWNT composites solutions were made in order to make organic photovoltaic devices and check their efficiency.

For these devices, short circuiting has been got even if P3HT was being used as buffer layer in between the ITO anode and the composite P3HT+MWNT. These short

circuits in these devices are shown in Figure 7.4.

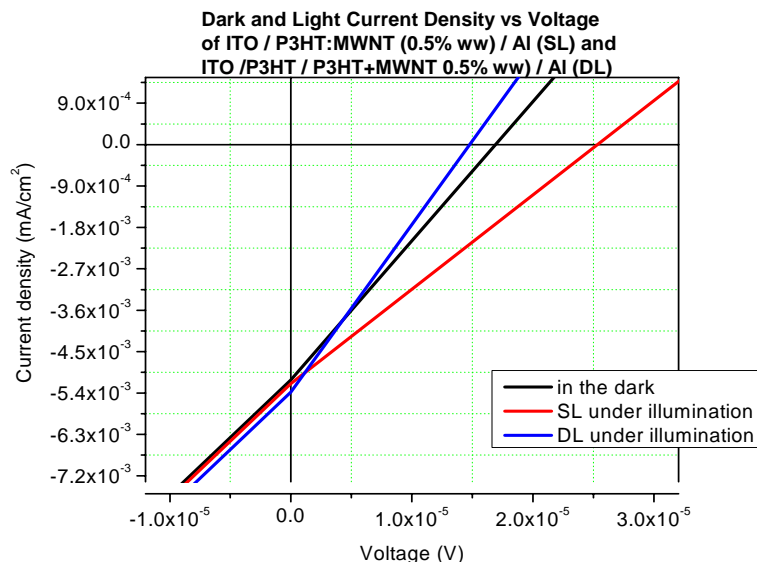


**Figure 7.4.** J-V characteristics of P3HT and MWNT composite devices tested in the dark and using  $80 \text{ mW/cm}^2$  white light illumination.

The average open circuit voltage  $V_{oc}$  of these particular single and double layer devices was  $\sim 2.00 \times 10^{-5} \text{ V}$  (extremely low) and the average short circuit current was  $-5.27 \times 10^{-3} \text{ mA/cm}^2$  at a monochromatic illumination of  $80 \text{ mW/cm}^2$ . Average values were taken because there is a very little difference between the values in the dark and the values under illumination. So, no improvements in terms of power efficiencies using polythiophene / multi-walled carbon nanotube composites were found. Short circuiting was found for all the P3HT/MWNT photovoltaic devices.

There are several different reasons why short circuiting appeared in P3HT and MWNT composites. One of these reasons could be that the dispersion of nanotubes in P3HT solutions was not good enough to get nice composite films. The importance of solvents used has been studied previously in different research groups. The other explanation could be the morphology characteristic of nanotubes themselves causes short circuits (explained later).

It was also shown that PCBM has an effect on the absorption spectra of the polymer P3HT, because the PCBM changes the conjugation of the polymer but nanotubes do not have the same effect. Therefore, to improve the photovoltaic properties we should make the nanotubes have this effect when we add them to see changes in absorption. Chloroform is a non-polar solvent, and PCBM has alkyl chains which make it dissolve in non-polar solvents. There is also the possibility of impurities in the MWNTs that may also cause a short circuit.

It should also be mentioned that the geometry of the fullerenes and the nanotubes in the composites are quite different, since fullerenes have 1nm diameter and multi-walled nanotubes are a few microns in length and several nanometres in diameter. In this case, the MWNTs used in this work were 15nm in diameter and 15-20  $\mu\text{m}$  in length. This difference could play an important role in the photovoltaic responses for PCBM and MWNTs.

As discussed in Section 6.3.6, PCBM is small enough in size to get in between the P3HT chains so the polymer can not crystallise. After annealing, there is some diffusion of PCBM into clusters, so the polymer can crystallise again resulting in better photovoltaic performance. Once MWNT are added it seems likely the polymer wraps some part of the nanotubes but not along the complete length of the nanotubes. After annealing the nanotubes can form inactive bundles with no interaction with the polymer-fullerene composite anymore, and therefore the MWNT themselves do not affect the device so the photovoltaic response results return to the same values as without nanotubes.

Solutions of P3HT:PCBM:MWNT (1:1:0.01 by weight) were prepared to analyse the influence of MWNT in P3HT:PCBM composites.

Current-voltage characteristics of MWNT composite devices before and after annealing are shown in Figure 7.5.

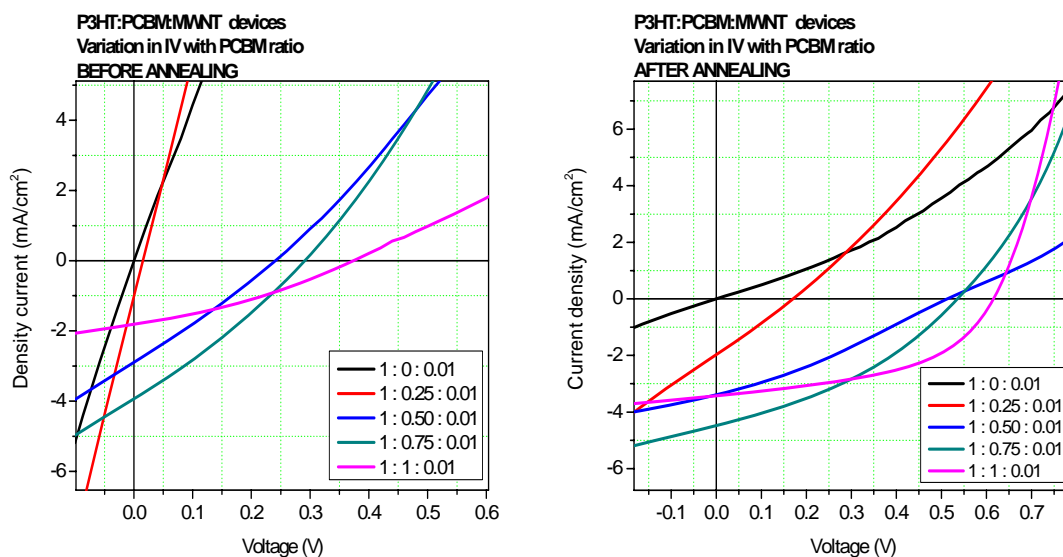


**Figure 7.5.** J-V characteristics of P3HT:PCBM:MWNT composite devices before and after annealing at 140 °C for 4 minutes using 80 mW/cm<sup>2</sup> white light illumination.

As can be seen in Figure 7.5 above, the presence of MWNT, in the P3HT:PCBM composites before annealing, causes an important decrease in the open-circuit voltage and also reduces the power efficiencies. This suggests that the inclusion of nanotubes, and not any effect connected to the PCBM or P3HT, is the likely explanation for shifts in the open circuit voltages and short circuit currents. After annealing, the nanotubes are formed from bundles which have no interaction with the P3HT:PCBM composite and this result in higher values of the open circuit voltage while short circuit currents do not change too much. SEM images of these nanotube bundles are shown in Figure 7.6.

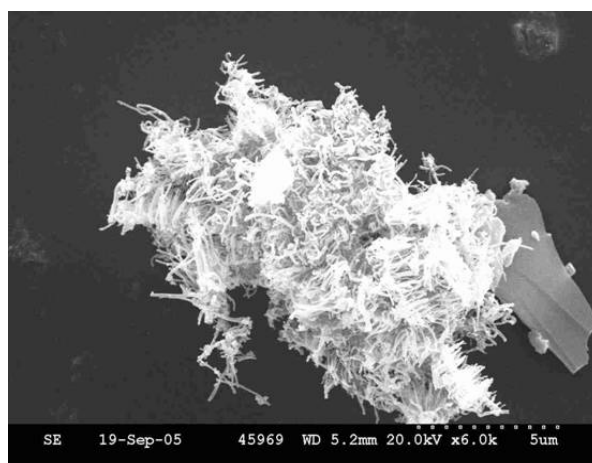


**Figure 7.6.** SEM image taken of the P3HT:PCBM:MWNT annealed composite film.

### 7.3.3 Absorption spectroscopy of P3HT:MWNT composite films

In this Section, absorption spectroscopy studies were performed on films with MWNTs. The addition of MWNTs into P3HT and P3HT:PCBM composites were carried out to analyse the UV-Vis absorption spectra.

As discussed in Section 4.4.3, absorption spectroscopy data reflect the vibrational energy distribution of the first excited state of a molecule or system of molecules either in solution or in solid state form. No shift in the absorption spectrum of blends will indicate no ground state electronic interaction between the different macro-molecules involved. However, a red shift in the absorption data is not necessarily a signature of a ground state interaction, but is often due to increased conjugation upon doping.

Absorption spectrum was taken on P3HT and P3HT:MWNT film composites before and after annealing at 140°C for 4 minutes. MWNTs were used at 0.5% weight

ratio. Figure 7.7 shows the absorption spectra.

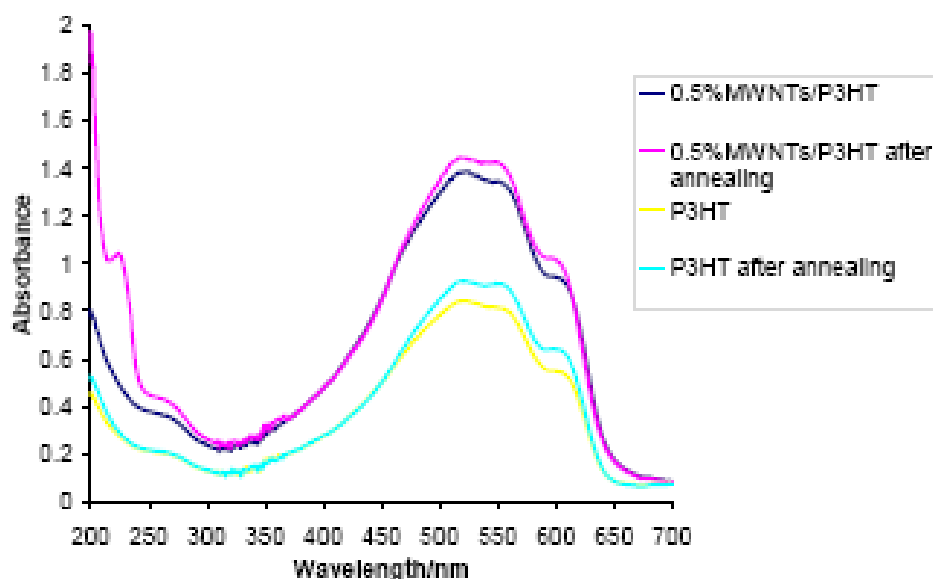


**Figure 7.7.** UV-vis absorption spectra of P3HT films, with and without the addition of wt% MWNTs, before and after annealing at 140°C for 4 minutes.

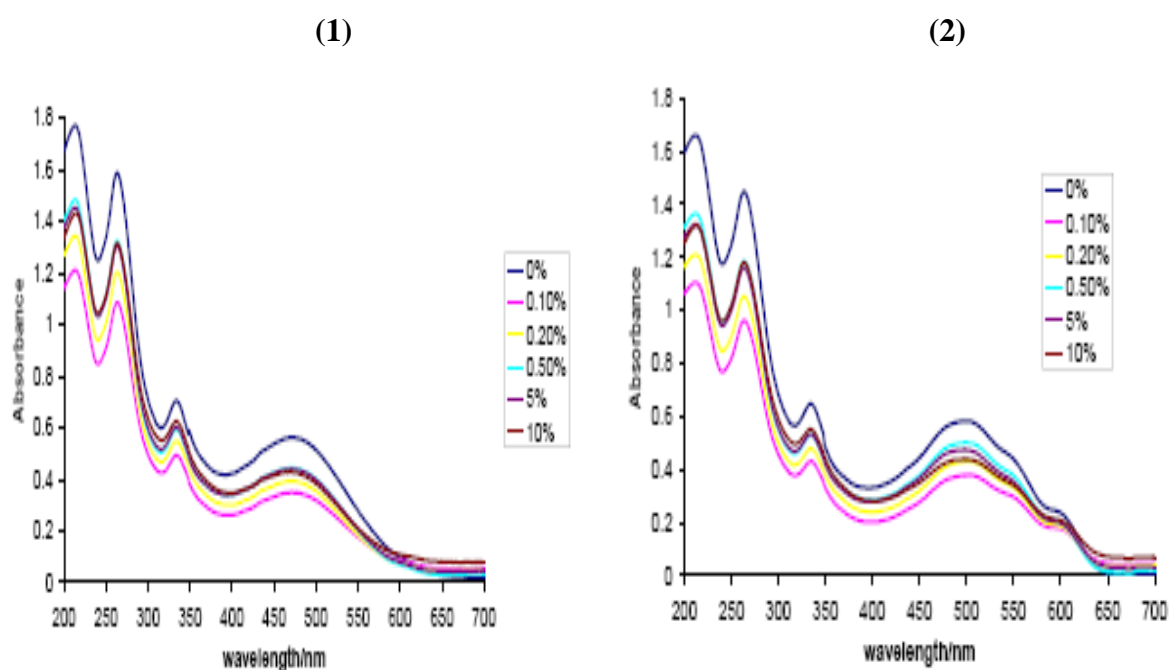
Before annealing there is a little difference in the shape of the absorption spectra whether MWNTs are added or not, but the magnitude of absorption is appreciably higher when MWNTs are added. This increase in absorption suggests some electronic interaction between the MWNTs and P3HT. In other words, the peaks at 400-600 nm are assigned to the  $\pi$ - $\pi^*$  transition in the polymer P3HT. The reason why this overall peak is very wide could be due to the different conjugation lengths in the polymer.

There is no change in the peak position and also no change in the absorption intensity. In the photoexcited state, however charge transfer from the photoexcited polymers to the nanotubes is expected to occur [73, 74]. But it is appreciable that after the films have been annealed there is an even more interesting change in the absorption spectrum of the MWNT:P3HT composite with an extra absorption band observed at approximately 230 nm, attributable to MWNTs. The effect of heat treatment on the optical absorption of MWNT:P3HT blend has not been reported before and thus the precise origin of this peak is unknown.



### 7.3.4 Absorption spectroscopy of P3HT:PCBM:MWNT composite films

Absorption spectra from P3HT:PCBM composites suggests that there are lower conjugation lengths compared to just P3HT. This might be because the PCBM has broken up the conjugation of the polymer, but it returns slightly on annealing. The absorption spectrum does not change upon addition of MWNT into the P3HT:PCBM composite, it seems to be that the MWNT do not affect the structure of the polymer because the nanotubes are bigger in size than the fullerenes which can get into the polymer chains to break the conjugation.



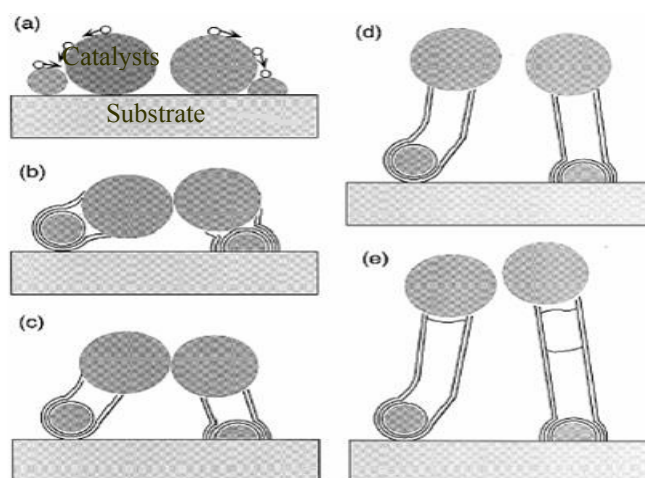
**Figure 7.8.** UV-vis absorption spectra of 1:1 P3HT:PCBM blend film with varying wt% MWNTs added before annealing (1) and after annealing (2) at 140°C/4 minutes.

Figure 7.8 above shows the absorption spectra of 1:1 P3HT:PCBM blend with varying MWNT content before annealing (1) and after annealing (2). There appears to be a little change in the shape of the absorption spectra of 1:1 P3HT:PCBM blends when MWNTs are added, either before or after annealing, even for concentrations of 10 wt%. This observation would indicate the absence of electronic interaction in the ground state between MWNTs and P3HT. This is in contrast to what was observed in Figure 7.7, here in this Figure 7.8 the absorption band at 220 nm belongs to the contribution of the fullerene PCBM. It is possible in the ternary blend that this signal is swamped by the strong absorption of PCBM at a similar wavelength.

Clearly though, MWNTs do not cause such changes to the P3HT absorption region as PCBM does. This suggests that the MWNTs cannot be in such intimate contact with polymer as PCBM, in order to break its inter-chain order. This could be expected, given the large size of the MWNTs with respect to PCBM, but this then raises the question and possibly future work of how an interface for charge separation as efficient as that between PCBM and P3HT can possibly exist between MWNTs and P3HT.

### 7.3.5 Chemical Vapour Deposition (CVD)

Since it is known that nanotubes enhance the transport properties of a polymer [75], we introduced a completely new and innovative method of producing polymer nanotube composites where the density of the nanotubes within the composite can be controlled. Large quantities of carbon nanotubes can be produced on a substrate simultaneously using CVD. The carbon nanotubes are grown at elevated temperatures between 500 °C and 1100 °C. The nanotubes are usually prepared by the decomposition of an organic catalyst containing ferromagnetic nanoparticles (e.g., Fe, Ni or Co). Different catalysts were used in this work, poly(styrene-vinylferrocene) copolymer blend (PS-PVF) used in Trinity College and Iron (II) phthalocyanine (FePc) used in the University of Wollongong, Australia. A gas flow of Ar/C<sub>2</sub>H<sub>2</sub> or Ar/H<sub>2</sub> (1:1 v/v, 20 cm<sup>3</sup>/min) was introduced into the quartz tube and with the iron-catalysts this caused the growth of carbon nanotubes on substrates, such as quartz glass, ITO glass and silicon substrates. Figure 7.8 shows the mechanism of the carbon nanotubes growth, from the decomposition of catalysts (a) to its subsequent nanotube growth (b - e).



**Figure 7.9.** Proposed growth mechanism of the carbon nanotubes on flat substrates using CVD technique. Reproduced from [76].

As discussed in Chapter 3, two different CVD set-ups were used during this work. The CVD system in Trinity College allows the growth of nanotube “forests” with no control on the distribution of the nanotubes, and the one used in Wollongong University has two furnaces and allows the growth of aligned carbon nanotubes.

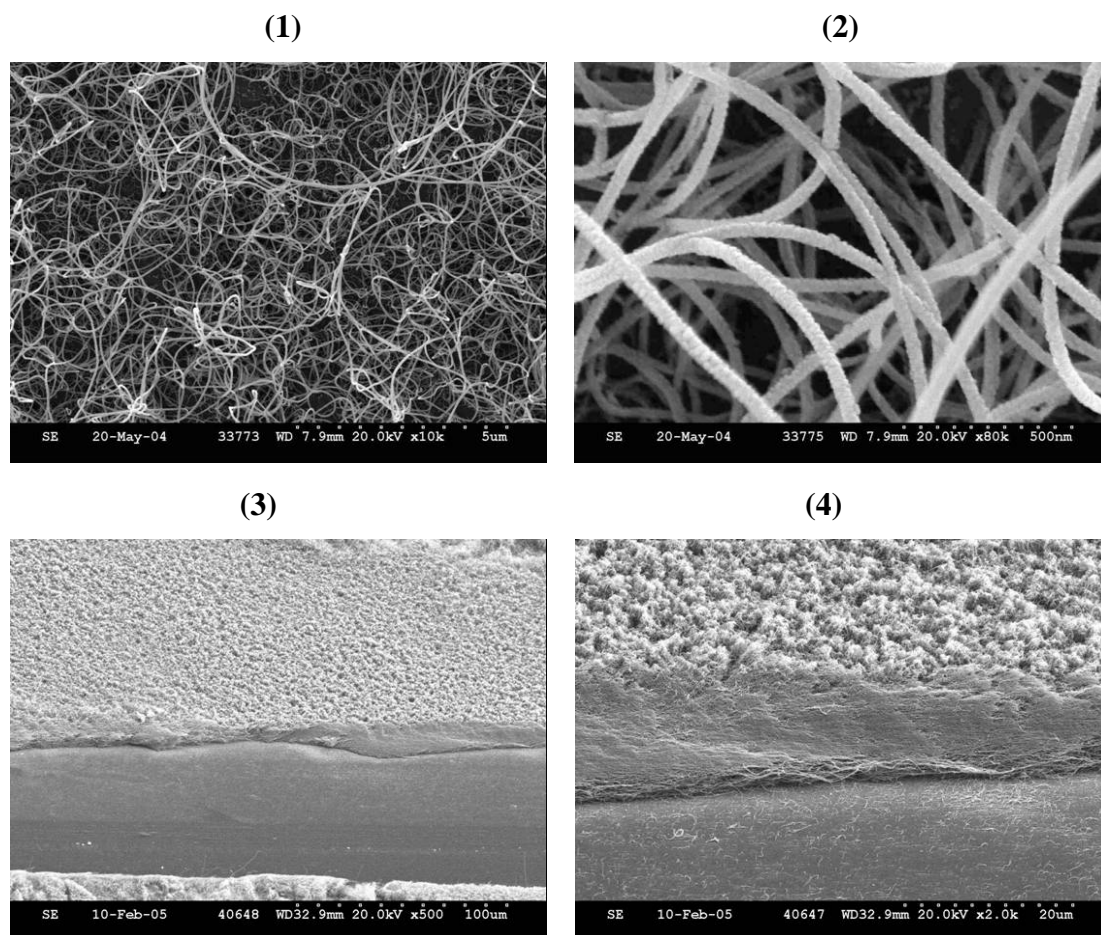


**Figure 7.10.** SEM images showing carbon nanotube growth on silicon substrates. Images (1) and (2) taken at lower and higher resolution respectively. Thicknesses shown in (3) and (4).

CVD allows the density and positioning of the nanotubes within the composite to be controlled. Parameters such as temperature and gas flow rates need to be optimized in order to get a good nanotube growth. This opens up the avenue toward simple electronic device fabrication. Figures 7.10 (1) and 7.10 (2) show the dispersion of the nanotubes grown on silicon substrates and Figures 7.10 (3) and 7.10 (4) show the average thicknesses of the nanotube “forests”, around 20  $\mu\text{m}$ , also grown on silicon substrates using CVD.

Photovoltaic devices incorporating these carbon nanotubes forests would be constructed based on a sandwich structure of metal electrodes at the sides and polymer-CVD carbon nanotubes blend in between.

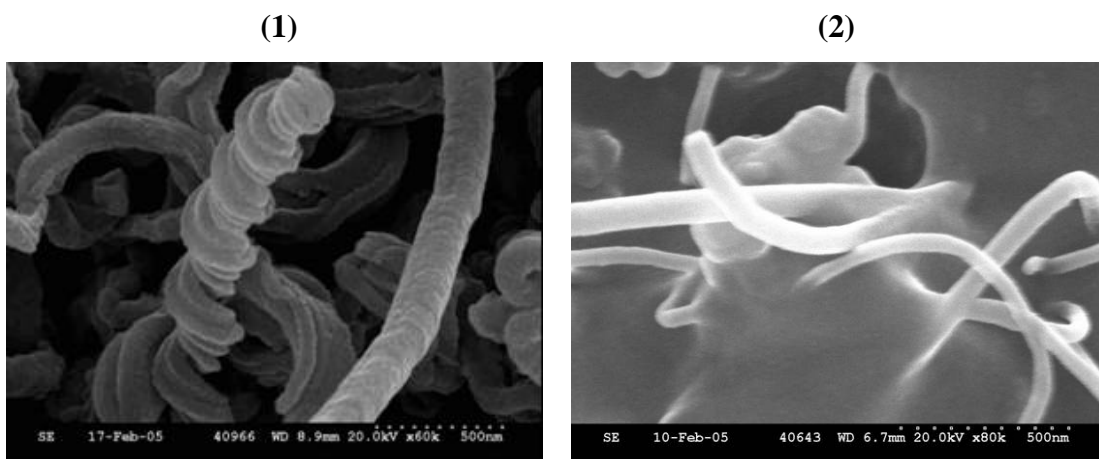


**Figure 7.11.** SEM images showing nanofibres grown on ITO substrate (ITO substrates were bent after heating at 700 °C.) (1), and a carbon nanotube array embedded into a flexible polymer matrix (Polydimethylsiloxane) (PDMS) giving a free-standing flexible film containing a controlled nanotube morphology (2).



**Figure 7.12.** Picture of the free-standing composite device. Figure 7.11 (2) shows the result of this elastomer containing carbon nanotubes.

Figure 7.11 (1) shows nanofibres grown on ITO substrate. Figure 7.11 (2) and Figure 7.12 show a free-standing flexible film where the nanotubes are embedded into the polymer. The idea of being able to control the positioning and length of the nanotubes arises at this stage.

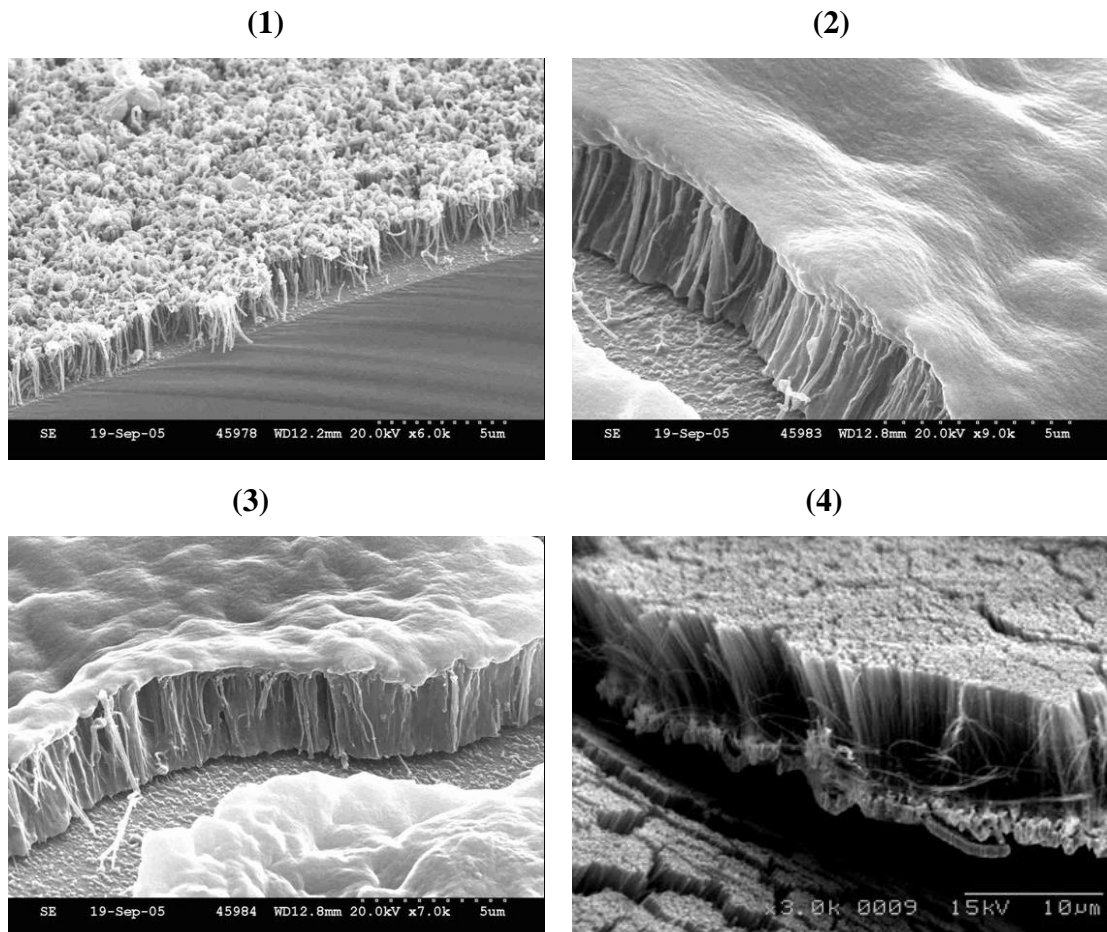
Aligned carbon nanotubes will encourage an enhanced contact between the polymer and nanotubes for better charge transfer. A better contact will be expected using aligned carbon nanotubes than using the nanotube “forest” growth showed in Figure 7.10 (3) and 7.10 (4).

The interaction of carbon nanotubes with conjugated polymer allows charge separation of the photogenerated excitons (electron-hole pair) in the polymer and efficient electron transport to the anode through the aligned nanotubes.

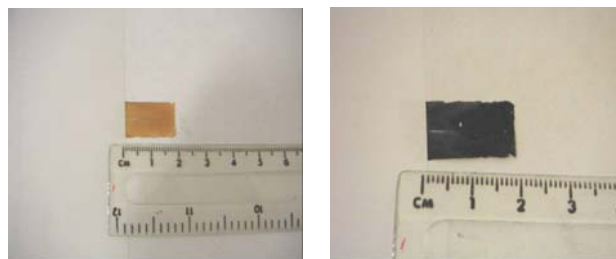
Properties of aligned carbon nanotubes such as high electron transport, higher current density capacity, and improvements in electrical conductivity and high mechanical strength will be taken into account in photovoltaic devices.

Figure 7.13 (1) shows aligned carbon nanotubes grown on quartz glass substrates. Short aligned nanotube lengths of around 1-2  $\mu\text{m}$  were achieved.

If the nanotubes are grown less densely packed, then this distribution will facilitate a better contact with the polymer, Figures 7.13 (2) and 7.13 (3) show the nanotubes blended into the polymer. The polymer was dropcasted onto the nanotubes.



**Figure 7.13.** SEM images showing the aligned carbon nanotube growth on quartz substrate (1), embedded in a polymer (2) and (3), and gold-covered on  $\sim 10 \mu\text{m}$  carbon nanotube film image (4) taken in the laboratory of the IPRI, Wollongong University, NSW, Australia.



**Figure 7.14.** Pictures of the device shown in Figure 7.13 (4). Top views of the gold-covered side and the carbon nanotube side of the device are shown.

To construct aligned carbon nanotube arrays on conducting electrodes [35], a layer of gold was sputter-coated onto the amorphous carbon layer covering the aligned nanotube film (see Figures 7.13 (4) and 7.14). The gold-covered carbon nanotube film was then separated from the quartz glass substrate used for the nanotube growth with an aqueous solution of 30% HF [33]. This could then be incorporated into a photovoltaic device as shown in Figure 7.14. The general structure of these free-standing devices is the following: one layer of aligned nanotubes embedded in the polymer and this composite between metal electrodes.

## 7.4 Conclusions

The discovery of carbon nanotubes has marked an important milestone in materials science and nanotechnology, due to the prospects for their use in future nanoscale applications. The decision to include carbon nanotubes in this thesis was based on the effects in providing photoinduced charge transfer and enhanced electron transport.

In the first part of this Chapter, organic photovoltaic devices have been prepared using single-wall carbon nanotubes (SWNT) as electron acceptors. The operating principle of this device is that the interaction of the carbon nanotubes with the polymer allows charge separation of the photogenerated excitons in the polymer and efficient electron transport to the electrode through the nanotubes. ITO/P3OT/Al and ITO/P3OT:SWNT/Al were the devices analysed.

In the second part, multi-wall carbon nanotubes (MWNT) were used in ITO/MEH-PPV/PPV:MWNT/Al devices. The presence of MWNTs widened the active layers and increased the power conversion by an order of magnitude, compared to the cell without MWNTs.

A good quality photovoltaic response using MWNT in polythiophenes was not achieved. ITO/PHT:MWNT/Al, ITO/P3HT/P3HT:MWNT/Al and ITO:P3HT:PCBM:MWNT/Al were the devices prepared and short-circuiting was found in most of the cases. Possible explanations are given in this Chapter in order to understand this behaviour. Absorption spectroscopy studies of P3HT:MWNT and P3HT:PCBM:MWNT were also discussed.

Finally, a scalable inexpensive technique has been introduced, Chemical Vapour Deposition (CVD), to fabricate carbon nanotube composites. It was demonstrated that

multi-walled carbon nanotubes are grown on different substrates and these periodic nanotube arrays are then incorporated into a polymer. Therefore, the combination of these simple methods for production of large-areas of nanotubes not only facilitates the characterisation of physical properties of nanotubes but also allows their effective incorporation into devices for practical applications. Controlling the position and density of nanotubes within the composite has an enormous importance for commercial nanotechnology devices and could play an important role to prevent short circuiting. However, making organic solar cells devices using CVD is still under analysis due to the difficulty of handling such free-standing and very thin devices.

# CHAPTER 8 - CONCLUSIONS & FUTURE WORK

## 8.1 Conclusions

The discovery of organic materials marked an important milestone in materials science and nanotechnology, due to the prospects for their use in future nano-scale applications. This thesis has presented a study on organic photovoltaic devices using conjugated polymers and fullerenes as electron donor and acceptor materials respectively.

The studies showed that the photovoltaic response of conjugated polymer and fullerene materials can be significantly enhanced through nanoscale control of the spatial location of the components.

In Chapter 5, initial studies of MEH-PPV devices consisted of measuring their short-circuit current and open circuit voltages as a function of the film thickness with illumination through the ITO electrodes. It was shown in terms of the filter effect that only a very thin polymer layer was photo-active in our single layer polymer solar cell, which resulted in the power efficiency being greater for thinner polymer solar cells. The maximum power conversion efficiencies achieved for MEH-PPV and MEH-PPV:PCBM photovoltaic devices were  $0.83 \times 10^{-3} \%$  and  $0.01 \%$  respectively. Spectral response studies on MEH-PPV devices were also discussed.

In Chapter 6, polymer and fullerene composites such as P3HT:PCBM were investigated. Using P3HT, which is known to have high-quality miscibility for PCBM, the interdiffusion between these two materials and further improved photovoltaic performance was observed. P3HT was characterised as a semicrystalline polymer, thus having a glass transition temperature, a melting point temperature and crystallisation point temperature. To study the influence on melting the polymer during interdiffusion-annealing, ITO / PEDOT:PSS / P3HT:PCBM / Al devices were annealed at temperature below  $T_m$  (but above  $T_g$ ). In this case, the photocurrents after annealing improved significantly compared to the unannealed devices. Differential Scanning Calorimetric analyses (DSC) of the polymer and fullerene composites were also carried out, showing the increased crystallinity of the P3HT after annealing. It has been demonstrated the great influence of the crystallinity on the efficiency of photovoltaic devices.

Also in Chapter 6, analysing P3HT:PCBM devices, it was shown that the I-V characteristics were improved by annealing treatment. The short circuit current  $J_{sc}$



improves from 4.98 mA/cm<sup>2</sup> in the unannealed devices to 7.00 mA/cm<sup>2</sup> in devices annealed at 140 °C for 4 minutes. For the best devices (annealed at 140 °C), the power conversion efficiency was calculated to be 2.28% using 80 mW/cm<sup>2</sup> white light illumination. This demonstrated that the annealing approach has significant potential for fabrication of highly efficient organic solar cells. For P3HT:PCBM films, morphology studies were carried out using scanning electron microscopy (SEM) and transmission electron microscopy (TEM) showing the differences in the nanoscale morphology of annealed and unannealed devices.

In Chapter 7, the use of single-walled nanotubes (SWNT) and multi-walled nanotubes (MWNT) for efficient charge transport in photovoltaic devices has been demonstrated. By using small concentrations of single-walled nanotubes with polymers such as P3OT, previous studies have shown that the short circuit current was improved by more than two orders of magnitude over the device without nanotubes present. While the use of multi-walled nanotubes in polymers such as PPV, reported previously, also showed improved charge transport. Here in this work the use of this MWNT into polymers blends, such as P3HT, did not improve the charge transport through the composites to the electrodes.

Also in Chapter 7, the technique of chemical vapour deposition, CVD, was then introduced to demonstrate an improvement in nanotube processing, control of nanotube length, the ability to control the orientation and positioning of nanotubes, and also, the potential to be incorporated into a polymer composite for photovoltaic devices.

## **8.2 Future work**

While these results have shown that organic materials such as PCBM can be used as charge transport media to enhance the efficiency of existing organic devices, there are still improvements to be made.

As regards increasing the power efficiency of polymer solar cells using carbon nanotubes, work is ongoing to use SWNT and, especially, MWNT in conjugated polymer composites. Further investigation of composites of MWNT, grown by organic CVD, with conjugated polymers and their photophysical properties is an interesting subject to continue exploring in the near future.

However, a limiting problem for potential industrial applications of organic materials still remains: chemical and electronic stability. Operational lifetime of tens

of thousands of hours is requested for all practical applications. Organic materials have to be protected from air humidity to achieve such lifetimes. The stability problem has to be controlled in the future in order for them to enter into large scale applications.

## REFERENCES

- [1] C. J. Campbell and J. H. Laherre, *Scientific American*, **278**, 78-83 (1998).
- [2] S. E. Shaheen, C. J. Brabec, N. S. Sariciftci, F. Padinger, T. Fromherz, J. C. Hummelen, *Appl. Phys. Lett.* **78**, 841-843 (2001).
- [3] M. Granstrom, K. Petritsch, A.C. Arias, A. Lux, M.R. Andersson, R.H. Friend, *Nature* **395**, 257 (1998).
- [4] G. Yu, J. Gao, J. C. Hummelen, F. Wudl, A. J. Heeger, *Science* **270**, 1789-1791 (1995).
- [5] P. Peumans, S. R. Forrest, *Appl. Phys. Lett.* **80**(2), 338-338 (2002).
- [6] W. U. Huynh, J. J. Dittmer, A. P. Alivisatos, *Science* **295**, 2425-2427 (2002).
- [7] H. Ago, M. S. P. Shaffer, D. S. Ginger, A. H. Windle, R. H. Friend, *Phys. Rev. B* **61**(3), 2286-2290 (2000).
- [8] C. K. Chiang, C. R. Fincher, Y. W. Park, A. J. Heeger, H. Shirakawa, E. J. Louis, S. C. Gau, A. G. McDiarmid, *Phys.Rev.Lett.* **39**, 1098 (1977).
- [9] L. Chen, D. Godovsky, O. Inganäs, J. C. Hummelen, R. A. J. Janssens, M. Svensson, M. R. Andersson, *Advanced Materials* **12**(18),1367- (2000).
- [10] G. Dennler, N. S. Sariciftci, *1435 Proceedings of the IEEE*, Vol. **93**, No. 8, 1429-1439, August (2005).
- [11] S. B. Lee, T. Katayama, H. Kaijii, H. Araki and K. Yoshino, *Synthetic Metals* **121**, 1591-1592 (2001).
- [12] E. J. W. List, C. Creely, G. Leising, N. Schulte, A. D. Schluter, U. Scherf, K. Mullen, W. Graupner, *Chemical Physics Letters* **325** (1-3), 132-138 (2000).
- [13] I. D. W. Samuela, B. Crystallb, G. Rumblesb, P. L. Burn, A. B. Holmes and R. H. Friend, *Chem. Phys. Lett.* **213**(5-6), 472-478 (1993).
- [14] N. T. Harrison, G. R. Hayes, R. T. Phillips, R. H. Friend, *Phys. Rev. Lett.* **77**, 1881-1884 (1996).
- [15] J. J. M. Halls, K. Pichler, R. H. Friend, S. C. Moratti, A. B. Holmes, *Appl. Phys. Lett.* **68** (22), 3120-3122 (1996).
- [16] A. Haugeneder, M. Neges, C. Kallinger, W. Spirkl, U. Lemmer, , J. Feldmann, U.Scherf, E. Harth, A. Gügel, K. Müllen, *Phys. Rev. B* **59**, 15346-15351 (1999).
- [17] Chistoph J. Brabec, N. Serdar Sariciftci, Jan C. Hummelen, *Adv. Funct. Mater.* **11**, No.1, February (2001).
- [18] Indium Tin Oxide (ITO), Cambridge, England, (<http://www.uqgoptics.com/>).

- [19] Donor and acceptor materials: American Dyes Source, Quebec, Canada, (<http://www.adsdyes.com/>), Bayer, Leverkusen, Germany (<http://www.bayer-echemicals.com/>) and Nanocyl S.A., Sambreville, Belgium (<http://www.nanocyl.com/>).
- [20] H. W. Kroto, J. R. Heath, S. C. O'Brien, R. F. Curl, R. E. Smalley, *Nature* **318**, 162 (1985).
- [21] W. Kratschmer, L. D. Lamb, K. Fostiropoulos, D. R. Huffman, *Nature* **347**, 354 (1990).
- [22] S. Iijima, *Nature* **354**, 56 (1991).
- [23] P. M. Ajayan, T. W. Ebbesen, *Rep. Prog. Phys.* **60**, 1025 (1997).
- [24] J. W. G. Wildoer, L. C. Venema, A. G. Rinzler, R. E. Smalley, C. Dekker, *Nature* **391**, 59 (1998).
- [25] J. W. Mintmire, D. H. Robertson, C. T. White, *J. Phys. Chem. Solids.* **54**, 1835 (1993).
- [26] D. H. Robertson, D. W. Brenner, J. W. Mintmire, *Phys. Rev. B* **45**, 12592 (1992).
- [27] X. Gong, J. Liu, S. Baskaran, R. D. Voise, J.S. Young, *Chem. Mater.* **12**, 1049 (2000).
- [28] G. Overney, W. Zhong, D. Tomanek, *Zeitschrift fur physik d-atoms molecules and clusters* **27**, 93 (1993).
- [29] D. Srivastava, M. Menon, K. Cho, *Phys. Rev. Lett.* **83**, 2973 (1999).
- [30] O. Lourie, D.M. Cox, H.D. Wagner, *Phys. Rev. Lett.* **81**, 1638 (1998).
- [31] O. Lourie, H.D. Wagner, *J. Mater. Res.* **13**, 2418 (1998).
- [32] E. Lahiff, C. Y. Ryu, S. Curran, A. I. Minnet, W. J. Blau, P. M Ajayan, *Nano Letters*, Vol. **3**, No. 10 , 1333-1337 (2003).
- [33] S. Huang, L. Dai, A. W. H. Mau, *J. Phys. Chem. B* **103**, 4223-4227 (1999).
- [34] Y. Yang, S. Huang, H. He, Albert W. H. Mau, L. Dai, *J. Am. Chem. Soc* **121**, 10832-10833 (1999).
- [35] B. Wang, X. Liu, H. Liu, D. Wu, H. Wang, J. Jiang, X. Wang, P. Hu, Y. Liu, D. Zhu, *J. Mater. Chem.* **13**, 1124-1126 (2003).
- [36] UQC Optics, Limited, Cambridge, England, (<http://www.uqgoptics.com/>).
- [37] M. Cecchi, H. Smith, and D. Braun, *Synth. Met.* **121**, 1715-1716, (2001).
- [38] R. K. Yonkoski, D. S. Soane, *J. Appl. Phys.* **72**, 725 (1992).
- [39] C. W. Tang, *Appl. Phys. Lett.* **48**, 183 (1986).

- [40] L. Chen, D. Godovsky, O. Inganäs, J. C. Hummelen, R. A. J. Janssens, M. Svensson, and R. Andersson, *Adv. Mater.* **12**, 1367 (2000).
- [41] R. N Marks, J. J. M. Halls, D. D. C. Bradley, R. H. Friend, and A. B. Holmes, *J. Phys.: Condens. Matter.* **6**, 1379 (1994).
- [42] W. Riess, S. Karg, V. Dyakonov, M. Meier, and M. Schwoerer, *J. Luminescence* **60-61**, 906 (1994).
- [43] K. Petritsch and R. H. Friend, *Synth. Met.* **102**, 976 (1999).
- [44] T. Erb, U. Zhokhavets, G. Gobsch, S. Raleva, B. Stühn, P. Schilinsky, C. Waldauf, C. J. Brabec, *Adv. Funct. Mater.* **15**, 1193-1196 (2005).
- [45] L. S. Roman, M. R. Andersson, T. Yohannes, O. Inganäs, *Adv. Mater.* **9**, 1110 (1997).
- [46] T. J. Savenije, J.E. Kroece, X. N. Yang, J. Loos, *Thin Solid Films* **511**, 2-6 (2006)
- [47] Y. Kim, S. A. Choulis, J. Nelson, S. Cook, J. R. Durrant, D. D. C. Bradley, *Journal of Material Science* **40**, 1371-1376 (2005).
- [48] D. Chirvase, J. Parisi, J. C. Hummelen and V. Dyakonov, *Nanotechnology* **145**, 1317-1323 (2004).
- [49] F. Padinger, Roman S. Rittberger, Niyazi S. Sariciftci, *Adv. Funct. Mater.* **13**, no.1, 85-88, January (2003).
- [50] M. J. Winokur, D. Spiegel, Y. Kim, S. Hotta and A. Heeger, *J. Synth. Met.* **28**, C419 (1989).
- [51] S. A. Chen and J. M. Ni, *Macromolecules* **25**, 6081 (1992).
- [52] K. Tashiro, Y. Minagawa, M. Kobayashi, S. Morita, T. Kawai and K. Yoshino, *Synth. Met.* **55-57**, 321 (1993).
- [53] K. Iwasaki, H. Fujimoto and S. Matsuzaki, *Synth. Met.* **63**, 101 (1994).
- [54] C. Roux, J. Y. Bergeron and M. Leclerc, *Makromol. Chem.* **194**, 869 (1993).
- [55] C. Roux and M. Leclerc, *Chem. Mater.* **6**, 620 (1994).
- [56] A. Bolognesi, W. Porzio, F. Provasoli and T. Ezquerra, *Makromol. Chem.* **94**, 817 (1993).
- [57] S. Malik, Arun K. Nandi, *Journal of Polymer Science: Part B: Polymer Physics*, Vol. **40**, 2073-2085 (2002).
- [58] S. Hugger, R. Thomann, T. Heinzl, T. Thurn-Albrecht, *Colloid Polym. Sci.* **282**, 932-938 (2004).
- [59] Y. Zhao, G. Yuan, P. Roche, M. Leclerc, *Polymer* **36**, 2211 (1995).

- [60] Y. Kim, S. A. Coulis, J. Nelson, D. D. C. Bradley, *Applied Physics Letters* **86**, 063502 (2005).
- [61] T-A. Chen, X. Rieke D. Wu, *J. Am. Chem. Soc.* **117**, 233 (1995).
- [62] Perkin Elmer, *Perkin Elmer Thermal Analysis Newsletter* PETAN-58.
- [63] G. Gobsch, U. Zhokhavets, T. Erb, M. Al-Ibrahim, H. Hoppe, N. S. Sariciftci, p. Schilinsky, C. Waldauf, C. Brabec, in *Proc. Of the 1<sup>st</sup> Int. Symp. On Technologies for Polymer Electronics*, TITK Rudolstadt and Technical University Ilmenau, Rudolstadt/Ilmenau, Germany 2004.
- [64] Tom J. Savenije, Jessica E. Kroeze, X. Yang, J. Loos, *Adv. Funct. Mater.* **15**, 1260-1266 (2005).
- [65] X. Yang, J. K. J. Van Durren, R. A. J. Janssen, M. A. J. Michels, J. Loos, *Macromolecules* **37**, 2151 (2004).
- [66] X. Yang, J. K. J. Van Duren, M. T. Rispens, J. C. Hummelen, R. A. J. Janssen, M. A. J. Michels, J. Loos, *Adv. Mater.* **16**, 802 (2004).
- [67] H. Ago, K. Petritsch, M. S. P. Shaffer, A. H. Windle, R. H. Friend, *Adv. Mat.* **11**, 1281, (1999).
- [68] S. Curran, A. P. Davey, J. N. Coleman, A. B. Dalton, B. McCarthy, S. Maier, A. Drury, D. Gray, M. Brennan, K. Ryder, M. L. de la Chapelle, C. Journet, P. Bernier, H. J. Byrne, D. Carroll, P. M. Ajayan, S. Lefrant, W. Blau, *Synthetic Metals* **103**, 1-3, 2559-2263 (1999).
- [69] J. N. Coleman, A. B. Dalton, S. Curran, A. Rubio, A. P. Davey, A. Drury, B. McCarthy, B. Lahr, S. Roth, R. C. Barklie, W. J. Blau, *Advanced Materials* **12**, 3 213-217 (2000).
- [70] R. Murphy, J. N. Coleman, M. Cadek, B. McCarthy, M. Bent, A. Drury, R. C. Barklie and W. J. Blau, *J. Phys. Chem. B.* **106**, 9 3087-3091 (2002).
- [71] E. Kymakis, G.A.J. Amaratunga, *Appl. Phys. Lett.* **80**, 112 (2002).
- [72] P. Fournet, J. N. Coleman, D. F. O'Brien, B. Lahr, A. Drury, C. R. McNeill, P. C. Dastoor, G. G. Wallace, H.-H. Hörhold, and W. J. Blau, *Proceedings of SPIE* Vol. **4876**, 338-350 (2003).
- [73] H. Ago, M. Shaffer, D. S Ginger, A. H. Windle and R. H. Friend, *Phys. Rev. B* **61**, 2286 (2000).
- [74] I. Musa, M. Baxendale, G. A. J. Amaratunga and W. Eccleston, *Synthetic Methals* **102**, 1250 (1999).
- [75] P. Fournet, J. N. Coleman, D. F. O'Brien, B. Lahr, A. Drury, H.-H. Hörhold, W. J. Blau, *J. Appl. Phys.* **90(2)**, 969-975 (2001).
- [76] D. Li, L. Dai, S. Huang, A. W. H. Mau, and Z. L. Wang, *Chem. Phys. Lett.* **316**, 349-355 (2000).